Mechanistic Insight into Electrochemical CO_2 Reduction on Boron-doped Diamond Cathode

March 2023

DU, Jinglun

A Thesis for the Degree of Ph.D. in Science

Mechanistic Insight into Electrochemical CO_2 Reduction on Boron-doped Diamond Cathode

March 2023

Graduate School of Science and Technology
Keio University

DU, Jinglun

Table of Content

Chapter 1

General Introduction

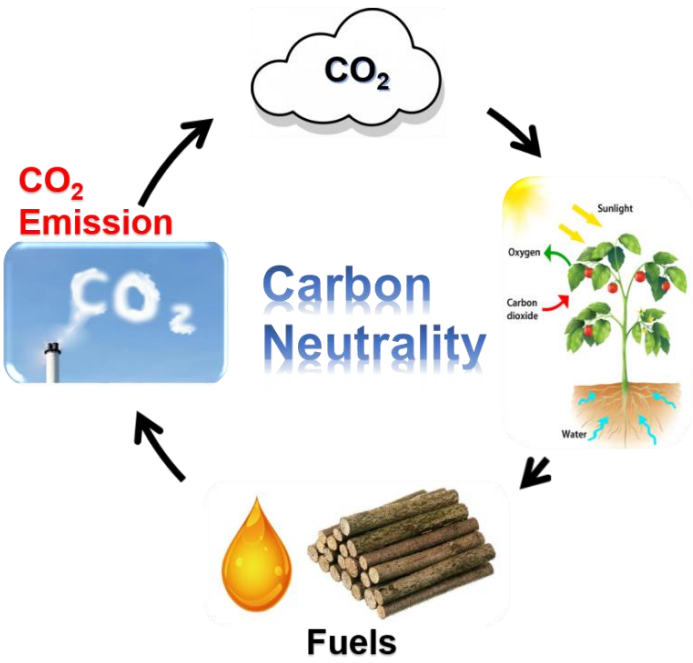

1.1 Carbon neutrality and artificial carbon offset

1.1.1 The purpose of carbon neutrality

In the recent years, extreme weather events caused by climate change lead to an increasingly serious impact on human life.[1,2] Excessive emissions of greenhouse gases including water vapor (H_2O), carbon dioxide (CO_2), methane (CH_4), nitrous oxide (N_2O), and ozone (O_3) are considered to be the primary cause of the current climate change (Figure 1.1). Among these, the emission of CO_2 from the combustion of fossil fuels is the main component of greenhouse gas emissions. In the 2015 Paris Agreement, nations collectively agreed to limit the global warming within 2 ℃. But actually, even with the constraints of the Paris Agreement, global warming will reach about 2.7 ℃ by the end of this century.[3] To limit global warming to 1.5 ℃, carbon dioxide emissions need to be halved by 2030 and zero emissions should be achieved by 2050.[4,5] This means that in the near future the emission of CO_2 from our daily life and the industry should be limited within the capacity of carbon offsets, that is, to achieve carbon neutrality.

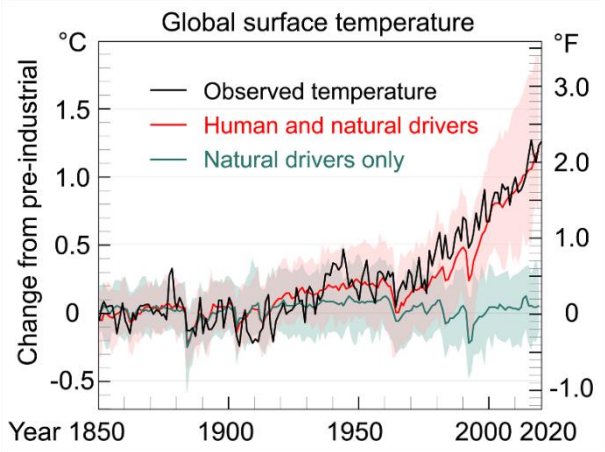

Figure 1.1 Average temperature changes of the global surface since the industrial revolution showing the temperature variation resulting from human activity and natural forces. Reprinted from ref. [1]. Copyright (2021) with permission from the IPCC website (www.ipcc.ch).

In addition to improving the living environment, carbon neutrality also possesses high economic value. According to researches on the social cost of carbon, continuous climate change will lead to the economic loss of about $ 1.5 trillion in global agricultural production, human health, property security and energy systems between

2015 and 2050.[6,7] Therefore, from the perspective of protecting the natural environment and saving economic losses, the strategy of carbon neutrality is a crucial topic that human society should strive to develop in the future.

1.1.2 Solutions for artificial carbon offset

The current researches on artificial carbon offset are mainly divided into the following four categories including 1) photochemistry, 2) biochemistry, 3) thermochemistry, 4) photo-electrochemistry and electrochemistry (Figure 1.2).[8] Besides, routes of mineralization, carboxylation and organic catalysis are also possible to be applied into the conversion of CO_2, but the products of these methods can hardly be utilized as fuels in a simple and direct way, which hinders their promotion for large-scale applications.[9–11]

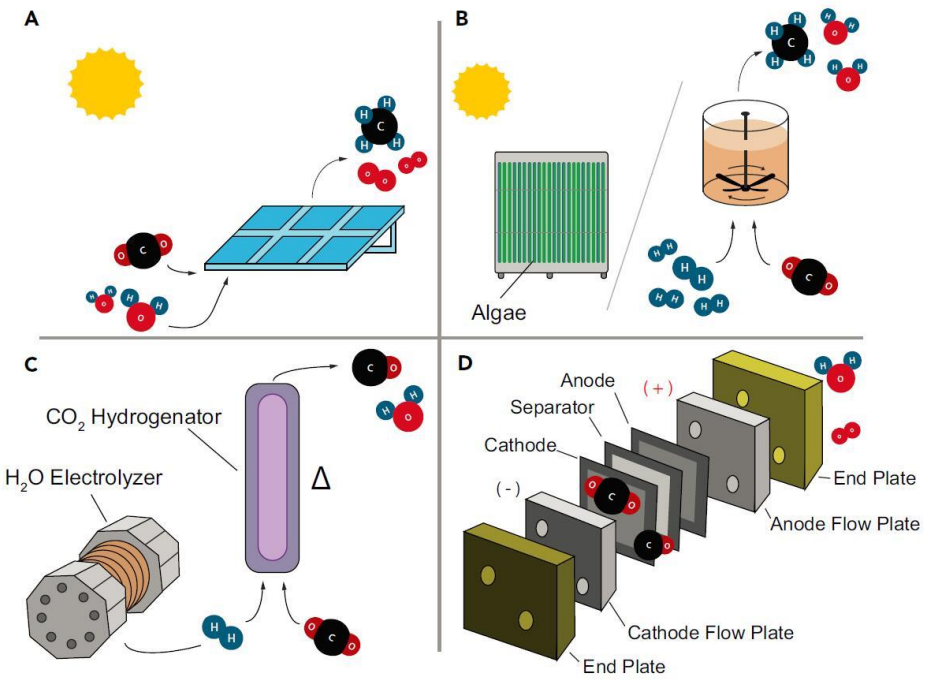

Figure 1.2 Schematic diagrams depicting the strategies for CO_2 conversion including (A) photochemistry, (B) biochemistry, (C) thermochemistry, and (D) electrochemistry. Adopted with permission from ref. [8]. Copyright (2018) from Elsevier.

(1) Photochemistry

Photocatalytic CO_2 reduction relies on the photoelectric effect of semiconductors. When a semiconductor is illuminated by light with energy above its band gap, electrons

in the valence band of the semiconductor material will be excited to leap to the conduction band. If the conduction band minimum of the semiconductor catalyst can meet the requirements of the CO_2 reduction reaction, the electrons in the conduction band are possible to release from the semiconductor surface and participate in the corresponding CO_2 reduction reaction. From this point of view, semiconductor materials such as TiO_2, SiC, Cu_2O, ZnO, TaON, CdS, etc are anticipated candidates for CO_2 reduction due to their suitable conduction band minimum.[12,13]

The superiority of photocatalytic CO_2 reduction is that the sunlight, which is the most common renewable and clean energy, can be directly adopted as the energy source for the conversion of CO_2, and no other harsh experimental conditions are further required, which means that the photocatalytic carbon offset could be performed anywhere. The corresponding weakness is shown as that the selection of photocatalytic semiconductors is not only limited by the energy level of its conduction band, but also by the catalytic activity of the material surface for the CO_2 reduction reaction.[14] Most of the photocatalytic materials that can complete the CO_2 reduction reaction well are wide-bandgap semiconductors, which exhibit poor utilization of sunlight, and the greater part of them can only absorb a part of ultraviolet light. Therefore, at present the production rate and energy conversion efficiency for photocatalytic CO_2 reduction are still at a relatively immature stage for industrial application.

(2) Biochemistry

The biocatalysis-based CO_2 reduction approach is also expected by researchers because of its safety and cleanliness. Microalgae and enzymes are able to effectively convert CO_2 into biofuels under the stimulation of light or electrical power.[15,16] The Biomass productivity with lipid as the main product can reach 2~7 g/L/day. However, high energy conversion efficiency and economic harvesting technology are still important issues to be further developed for biocatalytic CO_2 reduction in order to meet the requirements of industrial application. In addition, to maintain the reaction activity of microalgae and enzymes, during CO_2-conversion process the temperature and solution environment should be strictly limited.[17] These complicated operating procedures and the declined performance of biocatalytic CO_2 reduction are also obstacles to its commercial application.[18]

(3) Thermochemistry

In thermochemical CO_2 reduction, with the catalysis of some metals or metallic oxides, CO_2 can be converted into fuels such as syngas, methanol and hydrocarbons through catalytic thermal reforming of methane (CH_4) and hydrogenation.[19,20] The corresponding reaction mechanisms were shown in Table 1.1.

The CO_2 reforming of CH_4 included dry reforming (equation 1.1), oxy-CO_2 reforming (equation 1.2) and bi-reforming (equation 1.3).[21] As a simple method, dry reforming could produce the syngas with a H_2:CO ratio of 1:1 at the temperature of 800-1000 ℃. Compared with the dry reforming, oxy-CO_2 reforming possesses improved energy conversion efficiency, and the property of autothermal reforming is also a clear advantage of this approach. The bi-reforming route is a reaction in which both CO_2 and steam are adopted into the reforming of CH_4. In the bi-reforming reaction, the H_2:CO ratio can be adjusted by changing the reactant ratio (H_2O/CO_2) to meet the requirement of specific industrial designs. The hydrogenation reaction of CO_2 can directly synthesize hydrocarbons with CO_2 and H_2 as feedstock in a similar reaction pathway to Fischer–Tropsch synthesis, and also can synthesize methanol through the reaction route of equation 1.4.[20]

Overall, the thermochemical CO_2 reduction is able to achieve massive CO_2 conversion. Because of this, it is considered as an ideal method for large-scale industrial application. However, energy-intensive reaction routes and the expensive feedstock (H_2 or CH_4) lead to high costs and limit its economic value. The poor product selectivity and the deactivation of the catalyst are also problems that need to be solved in future researches.

Table 1.1 Equations showing the reaction routes for thermochemical CO_2 reduction.[21]

NO.	Equation	$\Delta H_{298\ K}$ (kJ/mol)	$\Delta G_{298\ K}$ (kJ/mol)
1.1	$CH_4 + CO_2 \rightleftharpoons 2CO + 2H_2$	+247	+170
1.2	$3CH_4 + CO_2 + O_2 \rightleftharpoons 4CO + 6H_2$	+58	-1
1.3	$3CH_4 + CO_2 + 2H_2O \rightleftharpoons 4CO + 8H_2$	+220	+151
1.4	$CO_2 + 3H_2 \rightleftharpoons CH_3OH + H_2O$	-50	+3.5

(4) Electrochemistry and photo-electrochemistry

Various value-added products can be synthesized via electrochemical CO_2 reduction reaction (eCO_2RR). Single-carbon products like formic acid, carbon monoxide and methane, two-carbon products for instance, ethanol and ethylene, and even three-carbon products such as propanol, have been directly obtained from the electro-reduction of CO_2 in aqueous solution (Table 1.2).[22,23] The main product of transition metal electrodes such as Au, Ag and Zn in eCO_2RR is CO, whereas Pb and Sn show remarkable selectivity for the production of formic acid. The composition of the products in eCO_2RR on Cu is complex, but the Cu electrode is one of the few electrodes that can produce multi-carbon products such as ethanol and ethylene with a selectivity of more than 5%.[24] Additionally, metal-free carbon electrodes can also complete the eCO_2RR well.[25] From the perspective of technological application, production rate, energy conversion efficiency, product selectivity, long-term stability and economic value are considered to be the key elements affecting the selection of working electrode and the corresponding product.[26]

As a safe and clean CO_2 conversion process, eCO_2RR possesses excellent energy conversion efficiency and is facile to be implemented.[27] Inspired by photo-catalysis, when suitable semiconductor electrode was set as working electrodes, both electric and solar energies could be efficiently adopted for CO_2 conversion, namely, photo-electrochemical CO_2 reduction.[28] Furthermore, if photovoltaic modules are applied as the electrical power for eCO_2RR, sustainable and efficient carbon offsets system will be achieved in which only renewable energy is cost without any additional energy investment. By combining solar cells with electrochemistry, Grätzel group and Zheng group attained the solar-to-chemical energy conversion efficiencies of 13.4% and 15.6%, respectively.[29,30] With the assistance of gas diffusion electrodes, Atwater group further boosted the solar-to-chemical energy conversion efficiency to 19.1%.[31] The controllable potential in electrochemistry also provide more options for the investigation of eCO_2RR.

Until now, it is still difficult for eCO_2RR to achieve impressive energy efficiency and dramatic current density at the same time. The fundamental factor that affects the performance of eCO_2RR is the overpotential for the formation of key reaction intermediates.[32] However, the current understanding of the eCO_2RR process is still not clear enough. For purpose of achieving acceptable production rate and energy conversion efficiency for commercial applications, more efforts should be devoted to

the investigation on the pathways and mechanisms of eCO_2RR. Beyond that, the high-efficiency synthesis of more economically valuable multi-carbon products and the long-term stable electrolytic reduction are also promising directions for future researches.

Table 1.2 Electrochemical equations showing the representative reaction mechanisms for eCO_2RR.[22,23]

NO.	Equation	Product	$E^0_{H_2} - E^0$ (V)
1.5	$CO_2 + 2H_2O + 2e^- \leftrightarrow HCOOH + 2OH^-$	Formic acid	-0.1707
1.6	$CO_2 + H_2O + 2e^- \leftrightarrow CO + 2OH^-$	CO	-0.104
1.7	$CO_2 + 6H_2O + 8e^- \leftrightarrow CH_4 + 8OH^-$	Methane	0.1691
1.8	$2CO_2 + 9H_2O + 12e^- \leftrightarrow C_2H_5OH + 12OH^-$	Ethanol	0.084
1.9	$2CO_2 + 8H_2O + 12e^- \leftrightarrow C_2H_4 + 12OH^-$	Ethylene	0.079
1.10	$3CO_2 + 13H_2O + 18e^- \leftrightarrow C_3H_8O + 18OH^-$	Propanol	0.098

1.2 Electrochemical CO_2 reduction

1.2.1 Reaction pathways

The high overpotential and low product selectivity of eCO_2RR are attributed to the inappropriate adsorption energies for key reaction intermediates.[33] According to the Sabatier principle,[34] excessive binding strength of reaction intermediates will hinder the release of reaction products from the electrode surface, which will cause the further reduction of the attached products, consequently leading to low product selectivity and even catalyst poisoning. While, a too weak binding strength to the reaction intermediate will prevent the eCO_2RR from taking place.

The most widely recognized intermediate in eCO_2RR is the carbon dioxide radical anion ($CO_2^{\bullet-}$).[35,36] The corresponding reaction mechanisms were shown in Figure 1.3. If the $CO_2^{\bullet-}$ is hard to be adsorbed on the electrode surface, with the assistance of the negative potential from the electrode, CO_2 will be converted into formic acid in aqueous solution. If the electrode possesses enough adsorption capacity for $CO_2^{\bullet-}$, $CO_2^{\bullet-}$ will be first converted into -COOH on the electrode surface, and then further reduced to CO. CO is generally regarded as an important intermediate for the formation of C_{2+} hydrocarbons and carbon-containing oxygenates.[33,37] Therefore, if the produced CO cannot be smoothly removed from the electrode surface, C-C coupling will be further generated, resulting in the formation of multi-carbon products.

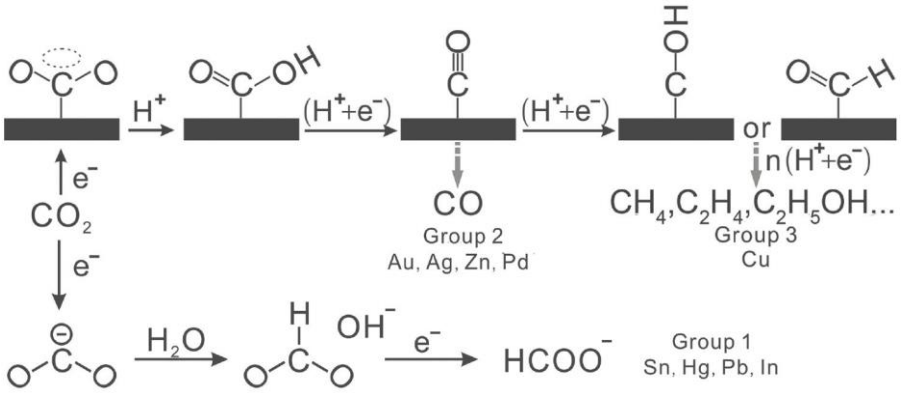

Figure 1.3 Proposed reaction mechanism for eCO_2RR on various metal electrodes in aqueous solution. Reproduced from ref. [35]. Copyright (2016) with permission from WILEY-VCH.

However, on the basis of the current researches, the $CO_2/CO_2^{\bullet-}$ redox couple lies at approximately -1.85 V vs SHE in aqueous media.[28] This potential presents a large amount of overpotential compared to the standard thermodynamic potential of cathodic eCO_2RR.[23,35] In practical experiments, efficient eCO_2RR also can be achieved at more positive potentials.[38,39] Thus, reaction intermediates other than $CO_2^{\bullet-}$ is speculated to exist in eCO_2RR.

Another mechanistic route of eCO_2RR by which to bypass the high energy $CO_2^{\bullet-}$ radical is through a series of proton-coupled electron transfers (PCET).[40] In the mechanistic explanation of PCET for eCO_2RR, *OCHO was regarded as a possible reaction intermediate for the formation of formic acid, while *COOH was considered as the main intermediate for the formation of CO.[37] This is mainly because in the theoretical calculation, from the perspective of Sabatier principle, electrodes with high catalytic activities for CO production such as Au and Ag exhibit more appropriate adsorption energy for *COOH, while the adsorption energy of *OCHO on formic acid producing electrodes such as Sn is in a reasonable position.[41] However, some researchers believe that *COOH also can be a reaction intermediate for the formation of formic acid.[42,43] Studt et al. proposed that based on the investigation through density functional theory calculations, since there is little correlation between the free energies of *COOH and *H, it is plausible for *COOH to act as a reaction intermediate in the electrochemical CO_2 reduction to formic acid.[44]

At present, the discussion on intermediates of eCO_2RR other than $CO_2^{\bullet-}$ mostly stays within the scope of theoretical calculations. Bocarsly group reported that by means of in situ ATR-IR spectroscopy, bicarbonate was observed to be a possible intermediate in a eCO_2RR pathway involving a two-electron transfer process.[45] Unfortunately, the

signals of reaction intermediates in the experimental part of that work cannot well support the proposed reaction mechanism. Moreover, the simultaneous transfer of two electrons is very rare in the mechanistic explanation of electrochemistry. Therefore, researches on the intermediates and reaction pathways for eCO_2RR still need to be further completed and supplemented by experimental investigations.

1.2.2 Catalytic sites

The source of catalytic active sites for eCO_2RR is often attributed to the undercoordinated site or the oxidized electrode surface (Figure 1.4).[25,35]

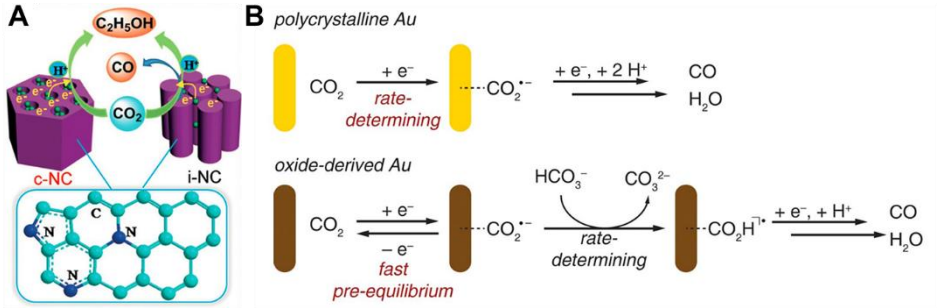

Figure 1.4 (A) Schematic diagram of the eCO_2RR on nitrogen-doped mesoporous carbon. Reproduced with permission from ref. [52]. Copyright 2017, WILEY-VCH. (B) Speculated mechanism for eCO_2RR on polycrystalline Au and oxide-derived Au respectively. Reproduced with permission from ref. [55]. Copyright 2012, American Chemical Society.

The undercoordinated site is generally considered to possess dramatic catalytic activity.[46,47] This is mainly due to the presence of unpaired electrons and the positively or negatively charged groups. These groups are chemically unstable and possess high affinity with other molecules involved in the reaction, thus it is facile for them to form reaction intermediates with the absorbed reactant.[48] Undercoordinated sites are generally located in material surface, grain boundaries and defects, including intrinsic and structural defects.[49,50] The structural control of the electrode surface is regarded as a reasonable way to increase the catalytically active undercoordinated sites.[46,47,51] Moreover, for metal-free carbon-based electrodes, the introduction of heteroatoms is also an effective way to provide additional undercoordinated sties in carbon frameworks and thereby enhance the catalytic activity for eCO_2RR.[52,53]

The importance of the metallic oxide to the performance of eCO_2RR was evaluated by a series of investigations from Kanan group.[54–56] In order to verify the function of

the metallic oxide layer on the Sn electrode for eCO_2RR, firstly, acid was used to etch the native SnO_x layer on the electrode surface to prepare a pure Sn electrode. Then, compared eCO_2RRs were further carried out on the Sn electrodes with or without the native SnO_x layer. It was found that the catalytic activity for eCO_2RR on the pure Sn electrode was extremely poor, and when a native SnO_x layer was on the surface, the performance of eCO_2RR could be greatly improved.[54] This indicates that the presence of metallic oxide plays a decisive role in the eCO_2RR on Sn electrode. In subsequent researches, it was further found that the oxide-derived Au and Cu electrodes obtained by the reduction of corresponding oxides also possess better catalytic activity for eCO_2RR than the initial metal electrodes.[55,56] The improved catalytic activity for eCO_2RR was attributed to the stabilization of $CO_2^{\bullet-}$ intermediate on the oxidized electrode surface (Figure 1.4 B). Besides, Zhou group also declared that the performance of eCO_2RR on the Sn electrode benefits from the oxide layer with an appropriate thickness.[57] These researches demonstrated that the oxidized electrode surface is another catalytic active site for eCO_2RR.

1.3 Boron-doped diamond electrodes

1.3.1 Structure and preparation

Diamond is a non-metallic material composed of carbon atoms according to the crystal structure of diamond cubic. Due to its wide band gap of 5.6 eV, the conductivity of diamond in its intrinsic state is similar to that of an insulator.[58] When diamond is doped with heteroatoms, the conductivity of it will be gradually improved. In the case of heavy doping, the conductivity of diamond can even reach the same level with metals.[59,60] This makes it possible for doped diamond to be used as electrodes in electrochemistry.

Chemical vapor deposition (CVD) is a well-known method for the production of high-quality BDD electrodes, in which high temperature and low pressure are commonly required for the deposition. In the synthesis of BDD by CVD, with the support of extremely high energy, the reactants are broken down, excited, ionized, and even decomposed to generate the active reaction region, called plasma. Then the ionized or atomized reactants form slow and orderly deposition on the substrate so as to boost the growth of sp^3 diamond film. As a side effect, the various complex chemical reactions involved in this process also result in the generation of volatile by-products. In order to solve this weakness, along with the growth of BDD, continuous hydrogen-

gas flow is adopted to remove the main by-product, graphite. Carbon sources used in the formation of CVD BDD include acetone, methane and methanol, etc. And trimethoxyborane ($B(OCH_3)_3$), trimethylboron ($B(CH_3)_3$) and B_2O_3 can be utilized as the boron source. Si, Nb, Mo, W and Ti are commonly chosen as substrates. Before the deposition, as a pretreatment, the substrate should be polished by diamond powder to make scratches which is the active sites for nucleation. Energy sources for CVD include hot filament, microwave power and some other high-energy routes. By using microwave plasma-assisted CVD (MPCVD), high-quality BDDs can be produced stably and efficiently. But the generated plasma area is limited by the wavelength of microwave radiation, so it is hard for MPCVD to achieve the large-area growth of BDD. The area of BDD films prepared by hot filament-assisted CVD can reach about 0.5 m^2. But this approach only can be applied when the decomposition temperature of the reactants is much higher than the deposition temperature of BDD. In this thesis, the BDD electrodes mentioned in chapter 2, 3 and 4 are synthesized based on the MPCVD.

1.3.2 Electrochemical properties

In general, BDD is recognized as an inert electrode which is not favorable to adsorption. The low reaction activity of BDD for hydrogen evolution, oxygen evolution and chlorine evolution results in a wide potential window, low background current, and low capacitance in aqueous solution compared to other electrodes (Figure 1.5).[61] In addition, BDD exhibits extremely chemical stability and resistance to corrosion during the long-term electrolysis.[62] These features make BDD an ideal electrode material for electroanalytical and sensor application.

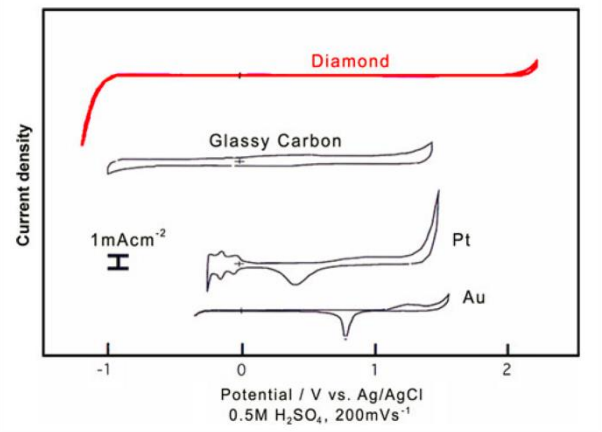

Figure 1.5 The compared potential windows showing the different electrochemical property of representative electrodes. Reproduced with permission from ref. [61]. Copyright 2010, Springer.

The surfaces of sp^3 diamond structures are commonly occupied by hydrogen or oxygen terminations. When the surface is dominated by hydrogen terminations, the BDD electrode is hydrophobic and exhibits outstanding reversibility for electrochemical redox reactions and high sensitivity for electrochemical sensing.[63] On the other hand, oxygen-terminated BDDs are proved to be hydrophilic and possess wider potential windows and lower background currents in aqueous solutions than hydrogenated BDDs.[64] Moreover, the ratio of H/O terminations on the BDD surface can be readily altered by simple electrochemical means so as to meet the requirements of specific chemical applications.

The sp^2 carbon species are usually considered to be impurities in BDD, which decrease the potential window and cause undesired disturbance to the background current. However, in the case of BDD with low boron concentration, the increase of sp^2 carbon species has been proved to be effective in broadening the potential window.[65] This property is partially attributed to the large amount of surface oxygen, high work function, low carrier densities and the presence of various sp^2 species.

1.3.3 Performance on electrochemical CO_2 reduction

In the researches concerning eCO_2RR, the hydrogen evolution reaction is considered to be the main competing reaction. In view of the low catalytic activity on BDD electrodes for hydrogen evolution, BDD-based eCO_2RR is expected to possess higher kinetic reactivity than hydrogen evolution reactions in aqueous solutions. Indeed, in the electrolysis system of flow cell, BDD exhibits over 90% Faradaic efficiency for the eCO_2RR with formic acid as the main product, and this highly selective eCO_2RR can be maintained for more than 24h (Figure 1.6 A).[66] In the work by Ikemiya et al., the performance of BDD in long-term eCO_2RR was further investigated.[67] When the reaction is performed at a low current density of -2 mA cm^{-2}, the eCO_2RR on BDD can sustain the Faradaic efficiency of over 80% for at least 48 h, and when the current density is increased to -20 mA cm^{-2}, the Faradaic efficiency for eCO_2RR will be dropped from 90% to 50% within 24 h. Interestingly, this reduced eCO_2RR activity can be recovered by a simple oxidative treatment in 20 min. This work, on the one hand, shows the possibility for the industrial application of long-term BDD-based eCO_2RR, and on the other hand, it indicates that the catalytic activity of the BDD-based eCO_2RR for formic acid production depends largely on the oxygen-containing functional groups on the surface.

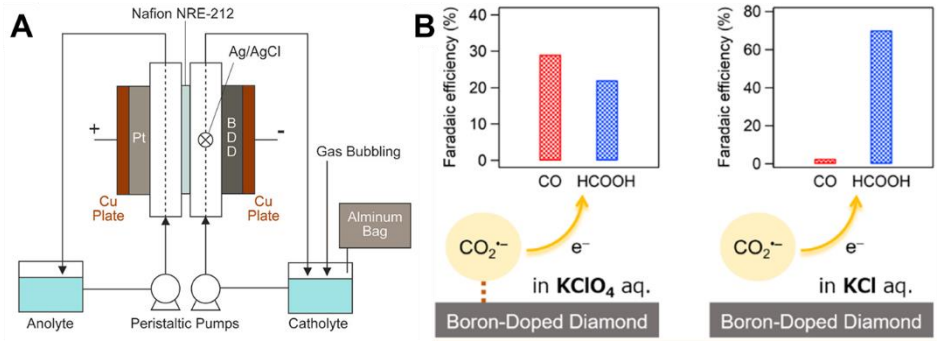

Figure 1.6 (A) Configuration of the BDD-based electrochemical CO_2 reduction system. Reproduced with permission from [66]. Copyright 2018, WILEY-VCH. (B) Schematic diagram showing the switchable product selectivity of the BDD electrodes in different solutions. Reproduced with permission from ref. [68]. Copyright 2019, American Chemical Society.

As mentioned above, BDD is generally considered to be an electrode with poor adsorption for reactants. This feature coincides with the current understanding of the eCO_2RR mechanism for the production of formic acid. Thus, the high selectivity of eCO_2RR for formic acid production on BDD seems reasonable and predictable. Unexpectedly, when the BDD-based eCO_2RR was carried out in $KClO_4$ solution, strong selectivity for CO production was observed (Figure 1.6 B). This performance was investigated by Tomisaki et al., and the reason of it was explained as the enhanced adsorption of $CO_2^{\bullet-}$ on BDD in $KClO_4$ solution.[68] Hence, it can be seen that the products of eCO_2RR on BDD can be readily controlled by the selection of electrolyte.

The fabrication of structural defects and the introduction of heteroatoms in electrode materials have been considered as effective approaches to increase the catalytically active undercoordinated sites for eCO_2RR.[25,46,48,50] However, according to the researches of Xu et al., the undercoordinated sites caused by the further doping of heteroatoms or by introducing sp^2 species failed to improve the catalytic activity of eCO_2RR on BDD.[69,70] Therefore, more mechanistic investigations should be performed to reveal the eCO_2RR processes on BDD.

As a summary of the investigations on the product selectivity in the process of eCO_2RR on BDD, referring to the above previous researches, boron-doping concentration and the species of electrolyte were considered to be two crucial factors. The boron-doping concentration of 0.1% and KCl solution are more beneficial to the production of formic acid, and when the boron-doping concentration is 1% and the electrolyte is set as $KClO_4$ solution, the Faradaic efficiency for CO production will be improved. In this thesis, we further investigated the effects on eCO_2RR which were

caused by various surface states or surface terminations on BDD electrode.

1.4 Outline of the thesis

BDD electrodes possess the advantages of low raw-material cost, non-toxic, long-term stability and strong corrosion resistance. These features are highly competitive especially when compared with conventional metal electrodes.[71] Moreover, in eCO_2RR, over 90% Faradaic efficiency have been achieved by BDD-based electrolyzer. However, the mechanistic details of the BDD-based eCO_2RR is still not clear enough. Here, we investigate the energy conversion efficiency (chapter 2), reaction pathways (chapter 3) and the possible catalytic sites (chapter 4) for the BDD-based eCO_2RR. It is hoped that these researches will enrich the understanding of the eCO_2RR process on BDD electrodes.

In chapter 2, we fabricated a CO_2 electrolyzer in order to investigate the energy requirements and the electrical-to-chemical energy conversion efficiency obtained when using BDD as the cathode. The main product in the electrochemical reduction of CO_2 using a BDD electrode was formic acid, with a Faradaic efficiency of 96%. The electrical-to-chemical energy conversion efficiency was investigated at various bias voltages, and it reached 43%, very close to the predicted maximum value, at a cell voltage of 3 V. If the secondary products, hydrogen and carbon monoxide, are also considered, the total electrical-to-chemical energy conversion efficiency was as much as 45%.[22]

In chapter 3, a self-activation process was introduced in the BDD-based eCO_2RR to reveal the reaction pathway for formic acid production. By means of an initial eCO_2RR, both the reaction current and Faradaic efficiency of the eCO_2RR on BDD electrodes were significantly improved. Here, this effect is referred to as the self-activation of BDD. Generally, the generation of $CO_2^{\bullet-}$ is the most recognized pathway leading to the formation of hydrocarbons and oxygenated products. However, the self-activation process enabled the eCO_2RR to take place at a low potential, i.e., a low energy, where $CO_2^{\bullet-}$ is hardly produced. In this work, we found that unidentate carbonate and carboxylic groups were identified as intermediates during self-activation. Increasing the amount of these intermediates via the self-activation process enhances the performance of eCO_2RR. We further evaluated this effect in long-term experiments using a CO_2 electrolyzer for formic acid production and found that the electrical-to-

chemical energy conversion efficiency reached 50.2% after the BDD self-activation process.[72]

In chapter 4, the possible source of the catalytic site for CO production in the BDD-based eCO_2RR was investigated. In the mechanistic investigations of eCO_2RR, the undercoordinated site and oxidized metals are generally considered as the most likely sources of catalytic sites. However, in the eCO_2RR based on BDD electrodes, the modification for these factors have no favorable effect on the catalytic activity. We further found that by means of electrochemical methods, when the surface of BDD electrodes is in a stable reduction state, the catalytic activity of eCO_2RR for CO production is the best. The Faradaic efficiency for CO production was increased up to 64%, and the corresponding production rate reached 23 μmol cm^{-2} h^{-1}, which was more than three times than the standard reduction set as comparison. This work demonstrates that the catalytic sites for eCO_2RR can also originate from the reduced electrode surface.

1.5 References

(1) Seneviratne, S. I.; Zhang, X.; Adnan, M.; Badi, W.; Dereczynski, C.; Di Luca, A.; Ghosh, S.; Iskandar, I.; Kossin, J.; Lewis, S.; Otto, F.; Pinto, I.; Satoh, M.; Vicente-Serrano, S. M.; Wehner, M.; Zhou, B. Weather and Climate Extreme Events in a Changing Climate. *Clim. Chang. 2021 Phys. Sci. Basis. Contrib. Work. Gr. I to Sixth Assess. Rep. Intergov. Panel Clim. Chang.* **2021**, 1513–1766.

(2) IPCC. *Climate Change 2021: The Physical Science Basis - Summary for the Policymakers (Working Group I)*; 2021, in press.

(3) United Nations Environment Programme. *Emissions Gap Report 2021: The Heat Is On – A World of Climate*; 2021, pp 36.

(4) Rogelj, J.; Meinshausen, M.; Schaeffer, M.; Knutti, R.; Riahi, K. Impact of Short-Lived Non-CO_2 mitigation on Carbon Budgets for Stabilizing Global Warming. *Environ. Res. Lett.* **2015**, *10* (7), 075001.

(5) Hilaire, J.; Minx, J. C.; Callaghan, M. W.; Edmonds, J.; Luderer, G.; Nemet, G. F.; Rogelj, J.; del Mar Zamora, M. Negative Emissions and International Climate Goals—Learning from and about Mitigation Scenarios. *Clim. Change* **2019**, *157* (2), 189–219.

(6) Sheet, E. P. A. F. Social Cost of Carbon. *High. Educ. Whisperer* **2016**, *December*, 1–5.

(7) Nordhaus, W. D. Revisiting the Social Cost of Carbon. *Proc. Natl. Acad. Sci. U. S. A.* **2017**, *114* (7), 1518–1523.

(8) Chen, C.; Khosrowabadi Kotyk, J. F.; Sheehan, S. W. Progress toward Commercial Application of Electrochemical Carbon Dioxide Reduction. *Chem* **2018**, *4* (11), 2571–2586.

(9) López-Periago, A. M.; Fraile, J.; López-Aranguren, P.; Vega, L. F.; Domingo, C. CO_2 Capture Efficiency and Carbonation/Calcination Kinetics of Micro and Nanosized Particles of Supercritically Precipitated Calcium Carbonate. *Chem. Eng. J.* **2013**, *226*, 357–366.

(10) Quadrelli, E. A.; Centi, G.; Duplan, J. L.; Perathoner, S. Carbon Dioxide Recycling: Emerging Large-Scale Technologies with Industrial Potential. *ChemSusChem* **2011**, *4* (9), 1194–1215.

(11) Fiorani, G.; Guo, W.; Kleij, A. W. Sustainable Conversion of Carbon Dioxide: The Advent of Organocatalysis. *Green Chem.* **2015**, *17* (3), 1375–1389.

(12) Tu, W.; Zhou, Y.; Zou, Z. Photocatalytic Conversion of CO_2 into Renewable Hydrocarbon Fuels: State-of-the-Art Accomplishment, Challenges, and Prospects. *Adv. Mater.* **2014**, *26* (27), 4607–4626.

(13) Prabhu, P.; Jose, V.; Lee, J. M. Heterostructured Catalysts for Electrocatalytic and Photocatalytic Carbon Dioxide Reduction. *Adv. Funct. Mater.* **2020**, *30*, 1910768.

(14) Habisreutinger, S. N.; Schmidt-Mende, L.; Stolarczyk, J. K. Photocatalytic Reduction of CO_2 on TiO_2 and Other Semiconductors. *Angew. Chemie - Int. Ed.* **2013**, *52* (29), 7372–7408.

(15) Chen, C. Y.; Yeh, K. L.; Aisyah, R.; Lee, D. J.; Chang, J. S. Cultivation, Photobioreactor Design and Harvesting of Microalgae for Biodiesel Production: A Critical Review. *Bioresour. Technol.* **2011**, *102* (1), 71–81.

(16) Alissandratos, A.; Easton, C. J. Biocatalysis for the Application of CO_2 as a Chemical Feedstock. *Beilstein J. Org. Chem.* **2015**, *11*, 2370–2387.

(17) Lam, M. K.; Lee, K. T. Microalgae Biofuels: A Critical Review of Issues, Problems and the Way Forward. *Biotechnol. Adv.* **2012**, *30* (3), 673–690.

(18) Savile, C. K.; Lalonde, J. J. Biotechnology for the Acceleration of Carbon Dioxide Capture and Sequestration. *Curr. Opin. Biotechnol.* **2011**, *22* (6), 818–823.

(19) Shi, L. E. I.; Yang, G.; Tao, K. A. I. Reforming with Methane and New Route of Low-Temperature Methanol Synthesis. *Acc. Chem. Res.* **2013**, *46* (8), 2–11.

(20) Saeidi, S.; Amin, N. A. S.; Rahimpour, M. R. Hydrogenation of CO_2 to Value-Added Products - A Review and Potential Future Developments. *J. CO_2 Util.* **2014**, *5*, 66–81.

(21) Kumar, N.; Shojaee, M.; Spivey, J. J. Catalytic Bi-Reforming of Methane: From Greenhouse Gases to Syngas. *Curr. Opin. Chem. Eng.* **2015**, *9*, 8–15.

(22) Du, J.; Fiorani, A.; Einaga, Y. An Efficient, Formic Acid Selective CO_2 electrolyzer with a Boron-Doped Diamond Cathode. *Sustain. Energy Fuels* **2021**, *5* (10), 2590–2594.

(23) Gurudayal; Bullock, J.; Srankó, D. F.; Towle, C. M.; Lum, Y.; Hettick, M.; Scott, M. C.; Javey, A.; Ager, J. Efficient Solar-Driven Electrochemical CO_2 Reduction to Hydrocarbons and Oxygenates. *Energy Environ. Sci.* **2017**, *10* (10), 2222–2230.

(24) Verma, S.; Kim, B.; Jhong, H. R. M.; Ma, S.; Kenis, P. J. A. A Gross-Margin Model for Defining Technoeconomic Benchmarks in the Electroreduction of CO_2. *ChemSusChem* **2016**, *9* (15), 1972–1979.

(25) Duan, X.; Xu, J.; Wei, Z.; Ma, J.; Guo, S.; Wang, S.; Liu, H.; Dou, S. Metal-Free Carbon Materials for CO_2 Electrochemical Reduction. *Adv. Mater.* **2017**, *29*, 1701784.

(26) Bushuyev, O. S.; De Luna, P.; Dinh, C. T.; Tao, L.; Saur, G.; van de Lagemaat, J.; Kelley, S. O.; Sargent, E. H. What Should We Make with CO_2 and How Can We Make It? *Joule* **2018**, *2* (5), 825–832.

(27) Higgins, D.; Hahn, C.; Xiang, C.; Jaramillo, T. F.; Weber, A. Z. Gas-Diffusion Electrodes for Carbon Dioxide Reduction: A New Paradigm. *ACS Energy Lett.* **2019**, *4* (1), 317–324.

(28) White, J. L.; Baruch, M. F.; Pander, J. E.; Hu, Y.; Fortmeyer, I. C.; Park, J. E.; Zhang, T.; Liao, K.; Gu, J.; Yan, Y.; Shaw, T. W.; Abelev, E.; Bocarsly, A. B. Light-Driven Heterogeneous Reduction of Carbon Dioxide: Photocatalysts and Photoelectrodes. *Chem. Rev.* **2015**, *115* (23), 12888–12935.

(29) Wang, Y.; Liu, J.; Wang, Y.; Wang, Y.; Zheng, G. Efficient Solar-Driven Electrocatalytic CO_2 Reduction in a Redox-Medium-Assisted System. *Nat. Commun.* **2018**, *9*, 5003.

(30) Schreier, M.; Héroguel, F.; Steier, L.; Ahmad, S.; Luterbacher, J. S.; Mayer, M. T.; Luo, J.; Grätzel, M. Solar Conversion of CO_2 to CO Using Earth-Abundant Electrocatalysts Prepared by Atomic Layer Modification of CuO. *Nat. Energy* **2017**, *2* (7), 17087.

(31) Cheng, W. H.; Richter, M. H.; Sullivan, I.; Larson, D. M.; Xiang, C.; Brunschwig, B. S.; Atwater, H. A. CO_2 Reduction to CO with 19% Efficiency in a Solar-Driven Gas Diffusion Electrode Flow Cell under Outdoor Solar Illumination. *ACS Energy Lett.* **2020**, *5*, 470–476.

(32) Whipple, D. T.; Kenis, P. J. A. Prospects of CO_2 Utilization via Direct Heterogeneous Electrochemical Reduction. *J. Phys. Chem. Lett.* **2010**, *1* (24), 3451–3458.

(33) Kortlever, R.; Shen, J.; Schouten, K. J. P.; Calle-Vallejo, F.; Koper, M. T. M. Catalysts and Reaction Pathways for the Electrochemical Reduction of Carbon Dioxide. *J. Phys. Chem. Lett.* **2015**, *6* (20), 4073–4082.

(34) Medford, A. J.; Vojvodic, A.; Hummelshøj, J. S.; Voss, J.; Abild-Pedersen, F.; Studt, F.; Bligaard, T.; Nilsson, A.; Nørskov, J. K. From the Sabatier Principle to a Predictive Theory of Transition-Metal Heterogeneous Catalysis. *J. Catal.* **2015**, *328*, 36–42.

(35) Zhu, D. D.; Liu, J. L.; Qiao, S. Z. Recent Advances in Inorganic Heterogeneous Electrocatalysts for Reduction of Carbon Dioxide. *Adv. Mater.* **2016**, *28* (18), 3423–3452.

(36) Zhang, W.; Hu, Y.; Ma, L.; Zhu, G.; Wang, Y.; Xue, X.; Chen, R.; Yang, S.; Jin, Z. Progress and Perspective of Electrocatalytic CO_2 Reduction for Renewable Carbonaceous Fuels and Chemicals. *Adv. Sci.* **2018**, *5* (1), 1700275.

(37) Kou, Z.; Li, X.; Wang, T.; Ma, Y.; Zang, W.; Nie, G.; Wang, J. Fundamentals, On-Going Advances and Challenges of Electrochemical Carbon Dioxide Reduction. *Electrochem. Energy Rev.* **2022**, *5* (1), 82–111.

(38) Rosen, B. A.; Salehi-Khojin, A.; Thorson, M. R.; Zhu, W.; Whipple, D. T.; Kenis, P. J. A.; Masel, R. I. Ionic Liquid-Mediated Selective Conversion of CO_2 to CO at Low Overpotentials. *Science* **2011**, *334* (6056), 643–644.

(39) Kortlever, R.; Peters, I.; Koper, S.; Koper, M. T. M. Electrochemical CO_2 Reduction to Formic Acid at Low Overpotential and with High Faradaic Efficiency on Carbon-Supported Bimetallic Pd-Pt Nanoparticles. *ACS Catal.* **2015**, *5* (7), 3916–3923.

(40) Costentin, C.; Robert, M.; Savéant, J. M. Catalysis of the Electrochemical Reduction of Carbon Dioxide. *Chem. Soc. Rev.* **2013**, *42* (6), 2423–2436.

(41) Feaster, J. T.; Shi, C.; Cave, E. R.; Hatsukade, T.; Abram, D. N.; Kuhl, K. P.; Hahn, C.; Nørskov, J. K.; Jaramillo, T. F. Understanding Selectivity for the Electrochemical Reduction of Carbon Dioxide to Formic Acid and Carbon

Monoxide on Metal Electrodes. *ACS Catal.* **2017**, *7* (7), 4822–4827.

(42) Daiyan, R.; Lu, X.; Ng, Y. H.; Amal, R. Liquid Hydrocarbon Production from CO_2 : Recent Development in Metal-Based Electrocatalysis. *ChemSusChem* **2017**, *10* (22), 4342–4358.

(43) Ting, L. R. L.; Yeo, B. S. Recent Advances in Understanding Mechanisms for the Electrochemical Reduction of Carbon Dioxide. *Curr. Opin. Electrochem.* **2018**, *8*, 126–134.

(44) Yoo, J. S.; Christensen, R.; Vegge, T.; Nørskov, J. K.; Studt, F. Theoretical Insight into the Trends That Guide the Electrochemical Reduction of Carbon Dioxide to Formic Acid. *ChemSusChem* **2016**, *9* (4), 358–363.

(45) Baruch, M. F.; Pander, J. E.; White, J. L.; Bocarsly, A. B. Mechanistic Insights into the Reduction of CO_2 on Tin Electrodes Using in Situ ATR-IR Spectroscopy. *ACS Catal.* **2015**, *5* (5), 3148–3156.

(46) Mariano, R. G.; Kang, M.; Wahab, O. J.; McPherson, I. J.; Rabinowitz, J. A.; Unwin, P. R.; Kanan, M. W. Microstructural Origin of Locally Enhanced CO_2 Electroreduction Activity on Gold. *Nat. Mater.* **2021**, *20* (7), 1000–1006.

(47) Mezzavilla, S.; Horch, S.; Stephens, I. E. L.; Seger, B.; Chorkendorff, I. Structure Sensitivity in the Electrocatalytic Reduction of CO_2 with Gold Catalysts. *Angew. Chemie - Int. Ed.* **2019**, *58* (12), 3774–3778.

(48) Zhang, L.; Ng, M. L.; Vojvodic, A. Role of Undercoordinated Sites for the Catalysis in Confined Spaces Formed by Two-Dimensional Material Overlayers. *J. Phys. Chem. Lett.* **2020**, *11*, 9400–9407.

(49) Wang, W.; Shang, L.; Chang, G.; Yan, C.; Shi, R.; Zhao, Y.; Waterhouse, G. I. N.; Yang, D.; Zhang, T. Intrinsic Carbon-Defect-Driven Electrocatalytic Reduction of Carbon Dioxide. *Adv. Mater.* **2019**, *31*, 1808279.

(50) Gong, Q.; Ding, P.; Xu, M.; Zhu, X.; Wang, M.; Deng, J.; Ma, Q.; Han, N.; Zhu, Y.; Lu, J.; Feng, Z.; Li, Y.; Zhou, W.; Li, Y. Structural Defects on Converted Bismuth Oxide Nanotubes Enable Highly Active Electrocatalysis of Carbon Dioxide Reduction. *Nat. Commun.* **2019**, *10*, 2807.

(51) Kang, X.; Li, L.; Sheveleva, A.; Han, X.; Li, J.; Liu, L.; Tuna, F.; McInnes, E. J. L.; Han, B.; Yang, S.; Schröder, M. Electro-Reduction of Carbon Dioxide at Low over-Potential at a Metal–Organic Framework Decorated Cathode. *Nat. Commun.* **2020**, *11*, 5464.

(52) Song, Y.; Chen, W.; Zhao, C.; Li, S.; Wei, W.; Sun, Y. Metal-Free Nitrogen-Doped Mesoporous Carbon for Electroreduction of CO_2 to Ethanol. *Angew.*

Chemie - Int. Ed. **2017**, *56* (36), 10840–10844.

(53) Wu, J.; Ma, S.; Sun, J.; Gold, J. I.; Tiwary, C.; Kim, B.; Zhu, L.; Chopra, N.; Odeh, I. N.; Vajtai, R.; Yu, A. Z.; Luo, R.; Lou, J.; Ding, G.; Kenis, P. J. A.; Ajayan, P. M. A Metal-Free Electrocatalyst for Carbon Dioxide Reduction to Multi-Carbon Hydrocarbons and Oxygenates. *Nat. Commun.* **2016**, *7*, 13869.

(54) Chen, Y.; Kanan, M. W. Tin Oxide Dependence of the CO_2 Reduction Efficiency on Tin Electrodes and Enhanced Activity for Tin/Tin Oxide Thin-Film Catalysts. *J. Am. Chem. Soc.* **2012**, *134* (4), 1986–1989.

(55) Chen, Y.; Li, C. W.; Kanan, M. W. Aqueous CO_2 Reduction at Very Low Overpotential on Oxide-Derived Au Nanoparticles. *J. Am. Chem. Soc.* **2012**, *134* (49), 19969–19972.

(56) Li, C. W.; Kanan, M. W. CO_2 Reduction at Low Overpotential on Cu Electrodes Resulting from the Reduction of Thick Cu_2O Films. *J. Am. Chem. Soc.* **2012**, *134* (17), 7231–7234.

(57) Wu, J.; Risalvato, F. G.; Ma, S.; Zhou, X. D. Electrochemical Reduction of Carbon Dioxide III. the Role of Oxide Layer Thickness on the Performance of Sn Electrode in a Full Electrochemical Cell. *J. Mater. Chem. A* **2014**, *2* (6), 1647–1651.

(58) Shi, Z.; Dao, M.; Tsymbalov, E.; Shapeev, A.; Li, J.; Suresh, S. Metallization of Diamond. *Proc. Natl. Acad. Sci. U. S. A.* **2020**, *117* (40), 24634–24639.

(59) Gonon, P.; Gheeraert, E.; Deneuville, A.; Fontaine, F.; Abello, L.; Lucazeau, G. Characterization of Heavily B-Doped Polycrystalline Diamond Films Using Raman Spectroscopy and Electron Spin Resonance. *J. Appl. Phys.* **1995**, *78* (12), 7059–7062.

(60) Tsay, Y. F.; Ananthanarayanan, K. P.; Gielisse, P. J.; Mitra, S. S. Electrical Conductivity of Heavily Doped Diamond. *J. Appl. Phys.* **1972**, *43* (9), 3677–3682.

(61) Einaga, Y. Diamond Electrodes for Electrochemical Analysis. *J. Appl. Electrochem.* **2010**, *40* (10), 1807–1816.

(62) Kashiwada, T.; Watanabe, T.; Ootani, Y.; Tateyama, Y.; Einaga, Y. A Study on Electrolytic Corrosion of Boron-Doped Diamond Electrodes When Decomposing Organic Compounds. *ACS Appl. Mater. Interfaces* **2016**, *8* (42), 28299–28305.

(63) Kasahara, S.; Natsui, K.; Watanabe, T.; Yokota, Y.; Kim, Y.; Iizuka, S.; Tateyama, Y.; Einaga, Y. Surface Hydrogenation of Boron-Doped Diamond

Electrodes by Cathodic Reduction. *Anal. Chem.* **2017**, *89* (21), 11341–11347.

(64) Yagi, I.; Notsu, H.; Kondo, T.; Tryk, D. A.; Fujishima, A. Electrochemical Selectivity for Redox Systems at Oxygen-Terminated Diamond Electrodes. *J. Electroanal. Chem.* **1999**, *473* (1), 173–178.

(65) Xu, J.; Yokota, Y.; Wong, R. A.; Kim, Y.; Einaga, Y. Unusual Electrochemical Properties of Low-Doped Boron-Doped Diamond Electrodes Containing Sp^2 Carbon. *J. Am. Chem. Soc.* **2020**, *142* (5), 2310–2316.

(66) Natsui, K.; Iwakawa, H.; Ikemiya, N.; Nakata, K.; Einaga, Y. Stable and Highly Efficient Electrochemical Production of Formic Acid from Carbon Dioxide Using Diamond Electrodes. *Angew. Chemie - Int. Ed.* **2018**, *57* (10), 2639–2643.

(67) Ikemiya, N.; Natsui, K.; Nakata, K.; Einaga, Y. Long-Term Continuous Conversion of CO_2 to Formic Acid Using Boron-Doped Diamond Electrodes. *ACS Sustain. Chem. Eng.* **2018**, *6* (7), 8108–8112.

(68) Tomisaki, M.; Kasahara, S.; Natsui, K.; Ikemiya, N.; Einaga, Y. Switchable Product Selectivity in the Electrochemical Reduction of Carbon Dioxide Using Boron-Doped Diamond Electrodes. *J. Am. Chem. Soc.* **2019**, *141* (18), 7414–7420.

(69) Xu, J.; Natsui, K.; Naoi, S.; Nakata, K.; Einaga, Y. Effect of Doping Level on the Electrochemical Reduction of CO_2 on Boron-Doped Diamond Electrodes. *Diam. Relat. Mater.* **2018**, *86* (March), 167–172.

(70) Xu, J.; Einaga, Y. Effect of Sp^2 Species in a Boron-Doped Diamond Electrode on the Electrochemical Reduction of CO_2. *Electrochem. commun.* **2020**, *115* (April), 106731.

(71) Hori, Y. *Electrochemical CO_2 Reduction on Metal Electrodes*; Springer: New York, 2008; pp 89-189.

(72) Du, J.; Fiorani, A.; Inagaki, T.; Otake, A.; Murata, M.; Hatanaka, M.; Einaga, Y. A New Pathway for CO_2 Reduction Relying on the Self-Activation Mechanism of Boron-Doped Diamond Cathode . *JACS Au* **2022**, *2*, 1375-1382.

Chapter 2

An Efficient, Formic Acid Selective CO_2 Electrolyzer with a Boron-doped Diamond Cathode

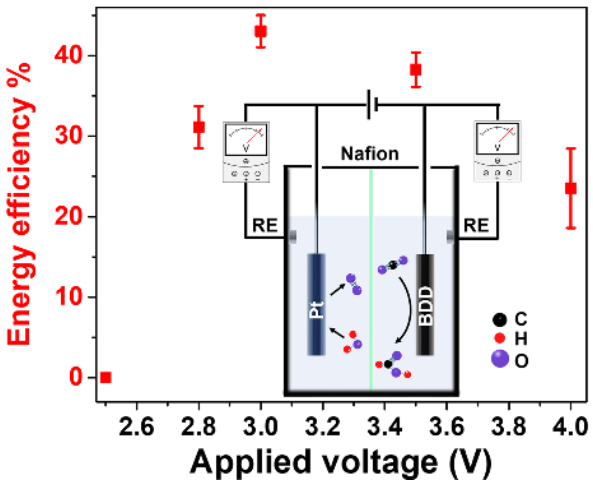

Reproduced with permission from Du, J.; Fiorani, A.; Einaga, Y. An Efficient, Formic Acid Selective CO_2 electrolyzer with a Boron-Doped Diamond Cathode. *Sustain. Energy Fuels* **2021**, *5* (10), 2590–2594. Copyright 2021, The Royal Society of Chemistry.

2.1 Introduction

The desire for carbon-neutral energy schemes has sparked increasing interest in a number of different strategies for the utilization of carbon dioxide (CO_2).[1] Among these several strategies, the electrochemical carbon dioxide reduction reaction (eCO_2RR) offers the possibility for the production of carbon monoxide,[2] methanol and small hydrocarbons (C_2-C_3), which can be used as feedstock for further chemical processes.[3] In particular, formic acid (FA) production is very attractive since it can be used as a reversible vector for the storage and release of H_2,[4] or applied directly in a fuel cell.[5] From this viewpoint, technological applications of eCO_2RR could enable the production of fuels or commodity chemicals, and the storing of excess renewable electricity. This latter point is also fundamental, since the eCO_2RR can be really sustainable only if coupled with electrical power from a renewable energy source.[6]

For a potential commercially viable application, however, the following five aspects should be considered for a CO_2 electrolyzer, especially for the electrode material: 1) affordable cost, 2) environmentally sustainable, 3) long-term stability, 4) high product selectivity, and 5) high electrical-to-chemical energy (ECE) conversion efficiency.

Traditionally, transition metals have been applied in electrochemical CO_2 reduction,[7,8] and these metals are still the electrode materials most commonly under investigation; however, solutions have to be found for cost (Pd, Au, and Ag),[9–12] toxicity (Pb, Sn, Hg, and In),[13–16] and long-term stability.[7,14,17] Cu is perhaps the best compromise in terms of cost and toxicity, but it has poor product selectivity[18,19] leading to high investment in product separation. Hybrid and hierarchical catalysts may overcome such drawbacks, but long term stability and high partial currents remain challenging goals.[20–22]

Boron-doped diamond (BDD) has been shown to be a good candidate for the cathode for CO_2 reduction,[23,24] and recently, we demonstrated its long term stability[25], resistance to corrosion[26] and high product-selectivity in the electrochemical reduction of CO_2.[27,28]. It can be fabricated with economical raw materials and does not pose any toxicity risks. Hence, the final condition to be met to enable the, potentially, commercial application of eCO_2RR, is a high ECE conversion efficiency, which needs to be evaluated in detail. Current research on CO_2 reduction with BDD focuses on three-electrode systems, where the BDD is

used as the cathode, neglecting the coupled reaction at the counter electrode. However, the ECE conversion efficiency for CO_2 reduction cannot be computed in the three-electrode configuration.[29,30]

Here, we evaluate the electrochemical performance of a CO_2 electrolyzer where a BDD electrode is used as the cathode, in order to achieve the best conditions for product selectivity and ECE conversion efficiency. In this two-electrode system, reference electrodes (RE) were used to monitor the actual potentials on both the cathode and the anode. Benefiting from this design, the energy distribution of each part in this electrolyzer can be analyzed. Through optimization of the experimental conditions, an outstanding Faradaic efficiency of 96% for the production of FA was obtained at a cell voltage (E_{cell}) of 3.5 V, although it was with E_{cell} at 3 V, that the ECE conversion efficiency reached its highest value, which was 43% for FA and 45% if all the products were included (i.e., hydrogen and carbon monoxide).[31]

2.2 Experimental section

2.2.1 Materials

KCl, Na_3PO_4 and $NaClO_4$ were purchased from Wako Pure Chemical Industries Ltd. and were used without any further purification. Formic acid for HPLC calibration was obtained from FUJIFILM Wako pure Chemical Corporation. Hydrogen and carbon monoxide for GC calibration were obtained from GL Sciences. Acetone and trimethoxyborane used in the preparation of the BDD were from TCI (Japan). Deionized water was obtained from a Simply-Lab water system (DIRECT-Q 3UV, Millipore) with a resistivity of 18.2 MΩ·cm at 25 °C.

2.2.2 BDD electrode fabrication

The BDD electrode was prepared following an established procedure.[27,28] Briefly, BDD was deposited on a Si (100) wafer substrate using a microwave plasma-assisted chemical vapor deposition (MPCVD) system (AX5400, Corns Technologies Ltd.). The concentration of boron in the BDD was set to 0.1 % and was determined by the ratio between the carbon source (acetone) and the boron source (trimethoxyborane). The exact content of boron in the BDD was further quantified by glow discharge optical emission spectroscopy (GDOES, GD-Profiler2, Horiba Ltd.)[32,33] and found to be 0.1%. The Raman spectrum was acquired using an Acton SP2500 (Princeton Instruments)

with a 532 nm laser (Figure 2.1). The Raman spectrum of the 0.1% BDD showed a narrow peak at 1332 cm^{-1} which was due to the zone-center optical phonon of diamond.[27,33] Surface morphology images of the BDD film were obtained with a scanning electron microscope (JCM-6000, JEOL). The SEM image shows homogeneous micrometer-sized diamond grains (Figure 2.2).

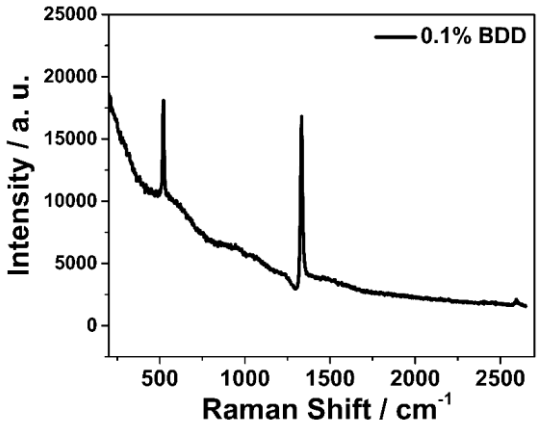

Figure 2.1 Raman spectrum for the BDD electrode with a boron content of 0.1%. Reproduced with permission from ref. [31]. Copyright 2021, The Royal Society of Chemistry.

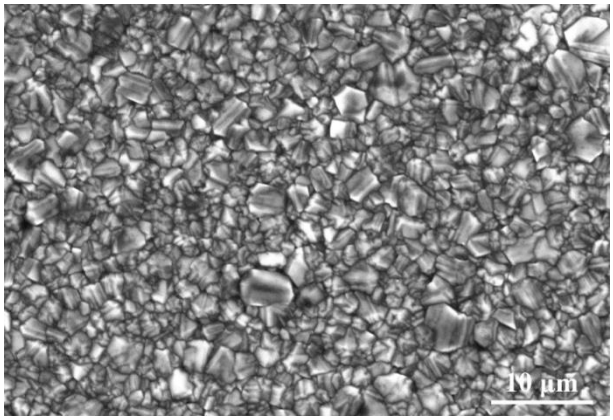

Figure 2.2 SEM micrograph of 0.1% BDD. Reproduced with permission from ref. [31]. Copyright 2021, The Royal Society of Chemistry.

2.2.3 Electrochemical tests and products analysis

Measurements were performed with a potentiostat (PGSTAT204, Metrohm Autolab) by operating the cell in a two-electrode configuration with a platinum anode (0.69 cm^2, Nilaco, JP) and BDD (0.79 cm^2) as the cathode. The anode and cathode chambers were separated by a Nafion NRE-212 (1.13 cm^2, Sigma-Aldrich) membrane and each chamber had an Ag/AgCl (saturated KCl) reference electrode to monitor the potentials of the anode and cathode. The actual connection diagram is shown in the schematic diagram below. As a pretreatment before CO_2 reduction, several cyclic voltammetry (CV) scans (including 10 cycles from a potential of -3.5 V to 3.5 V and 20 cycles from 0 V to 3.5 V with a scan rate of 0.5 V/s in 0.1 M $NaClO_4$ aqueous solution) were performed to assure reproducibility and the cleanliness of the surface of the electrodes. The catholyte and anolyte were 0.1 M KCl and 0.1 M Na_3PO_4, respectively (20 mL each). The catholyte was bubbled with N_2 for 10 min to remove oxygen and CO_2 for 60 min resulting in a CO_2-sauturated solution (Figure 2.3). During electrolysis, CO_2 bubbling was set at a flow rate of 10 ml min^{-1}.

At the end of each experiment, all of the products were quantified. Formic acid was quantified by high-performance liquid chromatography (CDD-10A, Shimadzu Corp.). The gaseous products (CO and H_2) were collected in an aluminum gas bag (GL Sciences) and quantified by gas chromatography (GC-2014, Shimadzu Corp.).

Error bars show the standard deviation (n = 3), except where otherwise stated.

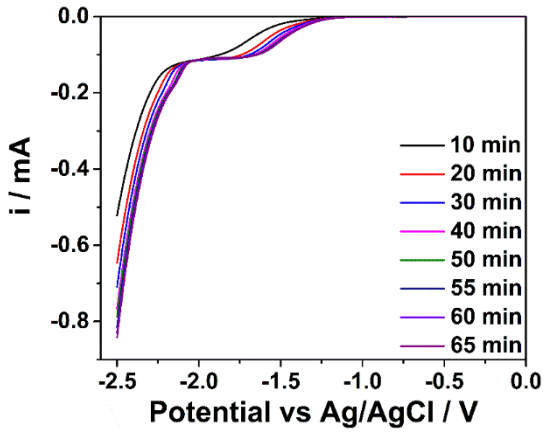

Figure 2.3 Saturation of KCl 0.1 M catholyte by CO_2 bubbling (100 mL min^{-1}). CV is performed at displayed time, with scan rate 100 mV s^{-1}. Reference electrode: Ag/AgCl(KCl sat). Reproduced with permission from ref. [31]. Copyright 2021, The Royal Society of Chemistry.

2.2.4 Electrical-to-chemical energy conversion efficiency.

The Gibbs free energy of the CO_2 reduction reaction (ΔG_r, Table 2.1) can be calculated from the following equation:

$$\Delta G_r = \Sigma G_{products} - \Sigma G_{reactants} \qquad (2.1)$$

The standard electromotive force of the cell reaction E^o can be calculated from the following equation:

$$E^\circ = -\frac{\Delta G_r}{nF} \qquad (2.2)$$

where n is the number of electrons transferred in the reaction and F is the Faraday constant (96485 C mol^{-1}). The calculated E^o of the common products from CO_2 reduction are summarized in Table 2.2.

The Faradaic efficiency (FE) can be defined by the following equation:

$$FE = \frac{\sum n_i \times F \times n^\circ mol_i}{Q} \qquad (2.3)$$

where n is the number of electrons involved in the reduction, n° mol is the number of moles of product and Q is the total charge in the electrolysis.

The ECE conversion efficiency (η_{energy}) can be evaluated using the equation below:

$$\eta_{energy} = \frac{\sum |E_i^o| \times FE_i}{E_{cell}} \qquad (2.4)$$

where E_{cell} represents the total cell voltage applied in the electrolysis. The subscript i represents the i^{th} product from CO_2 reduction.

The actual working potential applied in the electrolysis process is usually required to be higher than the standard thermodynamic potential to achieve the expected rate of reaction. Thus, when calculating the theoretical boundary of the ECE conversion efficiency for CO_2 reduction, we should take into account different applied voltages for practical applications. Of the common eCO_2RRs, the most negative standard thermodynamic potential is -1.3997 V (for the production of formic acid). This determines the theoretical maximum of the ECE conversion efficiency for CO_2 reduction at a specified voltage. The specific theoretical maximum can be calculated using equation 2.4.

Table 2.1 Standard Gibbs free energies of formation for common compounds obtained or involved in CO_2 reduction. (The standard Gibbs free energy of each compound was obtained from the Handbook of Chemistry and Physics 91st Edition.)

Compound Name	Chemical Formula	ΔG_f / kJ mol^{-1}
Carbon dioxide	CO_2 (g)	-394.4
Water	H_2O (l)	-237.1
Carbon monoxide	CO (g)	-137.2
Formic acid	HCOOH (l)	-361.4
Formaldehyde	HCHO (g)	-102.5
Methanol	CH_3OH (l)	-166.6
Methane	CH_4 (g)	-50.5
Acetaldehyde	CH_3CHO (l)	-127.6
Ethylene	C_2H_4 (g)	68.4
Ethanol	C_2H_5OH (l)	-174.8
Ethane	C_2H_6 (g)	-32.0

Table 2.2 The standard thermodynamic potentials of common products from CO_2 reduction. The minus (-) sign comes from J. W. Gibbs's definition in electrochemical thermodynamics.

Products	Reaction Equation	n	ΔG_r / kJ mol^{-1}	E^o / V
Water splitting	$H_2O \leftrightarrow H_2 + \frac{1}{2}O_2$	2	237.1	-1.229
Carbon monoxide	$CO_2 \leftrightarrow CO + \frac{1}{2}O_2$	2	257.2	-1.333
Formic acid	$CO_2 + H_2O \leftrightarrow HCOOH + \frac{1}{2}O_2$	2	270.1	-1.3997
Formaldehyde	$CO_2 + H_2O \leftrightarrow HCHO + O_2$	4	529	-1.371
Methanol	$CO_2 + 2H_2O \leftrightarrow CH_3OH + \frac{3}{2}O_2$	6	702	-1.213
Methane	$CO_2 + 2H_2O \leftrightarrow CH_4 + 2O_2$	8	818.1	-1.0599
Acetaldehyde	$2CO_2 + 2H_2O \leftrightarrow CH_3CHO + \frac{5}{2}O_2$	10	1135.4	-1.177
Ethylene	$2CO_2 + 2H_2O \leftrightarrow C_2H_4 + 3O_2$	12	1331.4	-1.15
Ethanol	$2CO_2 + 3H_2O \leftrightarrow C_2H_5OH + 3O_2$	12	1325.3	-1.145
Ethane	$2CO_2 + 3H_2O \leftrightarrow C_2H_6 + \frac{7}{2}O_2$	14	1468.1	-1.087

2.3 Results and discussion

2.3.1 CO_2 reduction in two-electrode system

First, we investigated the performance of the CO_2 electrolyzer (Figure 2.4) under different cell voltages. The CO_2 reduction reaction at the BDD cathode is coupled with the oxygen evolution reaction (OER) at the Pt anode. A reference electrode was added to each chamber, one for the anolyte and one for the catholyte, to monitor the potential of each electrode by digital voltmeters.

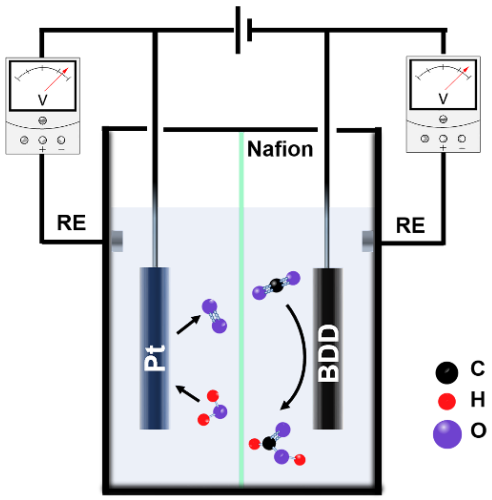

Figure 2.4 Schematic diagram showing the CO_2 electrolyzer and electrode connections. Reproduced with permission from ref. [31]. Copyright 2021, The Royal Society of Chemistry.

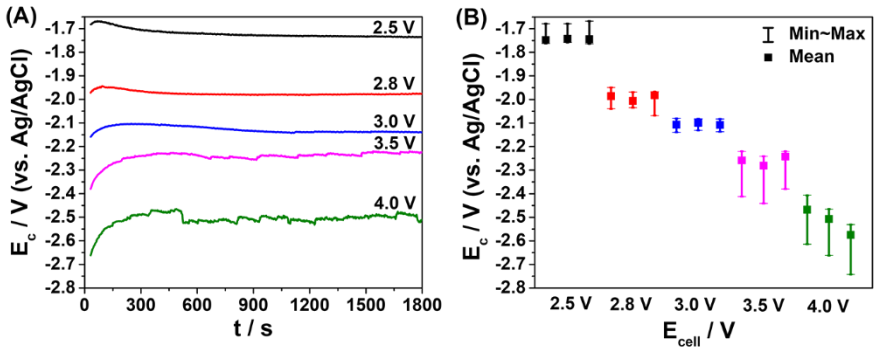

Figure 2.5 A) Measured potential at a BDD cathode during 30-min CO_2 reduction with E_{cell} set to 2.5 V, 2.8 V, 3.0 V, 3.5 V, and 4.0 V. B) Correlation between applied E_{cell} and measured E_c. The error bars show the minimum and maximum potentials measured during chronoamperometry. Reference electrode: Ag/AgCl (saturated KCl). Reproduced with permission from ref. [31]. Copyright 2021, The Royal Society of Chemistry.

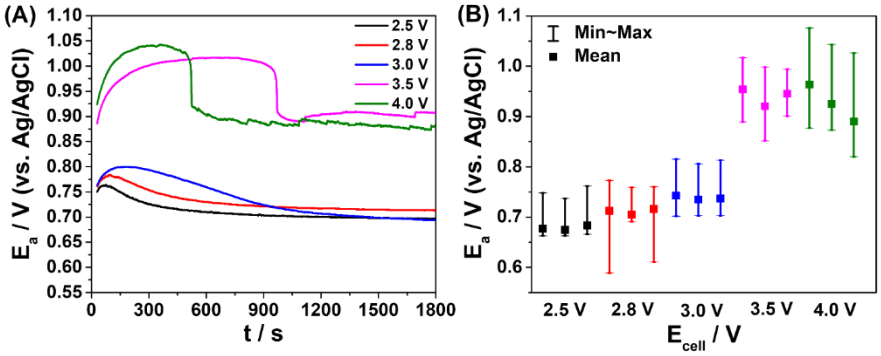

Figure 2.6 A) The potential on the Pt (anode) during 30-min CO_2 reduction at applied voltages of 2.5 V, 2.8 V, 3.0 V, 3.5 V and 4.0 V respectively. B) Statistical data of anode potentials, repeated three times at each applied voltage. E_a signifies the potential applied to the anode and E_{cell} is the voltage difference between the anode and cathode. Potentials are referred to Ag/AgCl (KCl sat). Reproduced with permission from ref. [31]. Copyright 2021, The Royal Society of Chemistry.

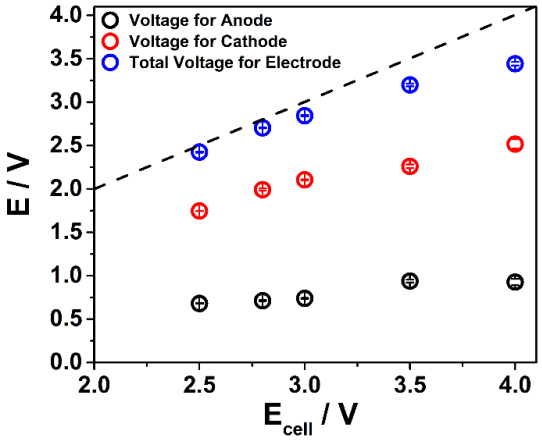

Figure 2.7 Voltage distribution in two-electrode system at various applied voltages. The dashed line shows the applied voltage. Reproduced with permission from ref. [31]. Copyright 2021, The Royal Society of Chemistry.

Figure 2.5 A shows the variation in cathode potential (E_c) (vs. Ag/AgCl) with time as the electrolysis proceeds at different values of E_{cell}, where after a short equilibration time, the cathode reaches a stable working potential. E_c was monitored as a function of E_{cell}, and this has a linear correlation in the range 2.5 - 4 V (Figure 2.5 B). The corresponding working potential of the anode (E_a) (vs. Ag/AgCl) is summarized in Figure 2.6. The two electrodes show an asymmetric potential distribution when E_{cell} is increased from 2.5 V to 4 V, since E_c gains 800 mV, while E_a only gains 260 mV (Figure 2.7). Consistent with the increase in applied E_{cell}, the current density in the electrolysis

increases from 0.2 mA/cm^{-2} to 5 mA/cm^{-2} (Figure 2.8).

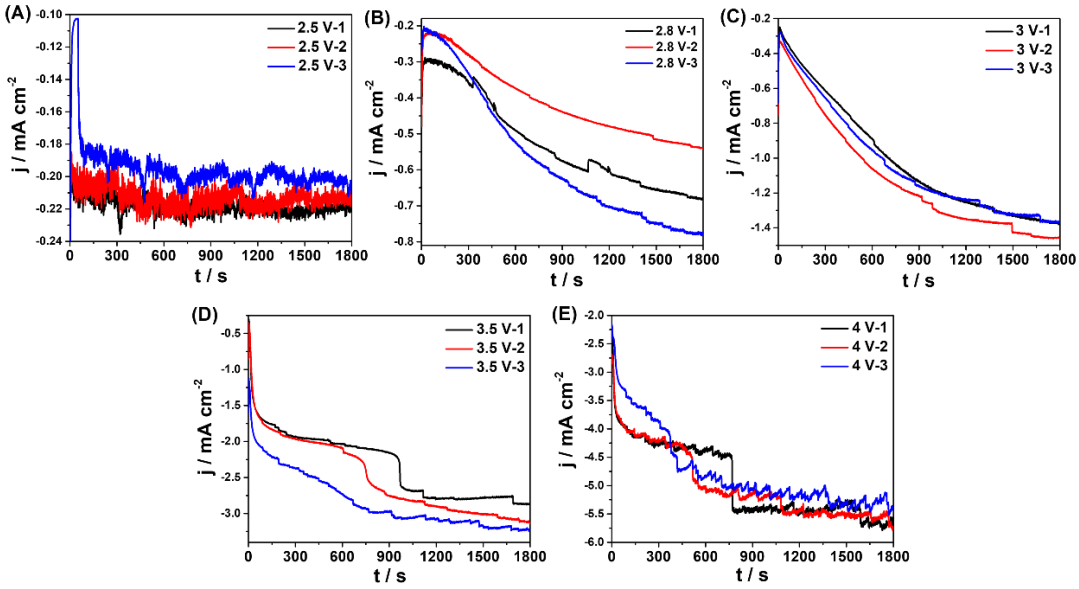

Figure 2.8 Current densities during 30-min CO_2 reduction at applied voltages of A) 2.5 V, B) 2.8 V, C)3.0 V, D) 3.5 V and E) 4.0 V. Reproduced with permission from ref. [31]. Copyright 2021, The Royal Society of Chemistry.

We further investigated the Faradaic efficiencies of the products at different E_{cell}. As shown in Figure 2.9 A and Table 2.3, the main product is formic acid, with small amounts of CO and H_2, since the hydrogen evolution reaction (HER) is a competitive reaction in CO_2 reduction. Since BDD is inert, carbon dioxide radicals ($CO_2^{\bullet-}$) are hardly absorbed on its surface;[27,34] consequently, this promotes the reduction of CO_2 to formic acid in aqueous solutions.[28,35] Furthermore, the high overpotential for hydrogen reduction results in a wide potential window and low activity towards HER.[36,37] Consequently, as E_{cell} is increased from 2.5 V to 3.5 V, increasing the applied overpotential for the reduction of CO_2 to $CO_2^{\bullet-}$,[35] the Faradaic efficiency for the production of formic acid gradually increases, reaching a maximum of 96.3 % at 3.5 V (Figure 2.9 A). At 4 V, the Faradaic efficiency for the production of FA decreases under strong competition from HER.

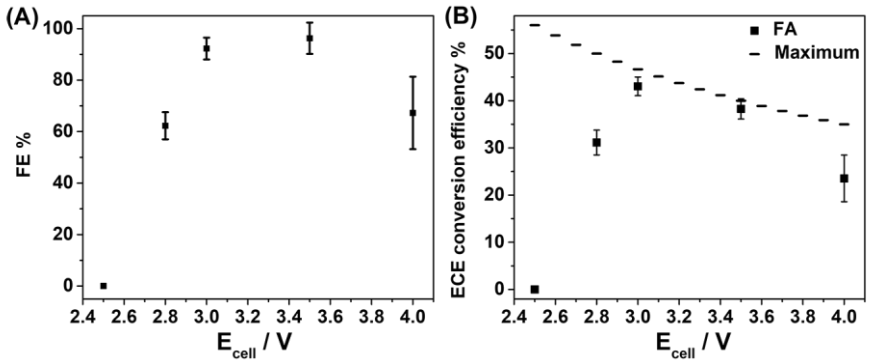

Figure 2.9 A) Faradaic efficiency and B) ECE conversion efficiency for FA as a function of the applied potential. The dashed line represents the theoretical maximum of the ECE conversion efficiency for CO_2 reduction. The error bars represent the standard deviation (n=3). Reproduced with permission from ref. [31]. Copyright 2021, The Royal Society of Chemistry.

Table 2.3 Faradaic efficiencies for all the products from CO_2 reduction in a two-electrode system at different E_{cell}.

Voltage (V)	H_2 (%)	CO (%)	Formic Acid (%)	Total (%)
2.5[a]	88.3	6.4	-	94.7
2.8	19.7±5.6	27.5±11.4	62.3±5.3	109.5±0.9
3.0	5.8[b]	2.8±2.7	92.3±4.2	97.0±4.9
3.5	0.8±0.3	1.1±0.7	96.3±6.1	98.2±5.4
4.0	26.7±16.7	18.5±6.4	67.2±14.1	112.4±3.9

[a] Of three experiments conducted at 2.5 V, the gas products were only collected once.

[b] Of three experiments conducted at 3 V, hydrogen was only found once.

The ECE conversion efficiencies for formic acid at various applied voltages can be calculated from the following:

$$\eta_{ECE} = \frac{\sum|E_i^0| \times FE_i}{E_{cell}} \qquad (2.4)$$

where E_i^0 is the electromotive force of the cell reaction (Table 2.1-2.2), FE is the Faradaic efficiency, E_{cell} is the total voltage applied to the electrolyzer, and the subscript i represents the i^{th} product from CO_2 reduction. From equation 2.4, the ECE conversion efficiency for eCO_2RR monotonically decreases with increasing E_{cell}. Moreover, it can be speculated that the theoretical maximum of the ECE conversion efficiency for eCO_2RR can be estimated using the most negative

value of E^0 (-1.3997 V for FA, Table 2.2) for the products of eCO_2RR (Figure 2.9 B).

Table 2.4 Energy conversion efficiencies for all the products from CO_2 reduction in a two-electrode system at different values of E_{cell}.

Voltage (V)	H_2 (%)	CO (%)	Formic acid (%)	Total (%)
2.5[a]	43.4	3.4	-	46.8
2.8	7.9±2.3	11.9±4.9	28.4±2.6	48.3±0.1
3.0	2.4[b]	1.2±1.2	42.9±2.1	44.9±2.0
3.5	0.3±0.1	0.4±0.3	38.1±1.9	38.7±1.6
4.0	7.4±4.9	5.5±1.7	20.9±3.9	33.7±0.6

[a] Of the three experiments conducted at 2.5 V, the gas products were only collected once.

[b] Of the three experiments conducted at 3 V, hydrogen was only found once.

The experimental data for which the total Faradaic efficiency exceeded 100% have been corrected with the corresponding Faradaic efficiency in calculating the energy conversion efficiency.

Accordingly, a relatively higher ECE conversion efficiency was obtained at 3.0 V (43%), compared to 3.5 V (38%). This improvement is attributed to the maintained Faradaic efficiency for the production of formic acid at over 90% (at 3.0 V) and to the reduced applied voltage. Moreover, if all products were taken into account, the total ECE conversion efficiency can reach 45% (Table 2.4).

2.3.2 Energy distribution in CO_2 electrolyzer

Since the electrical energy is only partially converted to chemical energy, we investigated the energy distribution of this electrochemical system. First, the voltage loss is the difference between E_{cell} and the sum of the potentials measured at the anode and cathode, i.e., equation 2.5 (Figure 2.7 and Table 2.5).

$$E_{loss} = E_{cell} - E_a + E_c \qquad (2.5)$$

We can observe that, as shown in Figure 2.10 A, when E_{cell} increases from 2.5 V to 4 V, the voltage loss of the system also increases from 0.076 V to 0.558 V. To define clearly the nature of the voltage loss, we further investigated the

relationship between the voltage loss and the reaction current (Figure 2.8), which results in a liner correlation (Figure 2.10 B).

Therefore, we can infer that the voltage loss is due to the uncompensated resistance, which includes that of the solution, the nafion membrane and the contact resistance, which has a value of about 130 Ω.

Table 2.5 Potentials applied at the anode and cathode, and the voltage loss at the applied E_{cell} (data from Figure 2.7). Potentials are referred to Ag/AgCl (KCl sat).

E_{cell} / V	E_a / V (vs. Ag/AgCl)	E_c / V (vs. Ag/AgCl)	E_a-E_c / V	Voltage loss / V	Voltage loss %
2.5	0.679±0.005	-1.745±0.003	2.424±0.006	0.076	3.04
2.8	0.711±0.006	-1.991±0.013	2.702±0.007	0.098	3.50
3.0	0.738±0.004	-2.105±0.005	2.843±0.008	0.157	5.23
3.5	0.938±0.017	-2.260±0.021	3.198±0.017	0.302	8.63
4.0	0.926±0.037	-2.516±0.055	3.442±0.019	0.558	13.95

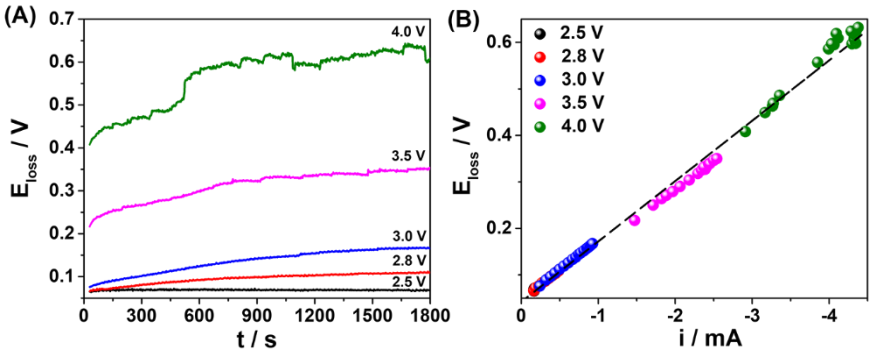

Figure 2.10 A) The voltage loss at various applied voltages during CO_2 reduction. B) Relationship between voltage loss and reaction current at various applied voltages. Reproduced with permission from ref. [31]. Copyright 2021, The Royal Society of Chemistry.

The last part of the energy loss is the overpotential at the electrodes (equation 2.6).[38]

$$E_{cell} = E^0 + E_{loss} + E_{overpotential} \qquad (2.6)$$

Owing to the tandem structure of this electrochemical system, the percentage energy distribution can be computed directly from the applied potential.

Therefore, in order to work out what the percentage energy loss due to the overpotential is, this was computed by excluding the ECE conversion efficiency for all the products and the uncompensated resistance from the total energy. Figure 2.11 shows the specific energy distribution in this electrolyzer. As the applied cell voltage in the system is increased, the total ECE conversion efficiency decreases from 48% to 34% (Table 2.4), and the energy loss caused by the uncompensated resistance increases from 3 to 14% (Table 2.5), whereas most of the energy in the system is consumed by the overpotential at the electrodes which is 50.64±1.85% at each applied voltage. Thus, reducing the uncompensated resistance and the overpotential of the electrodes is an effective way of reducing the energy loss, consequently improving the ECE conversion efficiency in this CO_2 electrolyzer.

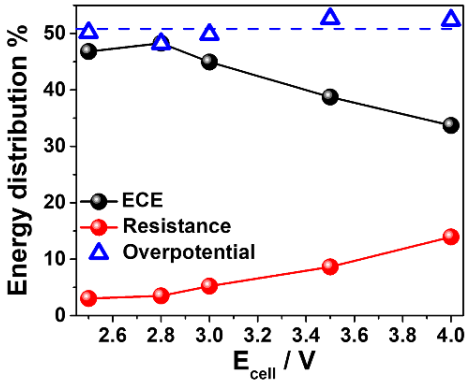

Figure 2.11 Percentage energy distribution in the CO_2 electrolyzer. The dashed line shows the average percentage energy distribution of the overpotential at the electrodes. Reproduced with permission from ref. [31]. Copyright 2021, The Royal Society of Chemistry.

To compare different anodes, we chose 1% BDD (doped with 1% boron) and Ni for experiments at 3.5 V (Table 2.6). In the case of 1% BBD, due to its high overpotential and low activity for the oxygen evolution reaction, both the voltage at the cathode and the reaction current are relatively low (Figure 1.12, 1.13). Note that the optimal potential range for CO_2 reduction using 0.1% BDD is from -2.1 V to -2.2 V (vs Ag/AgCl), and up to -2.5 V from our previous results.[28] However, in the system with a 1% BDD anode, this potential range is applied only in the first part of the electrolysis (~ 600 s) (Figure 1.12 A), which leads to a low Faradaic efficiency for the production of FA (Table 2.6). Even if the cathode voltage can be increased by applying a higher total cell voltage, this will inevitably result in a low ECE energy efficiency. On the other

hand, when Ni is the anode, in spite of its low overpotential for the oxygen evolution reaction, which allows a higher cathodic potential to be reached at the BDD electrode (-2.4 V vs. Ag/AgCl) (Figure 1.12), it tends to form oxygenates or hydroxides in an alkaline environment; consequently, the potential applied at the BDD cathode cannot be maintained at a stable working potential (Figure 1.12), resulting in poor product selectivity for formic acid (Table 2.6). Therefore, the anode should possess a low overpotential for water splitting and simultaneously should be able to remain stable during the entire CO_2 reduction process. Although, so far, in the present work, Pt has been shown to be the best anode material, replacement of the anode material and ohmic loss reduction are currently under investigation.

Table 2.6 Faradaic efficiencies for all products in a two-electrode system at 3.5 V with 0.1% BDD as the cathode coupled with different anodes.

Anode	H_2 (%)	CO (%)	Formic acid (%)	Total (%)
1% BDD[a]	11.7	42.8	45.27	99.77
Pt	0.8±0.3	1.1±0.72	96.26±6.08	98.16±5.35
Ni	20.93±2.2	19.73±9.4	68.09±9.39	108.76±1.05

[a] The experiment in the 1% BDD-0.1 % BDD system was only performed once

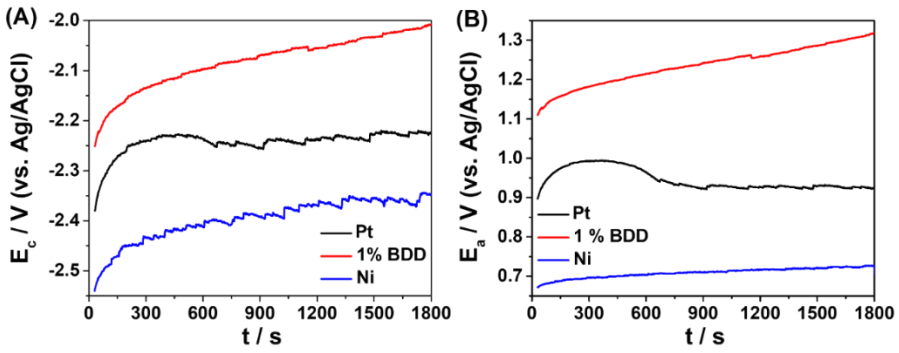

Figure 1.12 Comparison of different anodes showing A) potential on the cathode and B) potential on the anode during 30-min CO_2 reduction at 3.5 V in a two-electrode system. Potentials are referred to Ag/AgCl (KCl sat). Reproduced with permission from ref. [31]. Copyright 2021, The Royal Society of Chemistry.

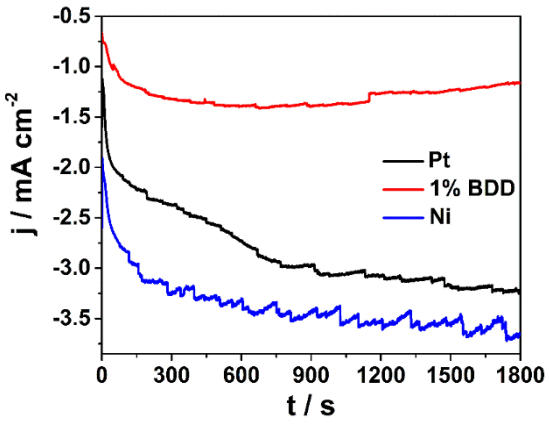

Figure 1.13 Comparison of current densities for different anodes during 30-min CO_2 reduction at 3.5 V in a two-electrode system. Reproduced with permission from ref. [31]. Copyright 2021, The Royal Society of Chemistry.

2.4 Conclusion

We investigated the electrochemical reduction of CO_2 using a BDD cathode in a two-electrode system. In aqueous solutions the main product from CO_2 reduction is formic acid, and the highest Faradaic efficiency, 96%, was achieved at a total applied voltage of 3.5 V. The electrical-to-chemical energy conversion efficiency for the production of formic acid can reach 43% at 3.0 V. Moreover, the total efficiency, including other products, at 3.0 V was 45% which is very close to the maximum theoretical efficiency for the electrochemical reduction of CO_2 at the corresponding voltage. We investigated the contribution of the energy losses involved in the electrical-to-chemical energy conversion efficiency, which is mainly ascribed to electrode overpotentials, and ways of decreasing this energy loss are currently under investigation. This electrolyzer using a BDD cathode has the potential to be used commercially in applications requiring the electrochemical reduction of CO_2.

2.5 References

(1) Aresta, M.; Dibenedetto, A.; Angelini, A. Catalysis for the Valorization of Exhaust Carbon: From CO_2 to Chemicals, Materials, and Fuels. Technological Use of CO_2. *Chem. Rev.* **2014**, *114* (3), 1709–1742.

(2) Nielsen, D. U.; Hu, X. M.; Daasbjerg, K.; Skrydstrup, T. Chemically and Electrochemically Catalysed Conversion of CO_2 to CO with Follow-up Utilization to Value-Added Chemicals. *Nat. Catal.* **2018**, *1* (4), 244–254.

(3) Kondratenko, E. V.; Mul, G.; Baltrusaitis, J.; Larraz ábal, G. O.; P érez-Ram írez, J. Status and Perspectives of CO_2 Conversion into Fuels and Chemicals by Catalytic, Photocatalytic and Electrocatalytic Processes. *Energy Environ. Sci.* **2013**, *6* (11), 3112–3135.

(4) Singh, A. K.; Singh, S.; Kumar, A. Hydrogen Energy Future with Formic Acid: A Renewable Chemical Hydrogen Storage System. *Catal. Sci. Technol.* **2016**, *6* (1), 12–40.

(5) Yu, X.; Pickup, P. G. Recent Advances in Direct Formic Acid Fuel Cells (DFAFC). *J. Power Sources* **2008**, *182* (1), 124–132.

(6) He, J.; Jan áky, C. Recent Advances in Solar-Driven Carbon Dioxide Conversion: Expectations versus Reality. *ACS Energy Lett.* **2020**, *5* (6), 1996–2014.

(7) Hori, Y. *Electrochemical CO_2 Reduction on Metal Electrodes*; Springer: New York, 2008; pp 89-189.

(8) Verma, S.; Kim, B.; Jhong, H. R. M.; Ma, S.; Kenis, P. J. A. A Gross-Margin Model for Defining Technoeconomic Benchmarks in the Electroreduction of CO_2. *ChemSusChem* **2016**, *9* (15), 1972–1979.

(9) Rosen, B. A.; Salehi-Khojin, A.; Thorson, M. R.; Zhu, W.; Whipple, D. T.; Kenis, P. J. A.; Masel, R. I. Ionic Liquid-Mediated Selective Conversion of CO_2 to CO at Low Overpotentials. *Science* **2011**, *334* (6056), 643–644.

(10) Vermaas, D. A.; Smith, W. A. Synergistic Electrochemical CO_2 Reduction and Water Oxidation with a Bipolar Membrane. *ACS Energy Lett.* **2016**, *1* (6), 1143–1148.

(11) Zhou, X.; Liu, R.; Sun, K.; Chen, Y.; Verlage, E.; Francis, S. A.; Lewis, N. S.; Xiang, C. Solar-Driven Reduction of 1 atm of CO_2 to Formate at 10% Energy-Conversion Efficiency by Use of a TiO_2-Protected III-V Tandem Photoanode in Conjunction with a Bipolar Membrane and a Pd/C Cathode. *ACS Energy Lett.* **2016,** 1, 764-770.

(12) Schreier, M.; Curvat, L.; Giordano, F.; Steier, L.; Abate, A.; Zakeeruddin, S. M.; Luo, J.; Mayer, M. T.; Grätzel, M. Efficient Photosynthesis of Carbon Monoxide from CO_2 Using Perovskite Photovoltaics. *Nat. Commun.* **2015**, *6*, 7326.

(13) Cheng, Y.; Hou, P.; Pan, H.; Shi, H.; Kang, P. Selective Electrocatalytic Reduction of Carbon Dioxide to Oxalate by Lead Tin Oxides with Low Overpotential. *Appl. Catal. B Environ.* **2020**, *272* (April), 118954.

(14) Anawati; Frankel, G. S.; Agarwal, A.; Sridhar, N. Degradation and Deactivation of Sn Catalyst Used for CO_2 Reduction as Function of Overpotential. *Electrochim. Acta* **2014**, *133*, 188–196.

(15) Russell, P. G.; Kovac, N.; Srinivasan, S.; Steinberg, M. The Electrochemical Reduction of Carbon Dioxide, Formic Acid, and Formaldehyde. *J. Electrochem. Soc.* **1977**, *124* (9), 1329–1338.

(16) Narayanan, S. R.; Haines, B.; Soler, J.; Valdez, T. I. Electrochemical Conversion of Carbon Dioxide to Formate in Alkaline Polymer Electrolyte Membrane Cells. *J. Electrochem. Soc.* **2011**, *158* (2), A167.

(17) Bushuyev, O. S.; De Luna, P.; Dinh, C. T.; Tao, L.; Saur, G.; van de Lagemaat, J.; Kelley, S. O.; Sargent, E. H. What Should We Make with CO_2 and How Can We Make It? *Joule* **2018**, *2* (5), 825–832.

(18) Kuhl, K. P.; Cave, E. R.; Abram, D. N.; Jaramillo, T. F. New Insights into the Electrochemical Reduction of Carbon Dioxide on Metallic Copper Surfaces. *Energy Environ. Sci.* **2012**, *5* (5), 7050–7059.

(19) Nitopi, S.; Bertheussen, E.; Scott, S. B.; Liu, X.; Engstfeld, A. K.; Horch, S.; Seger, B.; Stephens, I. E. L.; Chan, K.; Hahn, C.; Nørskov, J. K.; Jaramillo, T. F.; Chorkendorff, I. Progress and Perspectives of Electrochemical CO_2 Reduction on Copper in Aqueous Electrolyte. *Chem. Rev.* **2019**, *119* (12), 7610–7672.

(20) Valenti, G.; Melchionna, M.; Montini, T.; Boni, A.; Nasi, L.; Fonda, E.; Criado, A.; Zitolo, A.; Voci, S.; Bertoni, G.; Bonchio, M.; Fornasiero, P.; Paolucci, F.; Prato, M. Water-Mediated ElectroHydrogenation of CO_2 at Near-Equilibrium Potential by Carbon Nanotubes/Cerium Dioxide Nanohybrids. *ACS Appl. Energy Mater.* **2020**, *3* (9), 8509–8518.

(21) Melchionna, M.; Bracamonte, M. V.; Giuliani, A.; Nasi, L.; Montini, T.; Tavagnacco, C.; Bonchio, M.; Fornasiero, P.; Prato, M. Pd@TiO_2/Carbon Nanohorn Electrocatalysts: Reversible CO_2 Hydrogenation to Formic Acid. *Energy Environ. Sci.* **2018**, *11* (6), 1571–1580.

(22) O'Mara, P. B.; Wilde, P.; Benedetti, T. M.; Andronescu, C.; Cheong, S.; Gooding, J. J.; Tilley, R. D.; Schuhmann, W. Cascade Reactions in Nanozymes: Spatially Separated Active Sites inside Ag-Core-Porous-Cu-Shell Nanoparticles for Multistep Carbon Dioxide Reduction to Higher Organic Molecules. *J. Am. Chem. Soc.* **2019**, *141* (36), 14093–14097.

(23) Nakata, K.; Ozaki, T.; Terashima, C.; Fujishima, A.; Einaga, Y. High-Yield Electrochemical Production of Formaldehyde from CO_2 and Seawater. *Angew. Chemie - Int. Ed.* **2014**, *53* (3), 871–874.

(24) Birdja, Y. Y.; Koper, M. T. M. The Importance of Cannizzaro-Type Reactions during Electrocatalytic Reduction of Carbon Dioxide. *J. Am. Chem. Soc.* **2017**, *139* (5), 2030–2034.

(25) Ikemiya, N.; Natsui, K.; Nakata, K.; Einaga, Y. Long-Term Continuous Conversion of CO_2 to Formic Acid Using Boron-Doped Diamond Electrodes. *ACS Sustain. Chem. Eng.* **2018**, *6* (7), 8108–8112.

(26) Kashiwada, T.; Watanabe, T.; Ootani, Y.; Tateyama, Y.; Einaga, Y. A Study on Electrolytic Corrosion of Boron-Doped Diamond Electrodes When Decomposing Organic Compounds. *ACS Appl. Mater. Interfaces* **2016**, *8* (42), 28299–28305.

(27) Natsui, K.; Iwakawa, H.; Ikemiya, N.; Nakata, K.; Einaga, Y. Stable and Highly Efficient Electrochemical Production of Formic Acid from Carbon Dioxide Using Diamond Electrodes. *Angew. Chemie - Int. Ed.* **2018**, *57* (10), 2639–2643.

(28) Tomisaki, M.; Kasahara, S.; Natsui, K.; Ikemiya, N.; Einaga, Y. Switchable Product Selectivity in the Electrochemical Reduction of Carbon Dioxide Using Boron-Doped Diamond Electrodes. *J. Am. Chem. Soc.* **2019**, *141* (18), 7414–7420.

(29) Gurudayal; Bullock, J.; Srankó, D. F.; Towle, C. M.; Lum, Y.; Hettick, M.; Scott, M. C.; Javey, A.; Ager, J. Efficient Solar-Driven Electrochemical CO_2 Reduction to Hydrocarbons and Oxygenates. *Energy Environ. Sci.* **2017**, *10* (10), 2222–2230.

(30) Whipple, D. T.; Kenis, P. J. A. Prospects of CO_2 Utilization via Direct Heterogeneous Electrochemical Reduction. *J. Phys. Chem. Lett.* **2010**, *1* (24), 3451–3458.

(31) Du, J.; Fiorani, A.; Einaga, Y. An Efficient, Formic Acid Selective CO_2 electrolyzer with a Boron-Doped Diamond Cathode. *Sustain. Energy Fuels* **2021**, *5* (10), 2590–2594.

(32) Xu, J.; Natsui, K.; Naoi, S.; Nakata, K.; Einaga, Y. Effect of Doping Level on the Electrochemical Reduction of CO_2 on Boron-Doped Diamond Electrodes. *Diam. Relat. Mater.* **2018**, *86* (March), 167–172.

(33) Xu, J.; Yokota, Y.; Wong, R. A.; Kim, Y.; Einaga, Y. Unusual Electrochemical Properties of Low-Doped Boron-Doped Diamond Electrodes Containing Sp^2 Carbon. *J. Am. Chem. Soc.* **2020**, *142* (5), 2310–2316.

(34) Hori, Y.; Wakebe, H. H. I.; Tsukamoto, T.; Koga, O. Electrocatalytic Process of CO Selectivity in Electrochemical Reduction of CO_2 at Metal Elctrodes in Aqueous Media. *Electrochim. Acta* **1994**, *39* (11–12), 1833–1839.

(35) White, J. L.; Baruch, M. F.; Pander, J. E.; Hu, Y.; Fortmeyer, I. C.; Park, J. E.; Zhang, T.; Liao, K.; Gu, J.; Yan, Y.; Shaw, T. W.; Abelev, E.; Bocarsly, A. B. Light-Driven Heterogeneous Reduction of Carbon Dioxide: Photocatalysts and Photoelectrodes. *Chem. Rev.* **2015**, *115* (23), 12888–12935.

(36) Einaga, Y. Diamond Electrodes for Electrochemical Analysis. *J. Appl. Electrochem.* **2010**, *40* (10), 1807–1816.

(37) Macpherson, J. V. A Practical Guide to Using Boron Doped Diamond in Electrochemical Research. *Phys. Chem. Chem. Phys.* **2015**, *17* (5), 2935–2949.

(38) Tufa, R. A.; Chanda, D.; Ma, M.; Aili, D.; Demissie, T. B.; Vaes, J.; Li, Q.; Liu, S.; Pant, D. Towards Highly Efficient Electrochemical CO_2 Reduction: Cell Designs, Membranes and Electrocatalysts. *Appl. Energy* **2020**, *277* (May), 115557.

Chapter 3

A New Pathway for CO_2 Reduction Relying on the Self-Activation Mechanism of Boron-Doped Diamond Cathode

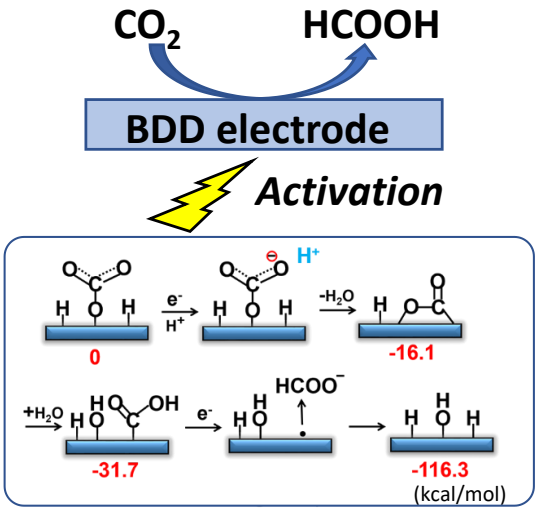

Enhanced electrochemical CO_2 reduction

Reproduced with permission from Du, J.; Fiorani, A.; Inagaki, T.; Otake, A.; Murata, M.; Hatanaka, M.; Einaga, Y. A New Pathway for CO_2 Reduction Relying on the Self-Activation Mechanism of Boron-Doped Diamond Cathode. *JACS Au* **2022**, *2*, 1375-1382. Copyright 2022, American Chemical Society.

3.1 Introduction

Research on carbon dioxide (CO_2) utilization is one of the keystone to realize the artificial carbon cycle and possibly carbon neutrality.[1,2] Several methods are currently under investigation,[3,4] and among them the electrochemical CO_2 reduction reaction (eCO_2RR) has been proved to be a viable and efficient approach to reduce CO_2 into small useful molecule compounds like CO,[5] formic acid or short chain hydrocarbons and oxygenates.[6–8] In these products, as a liquid fuel, formic acid not only possesses superiorities in transportation and storage but also has a bright application prospect in hydrogen vector[9] and fuel cells.[10] However, high overpotentials, poor product selectivity and low current densities are still obstacles that hinder the technological applications of eCO_2RR.[11]

During eCO_2RR the main reason concerning overpotentials and poor product selectivity was found to be the energetically unfavorable CO_2 adsorption.[12] Specific interactions between the CO_2 molecule (i.e., substrate) and electrodes (i.e., electrocatalyst) are needed to stabilize reaction intermediates, leading to lower overpotentials, high product selectivity and faster reaction rate. Until now, the most recognized pathway for eCO_2RR is through the generation of CO_2 radical anion ($CO_2^{\bullet-}$).[13] If the generation of $CO_2^{\bullet-}$ is the rate determining step, this will introduce a large overpotential as $CO_2/CO_2^{\bullet-}$ redox couple has a standard potential that lies near −1.85 V vs SHE which limits the electrolysis potential in a highly negative range.[13–17]

Kanan's group reported that compared to pure metal, oxidized or oxide-derived metal electrodes showed more prominent Faradaic efficiency and reduced overpotential for eCO_2RR,[18,19] where the increased stabilization of $CO_2^{\bullet-}$ intermediate was speculated to be the reason of this improved performance. But unfortunately, the chemical model and direct evidence of the interaction between CO_2 molecules and the oxygen-terminations are still unclear. In this context, the surface state of the electrode is crucial to provide stabilization for intermediate species in reaction mechanisms which did not rely on the generation of $CO_2^{\bullet-}$. A possible pathway has been proposed by Baruch et al. as the mechanism involved bicarbonate functional groups and an unlikely simultaneous transfer of two electrons.[20] Valenti et al. proposed CeO_2 as an electrocatalyst for CO_2 hydrogenation at overpotential as low as −0.02 V.[21] From the previous examples, it is clear that oxides or oxygenated species plays a central role in eCO_2RR at low overpotentials. Therefore, the specific mechanism for eCO_2RR, especially when the

applied potential is insufficient to form $CO_2^{\bullet-}$ radicals, is still worth further investigation.

Boron-doped diamond (BDD) was proposed as an outstanding candidate for mechanistic investigation of eCO_2RR. BDD is chosen for its long term stability,[22] resistance to corrosion[23] and high product selectivity[24,25] in eCO_2RR. In addition, due to its unique properties of low capacitive current and wide potential window,[26] BDD not only could greatly inhibit the reactivity of hydrogen evolution, which is the main competitor of eCO_2RR, and also is able to show evident redox signals for the electrochemical analysis. However, so far, the mechanism for the initial eCO_2RR reaction process has not been clearly determined. Therefore, in order to apply eCO_2RR to industrial processes, we now urgently need clarification and optimization of the factors that determine the experimental conditions, including the pretreatment of BDD electrode surfaces.

Here, we investigated a process referred as "self-activation" of BDD that prompted us to suggest a new and efficient pathway for eCO_2RR, which bypasses the mechanism involving $CO_2^{\bullet-}$. During electrolysis, the CO_2 molecules were first bound by BDD in the form of unidentate carbonate (-O-CO_2) and were further transformed to carboxylic structure (-COOH) after a proton and electron transfer reaction. This process leaves a detectable amount of carboxylic groups on the surface of BDD which are dependent on time, current density and potential, for this reason named self-activation, finally enhancing the performance in terms of Faradaic efficiency and partial current density. The application of this self-activation mechanism was evaluated on the performance of eCO_2RR with a long-term two-electrode electrolysis reaching a remarkable electrical-to-chemical energy (ECE) conversion efficiency of 50.2% after 7-hour self-activation at the total cell voltage of 2.7 V for eCO_2RR to formic acid.[27]

3.2 Experimental section

3.2.1 Materials

KCl, KOH, H_2SO_4, $NaClO_4$ and 2-propanol were purchased from Wako Pure Chemical Industries Ltd. $NiSO_4$, $FeSO_4$ and $(NH_4)_2SO_4$ were purchased from Sigma Aldrich. All reagents were used without any further purification. The deionized (DI) water employed in this work was from a Simply-Lab water system (DIRECT-Q 3 UV, Millipore) with a resistivity of 18.2 MΩ·cm at 25 °C. Experiments were performed at

room temperature (25 °C) in atmospheric pressure, unless stated otherwise. All of the electrochemical measurements were performed with the assistance of a potentiostat/galvanostat system (PGSTAT204, Metrohm Autolab). Ag/AgCl, KCl (sat'd) was set as the reference electrode for all of the electrochemical measurements in this work.

3.2.2 Preparation of BDD electrode

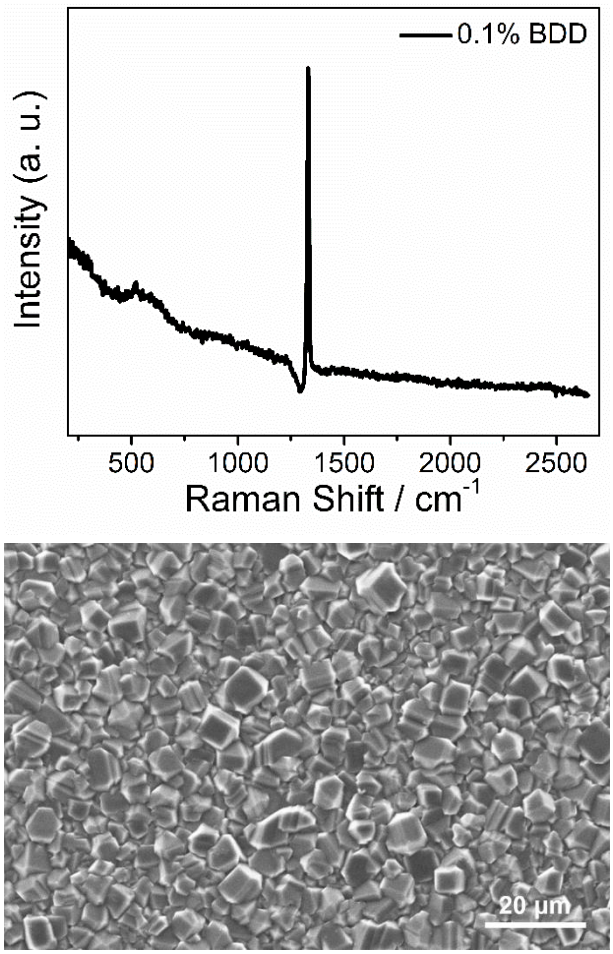

Figure 3.1 (Top) Raman spectrum for the BDD electrode and (bottom) SEM micrograph of BDD with a boron content of 0.1% deposited onto Si (100) substrate. Reproduced with permission from ref. [27]. Copyright 2022, American Chemical Society.

The polycrystalline BDD film was deposited on a Si (100) wafer substrate with a microwave plasma-assisted chemical vapor deposition (MPCVD) system (AX6500, Cornes Technologies Ltd.). The concentration of boron in the BDD electrode was determined by the ratio between the carbon source (methane) and the boron source (trimethylboron) and was set to 0.1%.[28] A glow discharge optical emission spectroscopy

(GDOES, GD-Profiler2, Horiba Ltd.) measurement was performed to further confirm the exact content of boron in BDD. Raman spectrum was recorded using an Acton SP2500 (Princeton Instruments) with a 532 nm laser (Figure 3.1) to confirm the crystallinity of diamond and exclude the interference caused by sp^2 carbon.[29] Surface morphology images of the BDD film were obtained with a scanning electron microscope (JCM-6000, JEOL) (Figure 3.1). As shown in SEM micrograph, the Si substrate was fully covered by the crystal grains of BDD and no pinholes can be found on the BDD surface. The interference of the substrate, Si (100) was excluded by corresponding eCO_2RR (Figure 3.2, Table 3.1).

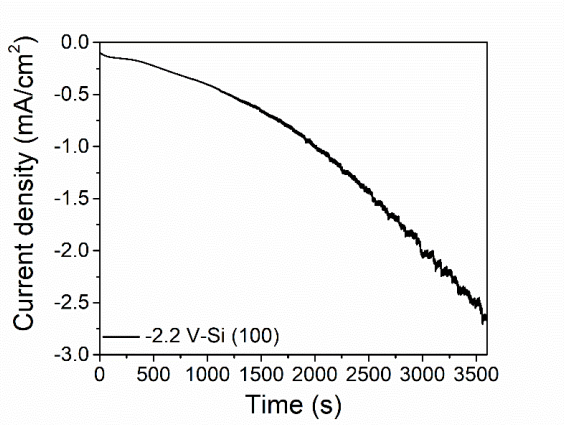

Figure 3.2 The variation of current densities during CO_2 reduction by Si (100) at -2.2 V vs Ag/AgCl. Reproduced with permission from ref. [27]. Copyright 2022, American Chemical Society.

Table 3.1 Faradaic efficiencies for all products in CO_2 reduction with Si (100) at -2.2 V vs Ag/AgCl.

	HCOOH	H_2	CO
Si (100)	20.57 %	69.7 %	0.7 %

To further exclude the interference of Si (100), we performed the eCO_2RR with Si (100). The corresponding current density and Faradaic efficiency were shown in Figure 3.2 and Table 3.1, respectively. We can observe that in the CO_2 reduction with Si (100) the Faradaic efficiency for hydrogen evolution is around 70% and the Faradaic efficiency for formic acid production is only 20%. The product selectivity of the Si (100) for CO_2 reduction is much worse than that of BDD (over 90% for formic acid). And the current density during electrolysis is also different with the performance of BDD in the CO_2 reduction (Figure 3.5). Therefore, the interference of the substrate (Si (100)) can be excluded in this work.

3.2.3 Electrochemical measurements and product analysis

Before each electrolysis, the BDD electrode was cleaned with 2-propanol and DI water by an ultrasonic treatment for 10 minutes each. Electrochemical measurements were performed in a two-compartment polytetrafluoroethylene (PTFE) flow cell which was with the same condition of our previous work.[24] 0.1 % BDD, Pt and Ag/AgCl (KCl sat'd) were set as the cathode, anode and reference electrode respectively and the two chambers of the cell were separated by Nafion NRE-212 (Sigma Aldrich). As a pretreatment before CO_2 reduction, several cyclic voltammetry (CV) scans (including 10 cycles from a potential of -3.5 V to 3.5 V in 0.1 M H_2SO_4 and 20 cycles from 0 V to 3.5 V 0.1 M $NaClO_4$ with a scan rate of 0.5 V/s) were performed to assure reproducibility and cleanliness of the surface of the electrodes. The catholyte and anolyte were 0.5 M KCl and 1 M KOH, respectively (50 mL each). The catholyte was bubbled with N_2 for 30 min to remove oxygen and CO_2 for 60 min resulting in a CO_2-sauturated solution. During electrolysis, CO_2 bubbling was set at a flow rate of 10 ml min^{-1}.

For the two-electrode electrolysis system, the nafion membrane was replaced by the bipolar membrane (fumasep® FBM, FUELCELL Store). Each chamber in the cell was connected with a reference electrode (Ag/AgCl, KCl sat'd) to monitor the working potentials of both cathode and anode. In comparison experiments, the Pt anode was further replaced by Ni (Nilaco), NiFeOx and dimensional stable electrode (DSE, DE NORA). The NiFeOx electrode was synthesized through electrodeposition. In brief, a Ni foil was immersed in a mixture solution of 9 mM $NiSO_4$, 9 mM $FeSO_4$ and 25 mM $(NH_4)_2SO_4$ (pH adjusted at 2.5 by H_2SO_4) and was electrolyzed under a constant current of 10 mA/cm^2 for 30 s and repeated for 50 cycles.

At the end of each CO_2 reduction experiment, all of the products were quantified. Formic acid was quantified by high-performance liquid chromatography (HPLC, CDD-10A, Shimadzu Corp.). The gaseous products (CO and H_2) were collected in an aluminum gas bag (GL Sciences) and quantified by gas chromatography (GC-2014, Shimadzu Corp.). Formic acid for HPLC calibration was obtained from FUJIFILM Wako pure Chemical Corporation. Hydrogen and carbon monoxide for GC calibration were obtained from GL Sciences.

3.2.4 XPS measurements

The specific elemental information about the surface of BDD electrode was measured with an X-ray photoelectron spectrometer (XPS, JPS-9010 TR, JEOL). The C 1s spectra were deconvoluted with Gaussian functions. Peaks deconvoluted from the C 1s spectra were assigned to the following components: 283.0 eV (sp^2 C-C bond), 284.1 eV (C-H bond), 284.75 eV (sp^3 C-C bond), 285.3 eV (C-O bond) and 286.2 eV (C=O bond). These binding energies were fixed for all of the XPS analyses.

3.2.5 In Situ Attenuated total reflectance infrared spectroscopy measurements

A thin 0.1% BDD film was deposited on a Si ATR-IR prism using MPCVD with the same method as mentioned before. The quality of the BDD film was verified by Raman spectrum (Figure 3.3). A one chamber PTFE cell was used to perform the electrolysis in which BDD, glassy carbon rod and Ag/AgCl (KCl sat'd) were set as the working electrode, counter electrode and reference electrode, respectively. Supporting electrolytes as 0.1 M H_2SO_4 and 0.1 M $NaClO_4$ were used for the pretreatment, while 0.5 M KCl for CO_2RR. The ATR-IR spectra were measured through a FT/IR-6600 (JASCO Corp.) with a liquid-nitrogen-cooled mercury-cadmium-telluride detector. All of the spectra were collected at a resolution of 4 cm^{-1} and had 256 scans. The baseline spectrum and pretreated comparison spectrum were measured in N_2-saturated DI water. After the electrolysis, the BDD electrode was washed by DI water for three times and then the ATR-IR spectrum was measured again in N_2-saturated DI water.

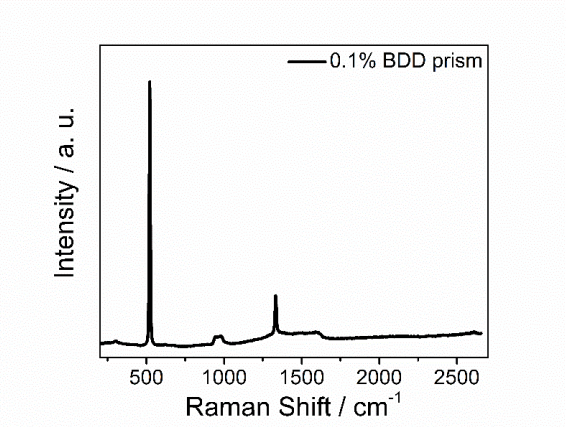

Figure 3.3 Raman spectrum for the BDD prism with a boron content of 0.1%. Reproduced with permission from ref. [27]. Copyright 2022, American Chemical Society.

3.2.6 Modification with aminoferrocene and characterization

The BDD electrode was activated by incubation with 10 mM 1-(3-dimethylaminopropyl)-3-ethylcarbodiimide hydrochloride (EDC, Tokyo Chemical Industry Co. Ltd), 10 mM N-hydroxysuccinimide (NHS, Sigma-aldrich) and 0.1 M 2-Morpholinoethanesulfonic acid (MES, DOJINDO) for 1 h in DI water. After rinsed with 0.1 M MES, the BDD electrode was further incubated with 0.01 M aminoferrocene (Fc-NH_2, Sigma-aldrich) in 0.1 M carbonate buffer solution (pH 9.8) for 1 h. Fc-NH_2 was previously dissolved in the minimum amount of acetonitrile. Before electrochemical measurements, BDD was rinsed with the mixed solvent DI water and acetonitrile 50:50 v/v. Cyclic voltammetry (CV) scan rate was set to 50 mV s^{-1} and potential range was from -0.2 V to 0.6 V. Square wave voltammetry (SWV) measurements were performed with the scan rate of 50 mV s^{-1} in the potential range of 0.1~0.6 V. All measurements were performed in a one chamber PTFE cell with 0.5 M KCl as supporting electrolyte.

3.3 Results and discussion

3.3.1 Self-activation process of BDD

To investigate and verify the self-activation process of BDD, we first performed the eCO_2RR with a BDD cathode in a three-electrode system in a flow cell. As shown in Figure 3.4 A and B, 3-hours eCO_2RR experiments were carried out at the potential of −2 V.

Galvanostatic CO_2 reductions for 1 hour at current densities of −0.1 mA cm^{-2}, −0.5 mA cm^{-2}, −1 mA cm^{-2}, −1.5 mA cm^{-2} and −2 mA cm^{-2} were adopted as activation processes and performed before the formal eCO_2RR. Without activation, current density and Faradaic efficiency at BDD are −0.17 mA cm^{-2} and 73.81%, respectively. In contrast, by the activation processes the current density reached −0.22 mA cm^{-2}, −0.3 mA cm^{-2}, −0.59 mA cm^{-2}, −0.23 mA cm^{-2} and −0.35 mA cm^{-2}, and the Faradaic efficiency for formic acid achieved 81.29%, 88.65%, 91.01%, 87.51% and 87.32%, respectively. An activation current of −1 mA cm^{-2} resulted in the best conditions as the current density was improved more than three times and the Faradaic efficiency increased by 17.2% compared to BDD without activation.

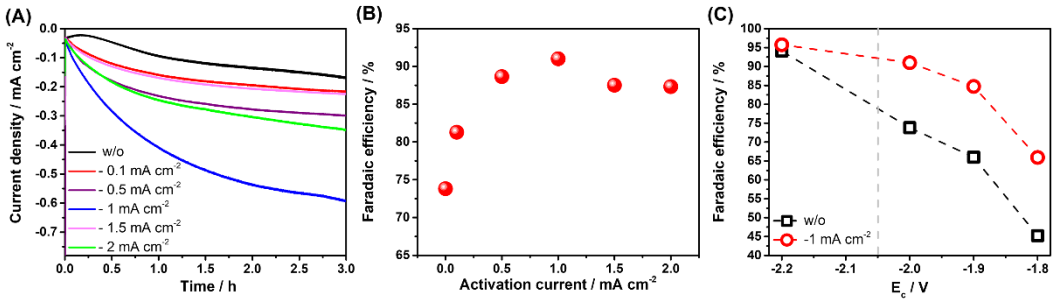

Figure 3.4 (A) Current densities and (B) Faradaic efficiencies in 3-hours eCO_2RR at −2 V showing the difference between the activated and non-activated BDD electrode. Activation processes were performed with 1-hour galvanostatic CO_2 reduction at the current densities of −0.1 mA cm^{-2}, -0.5 mA cm^{-2}, −1 mA cm^{-2}, -1.5 mA cm^{-2} and −2 mA cm^{-2} respectively before the formal eCO_2RR. (C) Compared Faradaic efficiencies of the activated (-1 mA cm^{-2}, red) and non-activated (w/o, black) BDD electrode at different electrolysis potentials (Ec). Reference electrode: Ag/AgCl, KCl (sat'd). The gray dotted line represents the standard potential of $CO_2/CO_2^{\bullet-}$: $E^0 = -2.05$ V vs Ag/AgCl, KCl (sat'd). Reproduced with permission from ref. [27]. Copyright 2022, American Chemical Society.

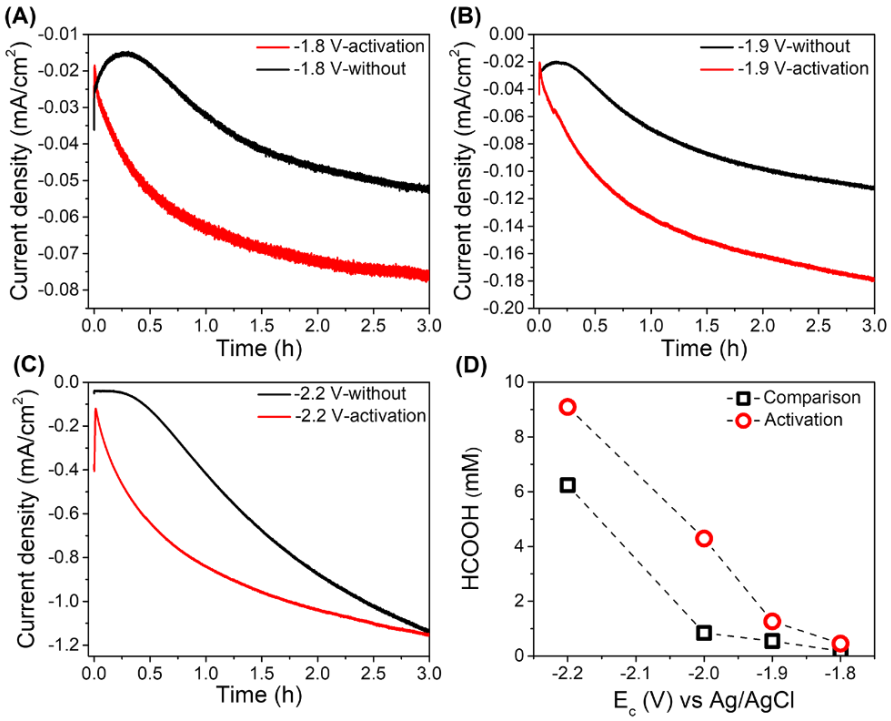

Figure 3.5 Compared current densities showing the difference between activated and non-activated BDD electrode at (A) -1.8 V, (B) -1.9 V and (C) -2.2 V. (D) Compared product concentration (HCOOH) of the activated (-1 mA cm^{-2}, red) and non-activated (black) BDD electrode at different electrolysis potentials (Ec). The reaction time is 3 hours and the volume of the electrolyte is 50 ml. Reference electrode: Ag/AgCl, KCl (sat'd). Reproduced with permission from ref. [27]. Copyright 2022, American Chemical Society.

To confirm the benefit of activation, electrolysis experiments of eCO_2RR were performed at different potentials from −2.2 V to −1.8 V, where the activation current density was set as −1 mA cm^{-2}. According to Figure 3.4 C an improvement of the Faradaic efficiency took place in the region of low potentials, also associated to higher current densities and product concentration (Figure 3.5) indicating that the reaction current of the activated BDD was significantly improved. When the reduction potential was −2.2 V, the Faradaic efficiencies of the activated and non-activated BDD were at the same level, while at reaction potential of −2 V, −1.9 V and −1.8 V, the Faradaic efficiencies of the activated BDD increase of 17.2%, 18.72% and 20.7%, respectively, compared with those by non-activated BDD.

Previously, we proposed that the generation of $CO_2^{\bullet-}$ intermediate (E^0 = −2.05 V vs Ag/AgCl, KCl(sat'd)) is a reliable pathway for BDD cathode to achieve efficient eCO_2RR.[24,25] Without activation process, a Faradaic efficiency higher than 80% could be realized only when the applied potential is sufficiently negative to generate the $CO_2^{\bullet-}$. However, the results in Figure 3.4 proved that with the aid of the activation process the performance of eCO_2RR was greatly improved for more positive potentials (~100-150 mV) and a Faradaic efficiency of more than 80% could be obtained even at potentials where the $CO_2^{\bullet-}$ was hardly produced. Besides, it is worth noting that in the eCO_2RR with BDD cathode, the faradic current keep increasing with time, a tendency observed previously.[30] Therefore, we speculate that during eCO_2RR, BDD will be subjected to a self-activation process that increase the electroactive area available for CO_2 reduction, and other reaction intermediates than $CO_2^{\bullet-}$ might be generated on the surface which will gradually increase along with the reaction time.

3.3.2 Mechanistic investigation

A combination of X-ray photoelectron spectrometer (XPS), in-situ attenuated total reflectance infrared (ATR-IR) spectroscopy and electrochemical measurements have been used to investigate the changes of BDD surface state before and after the activation process by eCO_2RR.

The comparison of XPS spectra for C 1s signal were depicted in Figure 3.6 and fitted to account for five carbon species including sp^2 C-C, C−H, sp^3 C−C, C−O and C=O.[31] The deconvolution of the C 1s signal revealed that with the activation by eCO_2RR, the content of C−H bonds decreased, while the amount of oxygen-containing groups increased, where the increment of C−O bond was 5% and the content of C=O group

increased to 12.6%. From this increment of oxygen moieties, we presumed that during eCO_2RR the CO_2 molecules were first bound on BDD in the form of chemisorption and then reacted into oxygen-containing intermediates. The relative abundance of these components is summarized in Table 3.2.

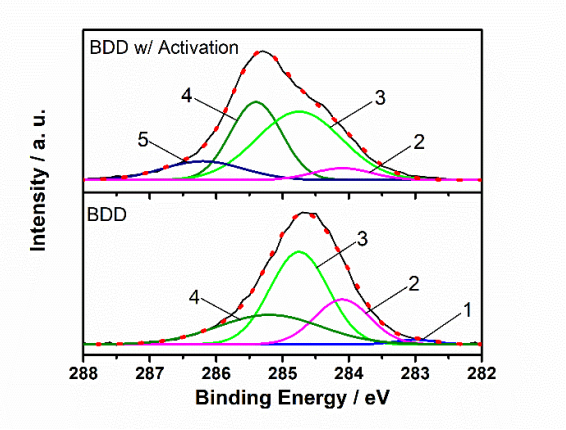

Figure 3.6 Deconvoluted C 1s spectra for the BDD and BDD with activation electrodes. The components are shown as follows: (1) sp^2 C-C, (2) C−H, (3) sp^3 C−C, (4) C−O, and (5) C=O. Reproduced with permission from ref. [27]. Copyright 2022, American Chemical Society.

Table 3.2 Relative abundance of the components (%) on the surface of BDD electrode.

	sp^2 C-C	C−H	sp^3 C−C	C−O	C=O
BDD	1.5	22.3	48.8	27.4	-
BDD w/ activation	-	5.8	48.2	33.4	12.6

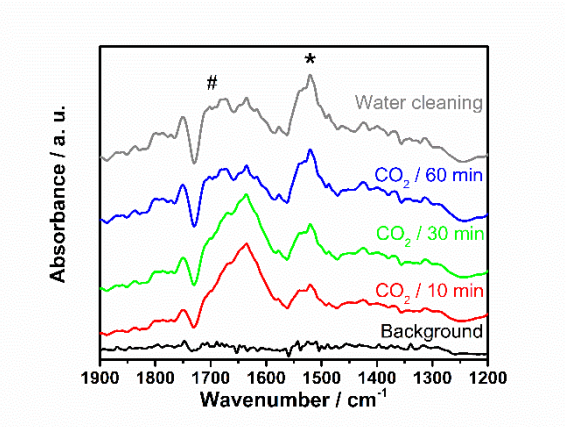

Figure 3.7 In situ time-dependent ATR-IR spectra during CO_2 reduction at -2 V vs Ag/AgCl, KCl (sat'd). The gray line shows the ATR-IR spectrum after rinsing BDD in ultra-pure water. * and # indicate the υ_4 vibration of unidentate carbonate and the stretching vibration of carboxylic c=o group, respectively. Reproduced with permission from ref. [27]. Copyright 2022, American Chemical Society.

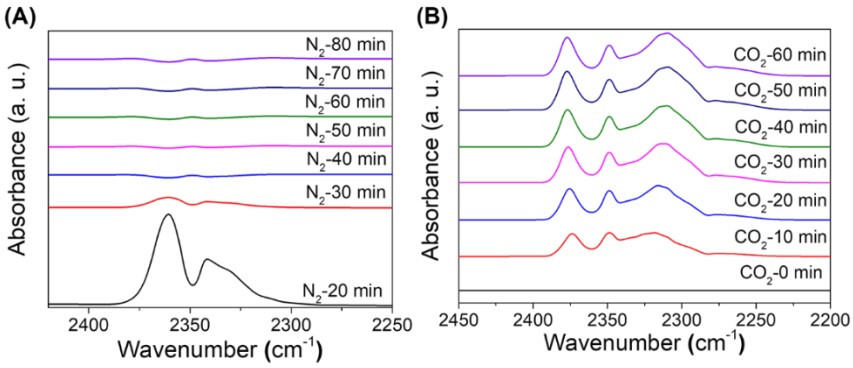

Figure 3.8 In situ time-dependent ATR-IR spectra showing the intensity variation of CO_2 vibration during (A) N_2 bubbling (B) CO_2 bubbling. Reproduced with permission from ref. [27]. Copyright 2022, American Chemical Society.

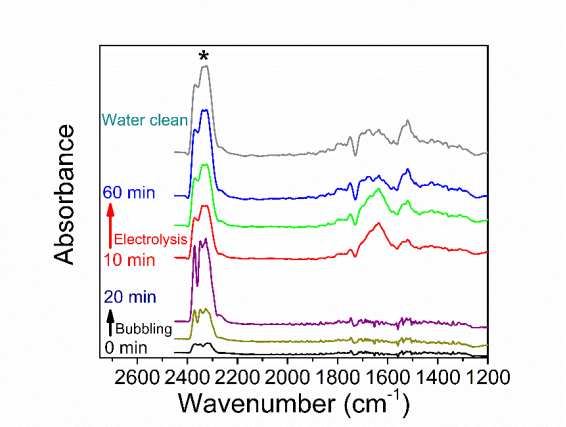

Figure 3.9 In situ time-dependent ATR-IR spectra in the range of 1200 cm^{-1}~2500 cm^{-1} at -2 V vs Ag/AgCl (KCl sat'd). The dark yellow line represents IR spectrum after 10 min-CO_2 bubbling. The green one represents the IR spectrum after 30 min-electrolysis. * indicates the vibration of CO_2 molecules. Reproduced with permission from ref. [27]. Copyright 2022, American Chemical Society

To confirm the XPS results and verify the existence of such oxygen-containing intermediates, in-situ ATR-IR spectroscopy measurements were further carried out (Figure 3.7). Before eCO_2RR, the background ATR-IR spectrum did not show any feature, even during CO_2 bubbling, meaning that signals of CO_2 chemisorption could not be observed (Figure 3.8-3.9). During eCO_2RR, new absorption peaks emerged in the region 1900 cm^{-1}-1200 cm^{-1} (Figure 3.7). The strong absorption at 1530-1470 cm^{-1} and 1370-1300 cm^{-1} was assigned to the vibration of unidentate carbonate (–O–CO_2),[32] and showed an increasing trend with time of eCO_2RR. Because the intense absorption peaks at 1650 cm^{-1} and 3400-3200 cm^{-1} showed a similar time-dependence variation

(Figure 3.7 and Figure 3.10), both have been assigned to water vibration modes.[20] Conversely to water vibrations, the shoulder peak at 1720-1710 cm^{-1} kept increasing during the eCO_2RR. Therefore, we suggested that the shoulder peak at 1720-1710 cm^{-1} and peak at 1460-1370 cm^{-1} could be assigned to the characteristic absorption of C=O and –OH groups in carboxylic structure (–COOH) respectively,[33] moreover this signal cannot be mistaken for formic acid in solution (Figure 3.11). Even after rinsing the BDD in ultra-pure water, the characteristic peaks of unidentate carbonate and carboxylic structure on the surface could be observed clearly (Figure 3.7). In addition, the presence of the carboxylic structure on BDD after eCO_2RR was further verified by reaction with aminoferrocene (Fc-NH_2, Figure 3.12)[34,35] and detected electrochemically (Figure 3.13).

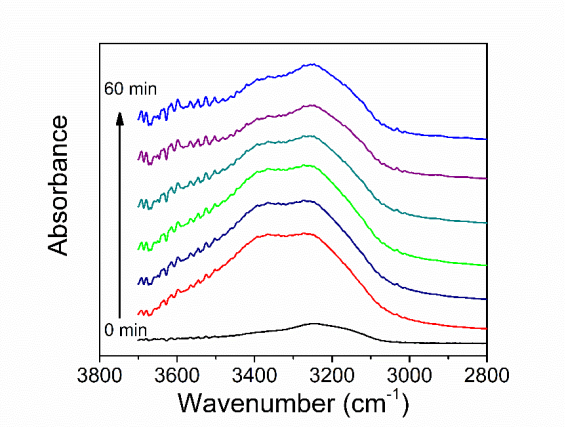

Figure 3.10 In situ time-dependent ATR-IR spectra showing the intensity variation of water vibration during the electrochemical CO_2 reduction at -2 V vs Ag/AgCl. Reproduced with permission from ref. [27]. Copyright 2022, American Chemical Society.

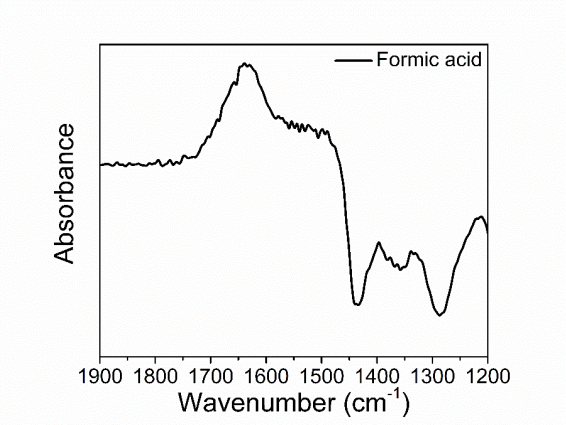

Figure 3.11 The characteristic infrared spectrum of 8 mM formic acid in 0.1 M KCl. Reproduced with permission from ref. [27]. Copyright 2022, American Chemical Society.

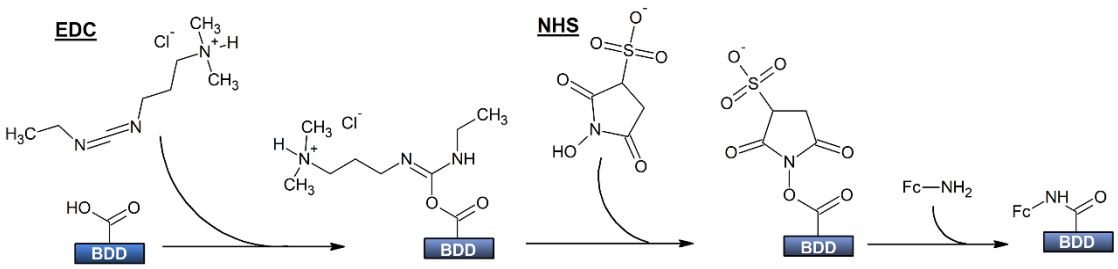

Figure 3.12 The schematic diagram showing the modification process of Fc-NH_2. Reproduced with permission from ref. [27]. Copyright 2022, American Chemical Society.

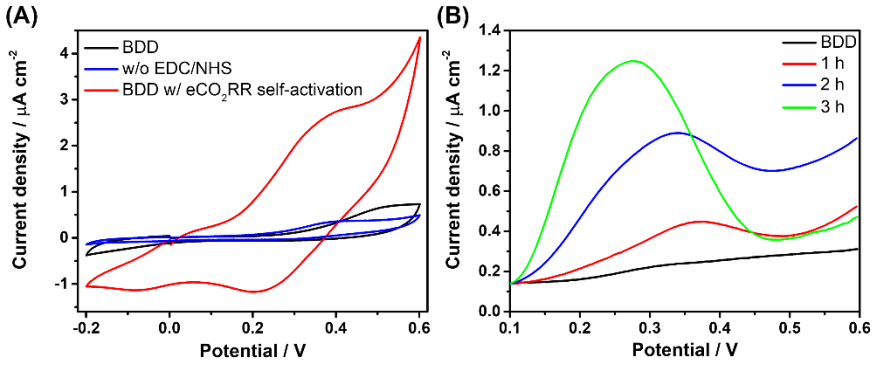

Figure 3.13 (A) CVs of BDD electrodes after the modification with Fc-NH_2: comparison sample without CO_2 reduction (black), CO_2 reduction-activated BDD without the addition of EDC/NHS before the Fc-NH_2 functionalization (blue) and CO_2 reduction-activated BDD coupled with the addition of EDC/NHS before the Fc-NH_2 functionalization (red); BDD activation by galvanostatic eCO_2RR at -1 mA cm^{-2}. (B) SWVs showing the variation of the Fc-NH_2 signals along with the time of eCO_2RR. Scan rate: 50 mV s^{-1}, supporting electrolyte: 0.5 M KCl, reference electrode: Ag/AgCl, KCl (sat'd). Reproduced with permission from ref. [27]. Copyright 2022, American Chemical Society.

The schematic diagram showing the modification process of Fc-NH_2 was described in Figure 3.12. With the help of 1-(3-dimethylaminopropyl)-3-ethylcarbodiimide hydrochloride (EDC) and N-hydroxysuccinimide (NHS), the carboxylic structure on the surface of BDD can be activated to react with the amino group of Fc-NH_2 and consequently the redox process of Fc-NH_2 can be monitored by cyclic voltammetry. A clear redox signal, corresponding to ferrocene, was observed for BDD electrode after eCO_2RR, but not for the comparison BDD (Figure 3.13 A) thus confirming that carboxylic functionalities were available on the surface of BDD only after eCO_2RR. Considering that aldehyde groups can react with Fc-NH_2 as well, and without activation

by EDC/NHS, we performed the Fc-NH_2 functionalization without EDC/NHS. Because the CV did not show any redox peak, we could exclude the presence of aldehydes on BDD surface after eCO_2RR (Figure 3.13 A). Therefore, the formation of carboxylic functionalities could be demonstrated through ATR-IR spectra and redox signals from the functionalization with Fc-NH_2. Furthermore, to evaluate the time dependence on the formation of carboxylic groups, we measured the ferrocene redox signal at increasing time of eCO_2RR (Figure 3.13 B). The current increment for the redox peak of ferrocene demonstrates that the amount of carboxylic functionality intermediates generated on the surface of BDD electrode increased gradually with the time of eCO_2RR.

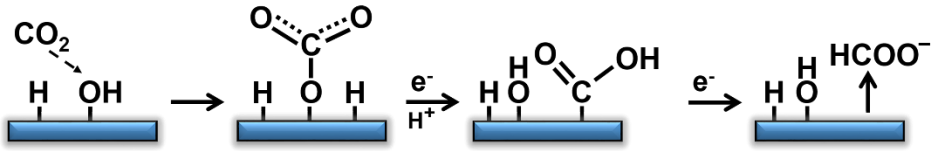

Figure 3.14 Schematic diagram showing the alternative mechanism of electrochemical CO_2 reduction on BDD at low overpotentials. Reproduced with permission from ref. [27]. Copyright 2022, American Chemical Society.

On the basis of the measurements described previously, we demonstrated that during eCO_2RR unidentate carbonate and carboxylic structure were generated on the surface of BDD. The amount of both intermediates increased with the time of electrolysis, and these two groups could remain on the surface of BDD even after the CO_2 reduction. Therefore, we concluded that CO_2 molecules would be bound on the surface of BDD in the form of unidentate carbonate first, then underwent a proton-coupled electron transfer (PCET) reaction[36] at negative potentials to generate carboxylic groups, and finally released from the surface of BDD as formate. During electrolysis, the increase of unidentate carbonate and carboxylic intermediates on the surface of BDD brings the direct consequence of enhancing the Faradaic efficiency of CO_2 reduction because activation will not only improve the reaction current, but also to enhance the competitiveness of eCO_2RR for protons, which is an essential reactant for both hydrogen evolution and eCO_2RR. The supposed schematic diagram of this pathway is shown in Figure 3.14 and Figure 3.15.

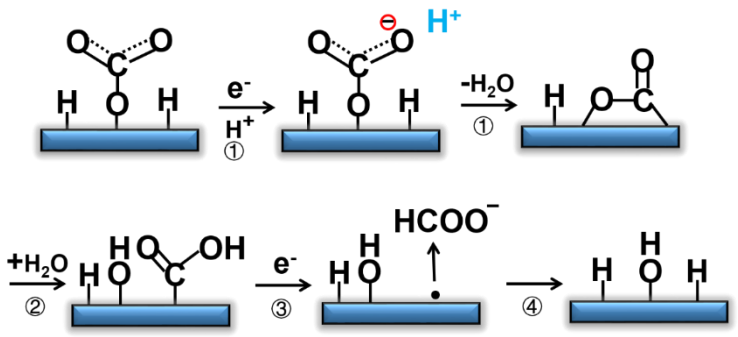

Figure 3.15 Schematic diagram showing the mechanism of electrochemical CO_2 reduction on BDD from unidentate carbonate to the generation of formate. The step (1) represents the proton-coupled electron transfer reaction under negative potentials, step (2) represents the hydrolysis of lactone, step (3) represents the electron transfer from electrode to carboxylic structure and step (4) represents the recovery of hydrogen termination. Reproduced with permission from ref. [27]. Copyright 2022, American Chemical Society.

In support for the reaction mechanism beyond the experimental evidences, we performed first-principles calculations based on density functional theory. The BLYP functional[37,38] was used to calculate the electronic structures of the surface of interest. The effects of electrolyte solution and electrode potential on the electronic structures were taken into account by using the reference interaction site model[39] and the effective screening medium method,[40] respectively. The surface state with unidentate carbonate was calculated as a stationary point where the negative charge of −0.75 *e* resides on the surface under the experimental electrode potential condition of ca. −2.0 V vs Ag/AgCl (Figure 3.16 A). This starting point has been set at 0 kcal/mol. Concerning the other intermediate, the carboxylic surface state was calculated to be nearly electrically neutral with a neighboring hydroxyl group (Figure 3.16 C). This carboxylic intermediate was found to be more stable by ca. 31 kcal/mol in grand potential than the unidentate carbonate surface state. This result indicates that the reaction proceeds through the unidentate carbonate intermediate followed by the carboxylic structure. The final hydroxyl terminated surface was estimated to be more stable by ca. 85 kcal/mol in grand potential than the carboxylic surface state, which was due to the release of the energy storage compound, i.e., formic acid (Figure 3.16 D). Noteworthy, all these defined reaction steps as reported in Figure 3.14 proceed exothermically. In conclusion, the calculation results are consistent with the experimental observations, and in agreement with the reaction pathway that has been proposed where unidentate carbonate and carboxylic groups are available on the BDD surface. Further insights are available in

the Appendix (Figure A1 and Table A1).

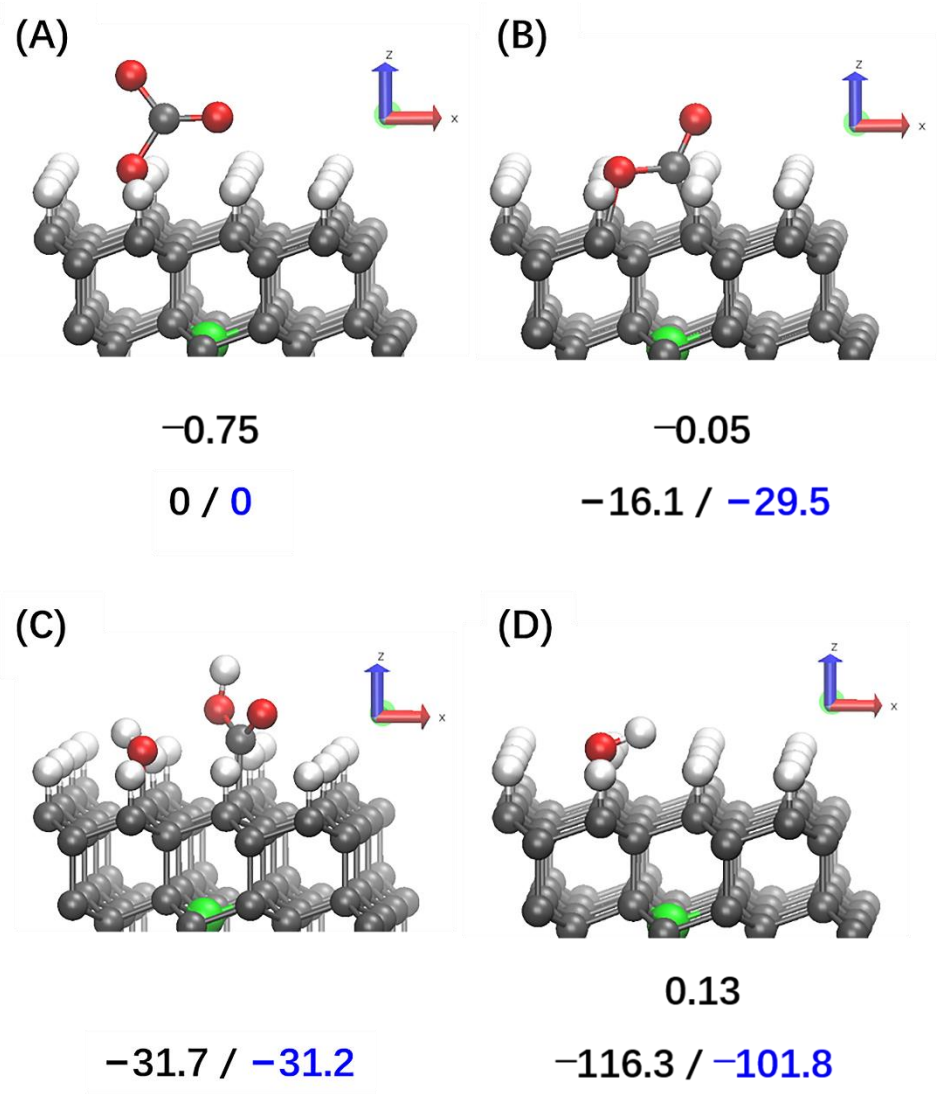

Figure 3.16 Four surface states with (A) unidentate carbonate, (B) lactone, (C) carboxylic, and (D) hydroxyl moieties. Values in the upper line are charges (in unit of *e*) introduced in the system to keep the electrode potential to be -2.0 V vs Ag/AgCl. Left black-colored (right blue-colored) values in the lower line are the grand potential (grand potential plus translational and rotational entropic contributions of molecules released into the solution) (in unit of kcal/mol) relative to that in the surface state with unidentate carbonate. Gray, white, red, and green spheres represent carbon, hydrogen, oxygen, and boron atoms, respectively. Reproduced with permission from ref. [27]. Copyright 2022, American Chemical Society.

The possible reaction pathway from unidentate carbonate to carboxylic structure was explored on the basis of ATR-IR spectra and the theoretical calculations. During CO_2 reduction at -2 V (vs Ag/AgCl), weak signals were emerged at 1800 cm^{-1}-1736 cm^{-1} (Figure 3.7), which can be ascribed to the vibrations of lactone. Considering that

lactones can be converted to carboxylic structure under hydrolysis, we suggested that it is possible for lactones to be intermediates in the reaction step from unidentate carbonate to carboxylic structure.

With the assistance of theoretical calculation, we estimated the grand potentials of unidentate carbonate, lactone and carboxylic structure at negative potentials (-2 V vs Ag/AgCl) and found that if the surface state with unidentate carbonate was set as the starting point (0 kcal/mol), the grand potentials of these three kinds of intermediates were in stepwise decline which were 0 kcal/mol, -16.1 kcal/mol and -31.7 kcal/mol, respectively (Figure 3.16). This decline of grand potentials indicates the potential of lactone as reaction intermediates in electrochemical CO_2 reduction. Therefore, we proposed the reaction pathway as shown in Figure 3.15 and expected it could provide novel insights for exploring the mechanism of electrochemical CO_2 reduction.

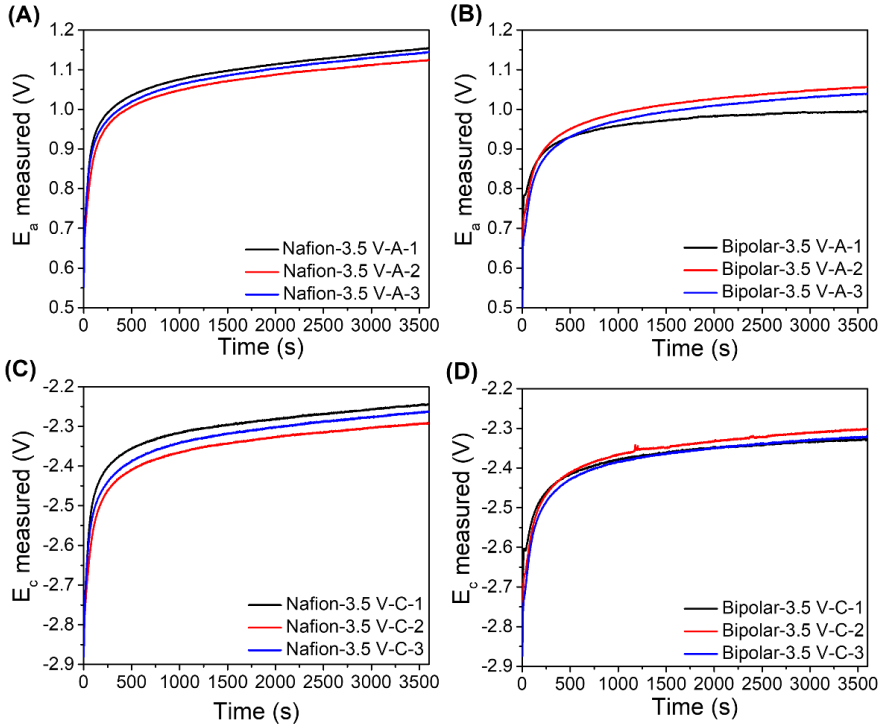

Figure 3.17 The comparison of the potentials on the Pt (anode) and BDD (cathode) during 1-hour CO_2 reduction at the applied voltage of 3.5 V showing the difference between nafion (A and C) and bipolar membrane (B and D). E_a signifies the potential applied to the anode and E_c represents the potential applied to the cathode. Potentials are referred to Ag/AgCl (KCl sat). Reproduced with permission from ref. [27]. Copyright 2022, American Chemical Society.

3.3.3 Long-term self-activation

To evaluate the time-dependence of the self-activation process on BDD and the overall effect on Faradaic and energy efficiency, the eCO_2RR was tested in an electrolysis system. The electrochemical cell comprised two compartments, equipped with a flow electrolyte setup, where BDD was set as the cathode. The electrochemical flow cell was first optimized by testing the performance for different membranes, which separate the anode and cathode chambers (i.e., Nafion and bipolar membrane), and for electrolyte flow rate. As a result, bipolar membrane was selected to ensure that both sides would not be contaminated by cation crossover, in particular by metal ions from the anode electrode[41,42] (Figure 3.17-3.20), while 400 ml/min was selected as the optimal flow rate of electrolyte (Figure 3.21 and Table 3.3-3.4).

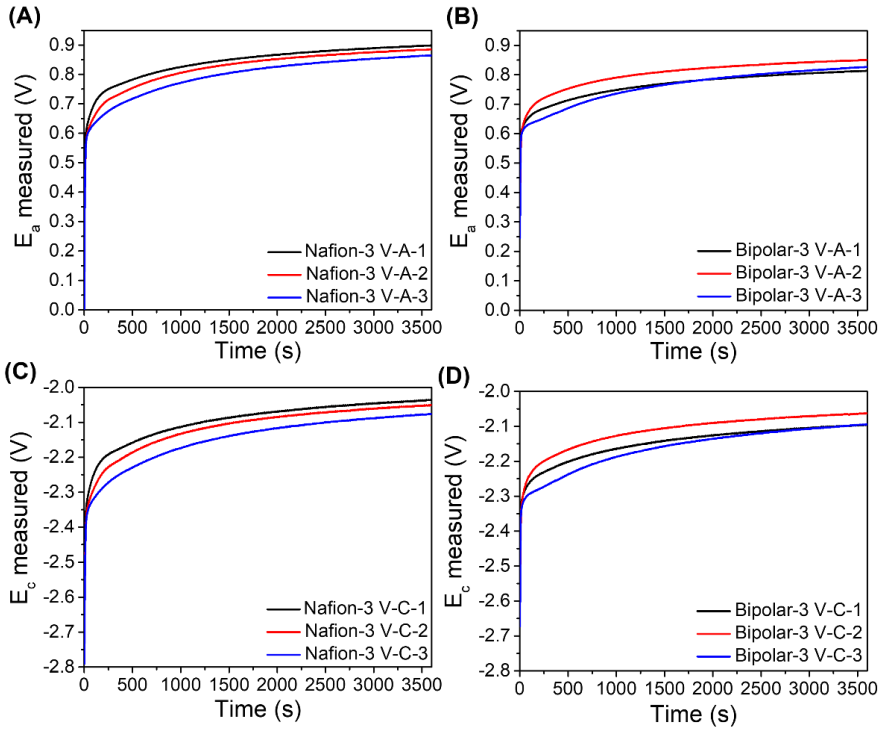

Figure 3.18 The comparison of the potentials on the Pt (anode) and BDD (cathode) during 1-hour CO_2 reduction at the applied voltage of 3.0 V showing the difference between nafion (A and C) and bipolar membrane (B and D). E_a signifies the potential applied to the anode and E_c represents the potential applied to the cathode. Potentials are referred to Ag/AgCl (KCl sat). Reproduced with permission from ref. [27]. Copyright 2022, American Chemical Society.

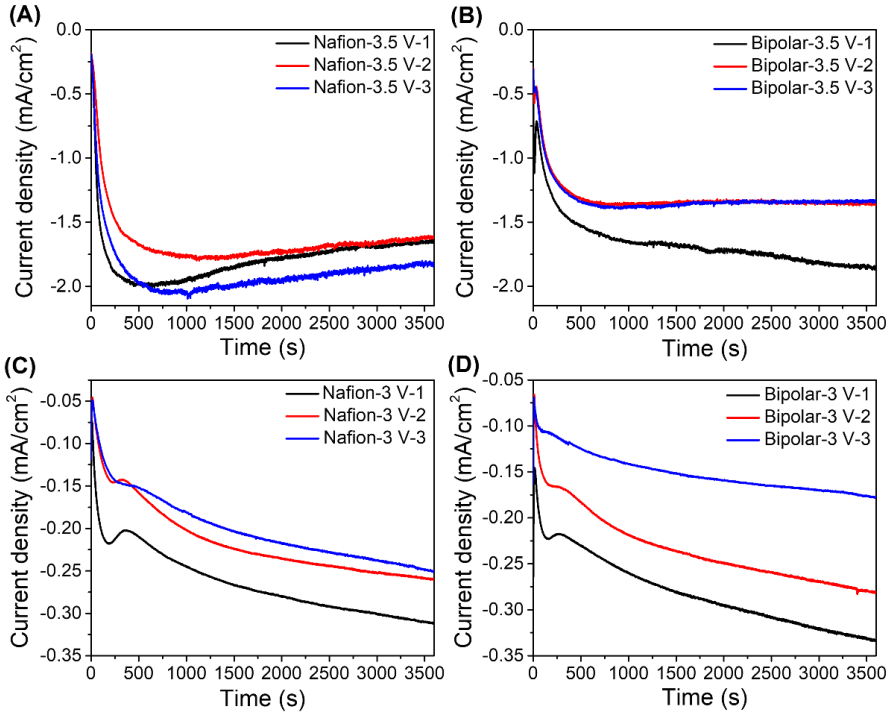

Figure 3.19 The comparison of the current densities in the BDD-based CO_2 electrolyzer during 1-hour CO_2 reduction at 3 V and 3.5 V showing the difference between nafion (A and C) and bipolar membrane (B and D). Potentials are referred to Ag/AgCl (KCl sat). Reproduced with permission from ref. [27]. Copyright 2022, American Chemical Society.

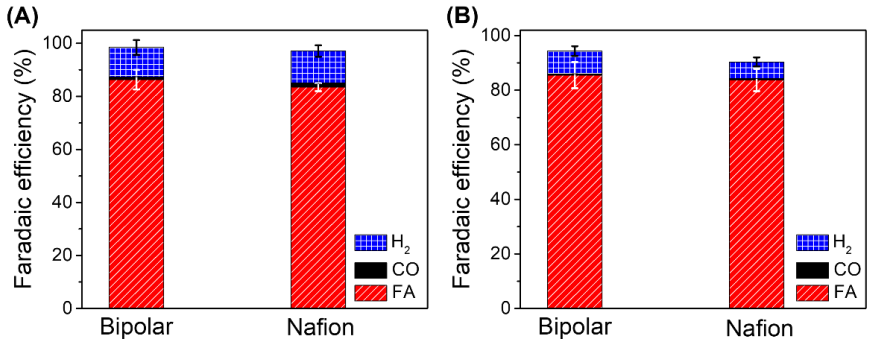

Figure 3.20 Compared Faradaic efficiencies of various products including CO, H_2 and formic acid in the bipolar menbrane and nafion electrolyzers for CO_2 reduction at (A) -3.5 V and (B) -3.0 V. Reproduced with permission from ref. [27]. Copyright 2022, American Chemical Society.

Nafion was known as a common cation exchange membrane and bipolar membrane was proved to efficiently separate the ions in catholyte and anolyte. According to the result in Figure 3.17-3.20, in terms of electrode potential, reaction current and Faradaic efficiency, both of nafion and bipolar membrane showed the same level of

electrochemical performance for CO_2 reduction. Therefore, in order to obtain a pure and safe reaction environment, we chose bipolar membrane for the long-term electrolysis experiments.

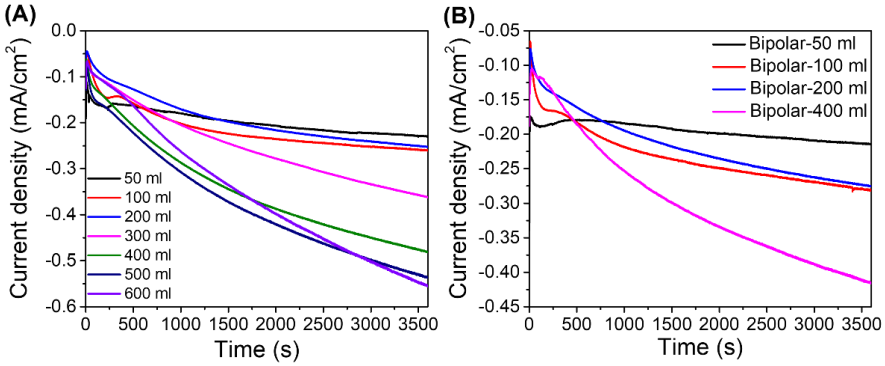

Figure 3.21 Current densities of the BDD-based CO_2 electrolyzer separated by (A) nafion and (B) bipolar membrane with different flow rates of electrolyte. The CO_2 reductions were performed at -3 V. Reproduced with permission from ref. [27]. Copyright 2022, American Chemical Society.

The optimization results of the flow rate show that the reaction current can be effectively improved when the flow rate is above 400 ml/min (Figure 3.21). And the Faradaic efficiency at different flow rates indicates that the Faradaic efficiency of carbon dioxide reduction will decrease when the flow rate is higher than 400 ml/min (Table 3.3 and 3.4). Therefore, 400 ml/min was considered as the best reaction flow rate.

Table 3.3 Faradaic efficiencies for all products in electrochemical CO_2 reduction at -3 V with nafion as the membrane. The volume of the electrolyte is 50 ml and the electrolysis was performed for 1 hour.

Flow rate (ml/min)	**H_2 (%)**	**CO (%)**	**Formic Acid (%)**	**Concentration of formic acid (mM)**
50	9.9	0.3	77.37	0.55
100	4.9	0.5	86.08	0.67
200	8.6	0.8	83.68	0.58
300	8.9	0.7	86.93	0.79
400	7.6	1	87.2	1.08
500	9.1	0.8	85.94	1.17
600	9.8	0.9	78.96	1.00

Table 3.4 Faradaic efficiencies for all products in bipolar membrane-separated CO_2 electrolyzer at -3 V. The volume of the electrolyte is 50 ml and the electrolysis was performed for 1 hour.

Flow rate (ml/min)	H_2 (%)	CO (%)	Formic Acid (%)	Concentration of formic acid (mM)
50	16.8	0.7	65.34	0.46
100	6.9	0.6	88.81	0.74
200	7.7	1.2	83.05	0.65
400	11.7	1.1	81	0.87

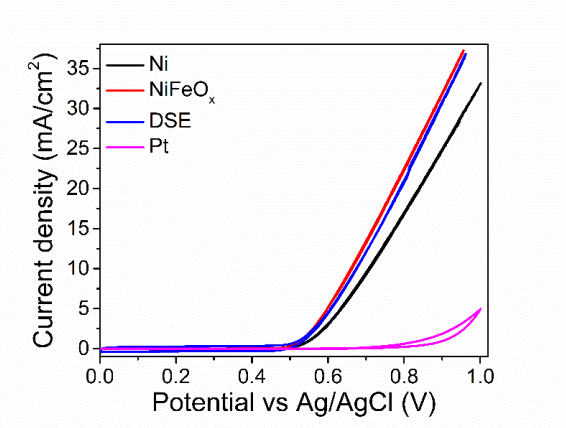

Figure 3.22 Cyclic voltammetry curves of the efficient oxygen-evolution anodes including Ni, NiFeOx and dimensional stable electrode (DSE). Pt was set as the comparison electrode. Potentials are referred to Ag/AgCl (KCl sat). Reproduced with permission from ref. [27]. Copyright 2022, American Chemical Society.

Furthermore, we investigated the performance of four selected anodes such as Pt, Ni, NiFeOx and dimensional stable electrode (DSE, Ti/IrOx,Ta_2O_5) to ensure an efficient oxygen evolution reaction (OER).[43] This aspect is crucial because the anode material, completing the electrochemical cell, will affect both the potential distribution between anode and cathode and the current density achievable. The CVs and XPS spectra of anode electrodes are shown in Figure 3.22 and 3.23, respectively. We performed the eCO_2RR with the BDD-cathode electrolyzer at different total voltages to find the most suitable potential that maximize Faradaic efficiency and electrical-to-chemical energy (ECE) conversion efficiency. During this investigation, we observed that both efficiencies are positively correlated with improved OER according to the anode materials. In particular, at 2.7 V the ECE conversion efficiency reached 48%, while the Faradaic efficiency is stable between 85 and 95% (Figure 3.24 and Table 3.5-3.6). The

improvement of the ECE conversion efficiency was mainly attributed to the low energy consumption attained by using efficient OER anodes (Figure 3.25-3.26 and Table 3.7-3.8). The repeatability of the activation process was further verified in two electrode eCO_2RR (Figure 3.27-3.28).

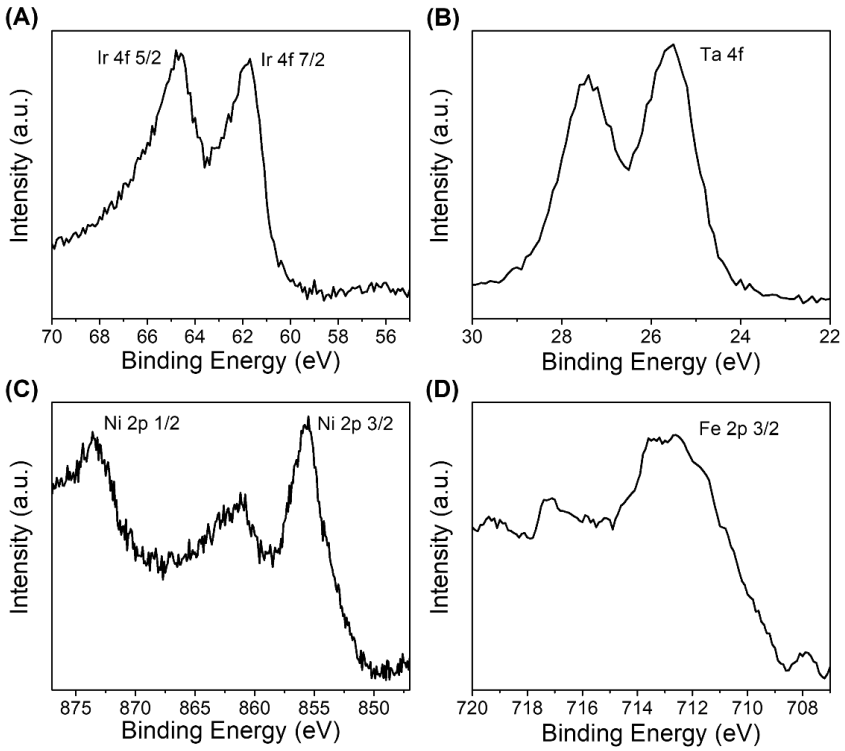

Figure 3.23 The X-ray photoelectron spectrometer spectra of the DSE (A and B) and NiFeOx (C and D) indicating that the ingredient of the DSE is the mixture of IrO_x and TaO_x. Reproduced with permission from ref. [27]. Copyright 2022, American Chemical Society.

The XPS result demonstrates that the NiFeOx electrode is synthesized successfully. And the elemental information of the dimensional stable electrode reveals that the main components are TaO_x and IrO_x.

Faradaic efficiency and electrical-to-chemical energy (ECE) conversion efficiency

The Faradaic efficiency (FE) can be defined by the following equation:

$$FE = \frac{\sum n_i \times F \times n^{\circ} mol_i}{Q} \qquad (3.1)$$

where n is the number of electrons involved in the reduction, n° mol is the number of moles of product, Q is the total charge in the electrolysis and F is the Faraday constant.

The ECE conversion efficiency (η_{energy}) can be evaluated using the equation below:

$$\eta_{energy} = \frac{\sum|E_i^o|\times FE_i}{E_{cell}} \qquad (3.2)$$

where E_{cell} represents the total cell voltage applied in the electrolysis and E^o represents the standard electromotive force of the cell reaction. The subscript i represents the i_{th} product from CO_2 reduction. Under normal conditions, the E^o of formic acid, hydrogen and carbon monoxide can be identified as -1.3997 V, -1.229 V and -1.333 V respectively.

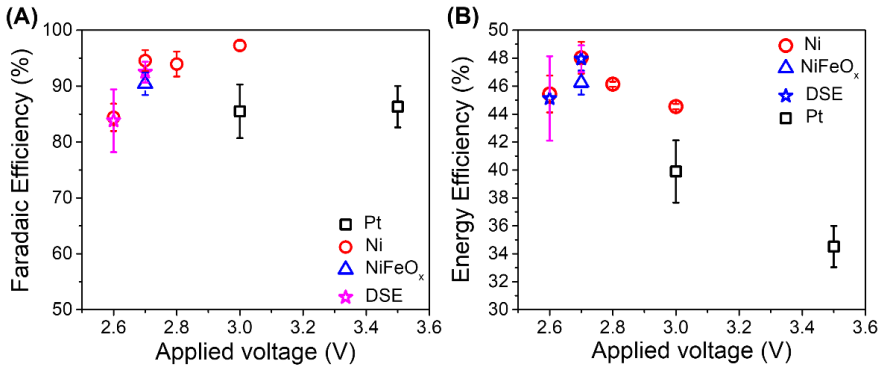

Figure 3.24 The (A) Faradaic efficiency and (B) electrical-to-chemical energy conversion efficiency of BDD-based CO_2 electrolyzer coupled with different anodes for the single product of formic acid including Pt (black), Ni (red), NiFeOx (blue) and dimensional stable electrode (pink). Reproduced with permission from ref. [27]. Copyright 2022, American Chemical Society.

Table 3.5 Faradaic efficiencies for all the products from CO_2 reduction in a two-electrode system with various anodes at different E_{cell}.

Condition	H_2 (%)	CO (%)	Formic Acid (%)	Total (%)
Pt-3.5 V	11.13±2.79	1.03±0.15	86.31±3.69	98.48±1.72
Pt-3.0 V	8.4±1.8	0.43±0.15	85.49±4.79	94.32±5.32
Ni-3.0 V	3.9±0.61	0.73±0.23	97.29±0.82	101.9±0.47
Ni-2.8 V	6.53±0.64	0.73±0.15	93.94±2.23	101.2±2.87
Ni-2.7 V	6.8±2.11	0.73±0.21	94.47±1.88	102.1±1.83
Ni-2.6 V	11.07±3.23	0.9±0.1	84.81±2.45	96.37±1.41
NiFeOx-2.7 V	10.3±1.91	0.63±0.23	90.41±2	101.35±1.07
DSE-2.7 V	5.67±0.42	0.63±0.21	92.49±1.86	98.79±1.51
DSE-2.6 V	6.2±0.89	0.47±0.12	83.8±5.62	90.47±4.9

Table 3.6 Energy efficiencies for all the products from CO_2 reduction in a two-electrode system with various anodes at different E_{cell}.

Condition	H_2 (%)	CO (%)	Formic Acid (%)	Total (%)
Pt-3.5 V	3.91±0.99	0.39±0.06	34.52±1.48	38.82±0.72
Pt-3.0 V	3.44±0.74	0.19±0.07	39.89±2.23	43.53±2.43
Ni-3.0 V	1.57±0.25	0.32±0.09	44.54±0.19	46.43±0.03
Ni-2.8 V	2.81±0.24	0.34±0.06	46.14±0.18	49.3±0.45
Ni-2.7 V	3.02±0.92	0.35±0.09	48.02±1.14	51.4±0.14
Ni-2.6 V	5.23±1.53	0.46±0.05	45.44±1.32	51.13±0.63
$NiFeO_x$-2.7 V	4.63±0.86	0.31±0.11	46.25±0.86	51.19±0.11
DSE-2.7 V	2.58±0.19	0.31±0.1	47.95±0.96	50.84±0.8
DSE-2.6 V	2.93±0.42	0.24±0.06	45.12±3.02	48.29±2.69

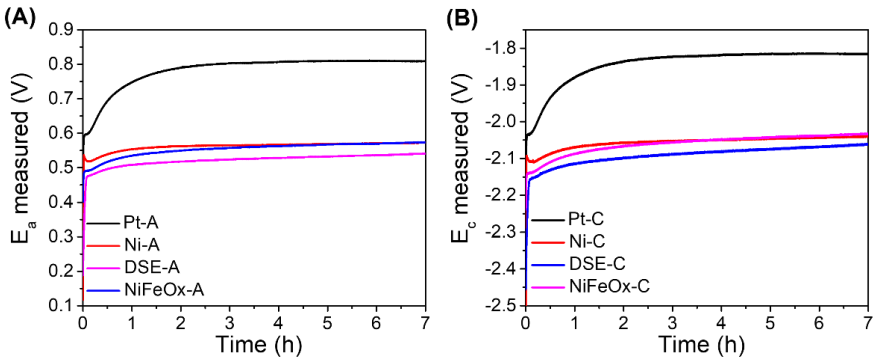

Figure 3.25 The variation of the potentials on (A) anode and (B) cathode in the BDD-based CO_2 electrolyzer during 7-hour CO_2 reduction. Reproduced with permission from ref. [27]. Copyright 2022, American Chemical Society.

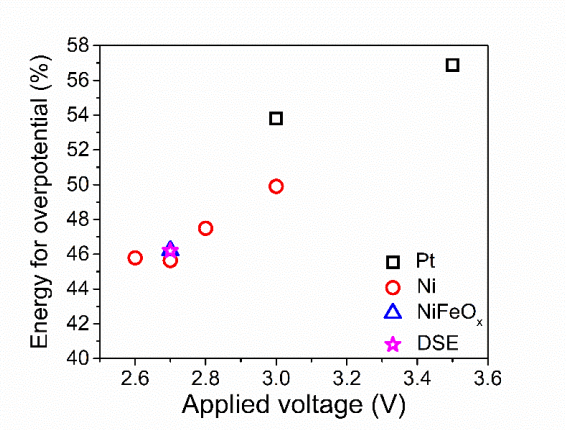

Figure 3.26 Percentage energy distribution of overpotential in the CO_2 electrolyzer. Reproduced with permission from ref. [27]. Copyright 2022, American Chemical Society.

Calculation of the energy distribution in the two-electrodes cell

The calculation method refers to method in Chapter 2. In brief, First, the voltage loss (E_{loss}) is the difference between E_{cell} and the sum of the potentials measured at the anode (E_a) and cathode (E_c), i.e., equation 3.3 (Table 3.7).

$$E_{loss} = E_{cell} - E_a + E_c \qquad (3.3)$$

The applied voltage in the two-electrode CO_2 electrolyzer is divided into 3 parts including the standard electromotive force of the cell reaction (E^0) the voltage loss (E_{loss}) and the voltage consumption of the overpotential as shown in equation 3.4.

$$E_{cell} = E^0 + E_{loss} + E_{overpotential} \qquad (3.4)$$

Owing to the tandem structure of this electrochemical system, the percentage energy distribution can be computed directly from the applied potential. Therefore, in order to work out what the percentage energy loss due to the overpotential is, this was computed by excluding the ECE conversion efficiency for all the products and the uncompensated resistance from the total energy. Table 3.8 shows the specific energy distribution in this electrolyzer and Figure 3.26 shows the energy distribution of the overpotential in the electrolyzer with different anodes.

Table 3.7 Potentials applied at the anode and cathode, and the voltage loss of the resistance at the applied E_{cell}. Potentials are referred to Ag/AgCl (KCl sat) to cathode and anode.

Condition	Cathode (V)	Anode (V)	Resistance (V)
Pt-3.5 V	-2.37±0.01	0.98±0.02	0.15
Pt-3.0 V	-2.14±0.03	0.78±0.02	0.08
Ni-3.0 V	-2.26±0.03	0.63±0.03	0.11
Ni-2.8 V	-2.15±0.01	0.56±0.01	0.09
Ni-2.7 V	-2.1±0.02	0.52±0.01	0.08
Ni-2.6 V	-2.02±0.01	0.5±0.02	0.08
NiFeOx-2.7 V	-2.11±0.01	0.52±0.01	0.07
DSE-2.7 V	-2.13±0.01	0.49±0.01	0.08
DSE-2.6 V	-2.06	0.47±0.01	0.07

Table 3.8 Percentage energy distribution for the electrical-to-chemical energy conversion efficiency (ECE), resistance and overpotential with various anodes and at different applied voltages.

Condition	ECE (%)	Resistance (%)	Overpotential (%)
Pt-3.5 V	38.82	4.29	56.89
Pt-3.0 V	43.53	2.67	53.8
Ni-3.0 V	46.43	3.67	49.9
Ni-2.8 V	49.3	3.21	47.49
Ni-2.7 V	51.4	2.96	45.64
Ni-2.6 V	51.13	3.08	45.79
NiFeOx-2.7 V	51.19	2.59	46.22
DSE-2.7 V	50.84	2.96	46.2
DSE-2.6 V	48.29	2.69	49.02

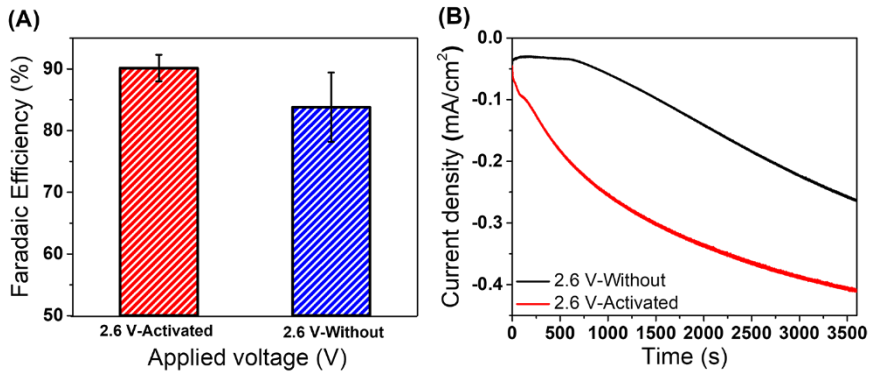

Figure 3.27 (A) Faradaic efficiencies and (B) Current densities in two-electrode eCO_2RR at 2.6 V showing the difference between the activated and non-activated BDD electrode. Activation processes were performed with 1-hour galvanostatic CO_2 reduction at the current densities of −1 mA cm^{-2} before the formal eCO_2RR. Anode electrode is DSE. Reproduced with permission from ref. [27]. Copyright 2022, American Chemical Society.

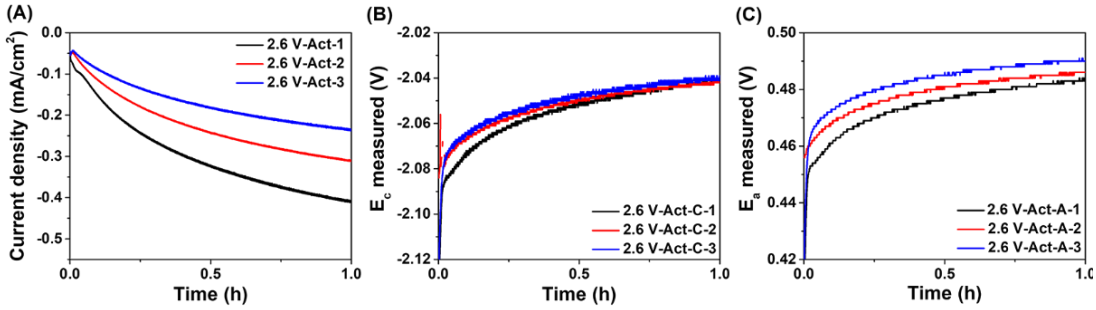

Figure 3.28 The variation of the (A) current densities, potentials on (B) cathode (BDD) and (C) anode (DSE, IrO_x and TaO_x) in the BDD-based CO_2 electrolyzer during the activated CO_2 reduction at 2.6 V. Activation processes were performed with 1-hour galvanostatic CO_2 reduction at the current densities of −1 mA cm^{-2} before the formal eCO_2RR. Reproduced with permission from ref. [27]. Copyright 2022, American Chemical Society.

Actually, as shown in Figure 3.24, generally, BDD electrode shows remarkable repeatability in CO_2 reduction. The repeatability of the activation process can be further verified by the CO_2 reduction experiments at 2.6 V in two-electrode system. As shown in Figure 3.27, with the assistance of the activation process both the Faradaic efficiency and the current densities were significantly improved. This improvement remained stable in the three times experiments. The specific electrochemical performance of the activated CO_2 reduction was shown in Figure 3.28. In addition, as we showed in Figure 3.4, the enhanced CO_2 reduction can always be observed even when BDD was activated with different current densities. This performance also demonstrates the repeatability

of the activation process.

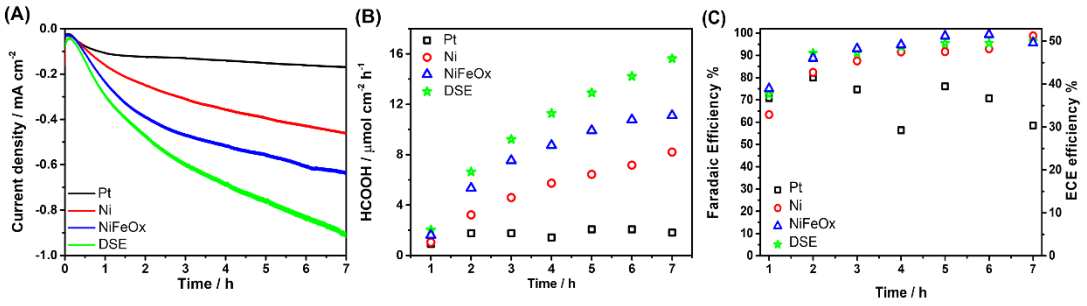

Figure 3.29 (A) Current densities (B) production rate and (C) Faradaic efficiencies / ECE conversion efficiencies of the BDD-based CO_2 electrolyzers which were coupled with different anodes including Pt, Ni, $NiFeO_x$ and DSE. CO_2 reduction electrolysis experiments were performed at the applied voltage of 2.7 V. Reproduced with permission from ref. [27]. Copyright 2022, American Chemical Society.

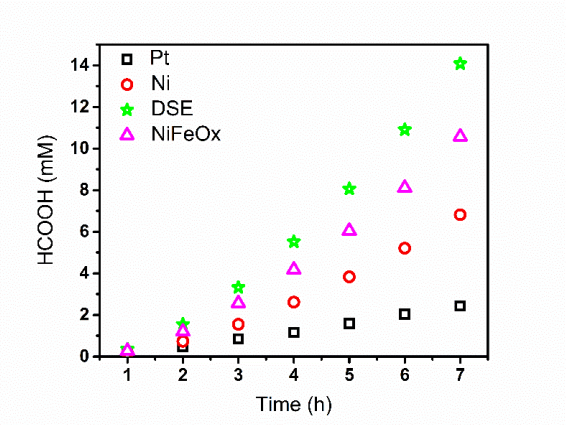

Figure 3.30 The variation of the product concentration (HCOOH) in the BDD-based CO_2 electrolyzers which were coupled with different anodes including Pt, Ni, DSE and NiFeOx. CO_2 reduction electrolysis experiments were performed at the applied voltage of 2.7 V. The volume of the electrolyte was reduced from 55 ml to 49 ml. 1 ml electrolyte was taken for every hour for the characterization. Reproduced with permission from ref. [27]. Copyright 2022, American Chemical Society.

The time-dependence of the self-activation process on BDD was evaluated over 7 hours of eCO_2RRs at the best ECE conversion efficiency potential of 2.7 V (Figure 3.24) by monitoring the current, Faradaic efficiency and ECE conversion efficiency (Figure 3.29).

Current and formic acid production rate increased continuously with the reaction

time suggesting an ongoing activation of the surface (Figure 3.29 A-B) in agreement with previous results, therefore confirming our hypothesis of BDD "self-activation" during eCO_2RR. The Faradaic efficiency of formic acid could reach more than 90% with an average ECE conversion efficiency of 50.2% after 7 hours of continuous eCO_2RR, *viz*. self-activation (Figure 3.29 C). The effect of different OER anodes is clearly evident in the current values (Figure 3.29 A) as lower overpotentials for OER lead to higher currents and then enhanced self-activation that turn into higher production rates (Figure 3.29 B and 3.30) with the series DSE(IrOx)>NiFeOx>Ni>Pt.

Additionally, we would like to draw the attention on the reaction pathways on activated and non-activated BDD which is the same, this is also the reason to choose the term "self-activation". As shown in Figure 3.29, in the BDD-based long term eCO_2RR, both the reaction current density and the Faradaic efficiency for the production of formic acid were continuously improved. This is the essential performance of self-activation and it indicates that during eCO_2RR the activity of BDD for CO_2 reduction will keep increasing which means an improvement of the electroactive surface area. However, due to the low initial reaction current, the process of self-activation is very slow, therefore, it benefits by additional galvanostatic CO_2 reduction performed before the formal eCO_2RR to accelerate the activation process as demonstrated clearly in Figure 3.4. A difference in reaction mechanism can be found when the potential is negative enough to generate the $CO_2^{\bullet-}$ which in that case provided the same Faradaic efficiency (Figure 3.4).

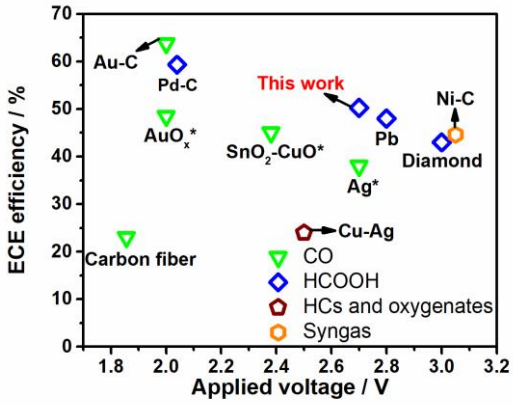

Figure 3.31 Summarized ECE conversion efficiencies of the reported representative CO_2 electrolyzers. The energy efficiencies with * were calculated by ourselves. Reproduced with permission from ref. [27]. Copyright 2022, American Chemical Society.

Finally, we compared the ECE conversion efficiency of the present work with other representative electrocatalysts,[30,41,42,44–50] to show that BDD can reach remarkable performances (Figure 3.31). Although the efficiency of BDD does not reach the level of noble metal electrocatalysts (e.g., Au or Pd), the advantages of BDD are in terms of raw material cost, chemical resistance and physical stability in long term applications where the carbon nanostructure coupled with noble metal electrocatalysts face structural changes and activity loss.[51,52] We are aware that at present, the electrolysis current density of BDD cannot meet the standard of the industrial application, therefore improving the current density of BDD, for example by gas diffusion electrode system, will be our research direction for the future work.

3.4 Conclusion

Here we investigated the mechanism of CO_2 reduction on BDD highlighting a new and until now uncovered mechanism which leads to "self-activation" of the BDD surface during the eCO_2RR. Characterization of the BDD surface by spectroscopic techniques such as XPS and ATR-IR combined with electrochemical analysis with aminoferrocene demonstrated that unidentate carbonate and carboxylic intermediates were generated on the surface of BDD and kept increasing during eCO_2RR. Based on the presence of these intermediates, a new pathway for electrochemical CO_2 reduction was proposed, which was independent of the generation of $CO_2^{\bullet-}$. The CO_2 molecules from the solution first adsorb on the BDD surface as unidentate carbonate and under the application of a suitable negative potential, the unidentate carbonate is converted to a carboxylic intermediate and finally to formate. During eCO_2RR an increasing amount of carboxylic intermediates are generated on the BDD surface meaning an improvement of the electroactive surface area in a process we refer as "self-activation" that improves both reaction current and Faradaic efficiency of eCO_2RR. The technological application performance of the self-activation effect was further estimated by 7-hour eCO_2RR in a flow electrolyzer. Benefiting from the self-activation effect, the BDD electrode reaches an ECE conversion efficiency of 50.2% for the single product of formic acid. This work provides new insights on the mechanism of electrochemical CO_2 reduction at BDD electrodes and demonstrates its potential application as working electrode for eCO_2RR.

3.5 References

(1) Aresta, M.; Dibenedetto, A.; Angelini, A. Catalysis for the Valorization of Exhaust Carbon: From CO_2 to Chemicals, Materials, and Fuels. Technological Use of CO_2. *Chem. Rev.* **2014**, *114* (3), 1709–1742.

(2) Goeppert, A.; Czaun, M.; Jones, J. P.; Surya Prakash, G. K.; Olah, G. A. Recycling of Carbon Dioxide to Methanol and Derived Products-Closing the Loop. *Chem. Soc. Rev.* **2014**, *43* (23), 7995–8048.

(3) Matthessen, R.; Fransaer, J.; Binnemans, K.; De Vos, D. E. Electrocarboxylation: Towards Sustainable and Efficient Synthesis of Valuable Carboxylic Acids. *Beilstein J. Org. Chem.* **2014**, *10*, 2484–2500.

(4) Fiorani, G.; Guo, W.; Kleij, A. W. Sustainable Conversion of Carbon Dioxide: The Advent of Organocatalysis. *Green Chem.* **2015**, *17* (3), 1375–1389.

(5) Nielsen, D. U.; Hu, X. M.; Daasbjerg, K.; Skrydstrup, T. Chemically and Electrochemically Catalysed Conversion of CO_2 to CO with Follow-up Utilization to Value-Added Chemicals. *Nat. Catal.* **2018**, *1* (4), 244–254.

(6) Kondratenko, E. V.; Mul, G.; Baltrusaitis, J.; Larrazábal, G. O.; Pérez-Ramírez, J. Status and Perspectives of CO_2 Conversion into Fuels and Chemicals by Catalytic, Photocatalytic and Electrocatalytic Processes. *Energy Environ. Sci.* **2013**, *6* (11), 3112–3135.

(7) Verma, S.; Kim, B.; Jhong, H. R. M.; Ma, S.; Kenis, P. J. A. A Gross-Margin Model for Defining Technoeconomic Benchmarks in the Electroreduction of CO_2. *ChemSusChem* **2016**, *9* (15), 1972–1979.

(8) Whipple, D. T.; Kenis, P. J. A. Prospects of CO_2 Utilization via Direct Heterogeneous Electrochemical Reduction. *J. Phys. Chem. Lett.* **2010**, *1* (24), 3451–3458.

(9) Singh, A. K.; Singh, S.; Kumar, A. Hydrogen Energy Future with Formic Acid: A Renewable Chemical Hydrogen Storage System. *Catal. Sci. Technol.* **2016**, *6* (1), 12–40.

(10) Yu, X.; Pickup, P. G. Recent Advances in Direct Formic Acid Fuel Cells (DFAFC). *J. Power Sources* **2008**, *182* (1), 124–132.

(11) Bushuyev, O. S.; De Luna, P.; Dinh, C. T.; Tao, L.; Saur, G.; van de Lagemaat, J.; Kelley, S. O.; Sargent, E. H. What Should We Make with CO_2 and How Can We Make It? *Joule* **2018**, *2* (5), 825–832.

(12) Kortlever, R.; Shen, J.; Schouten, K. J. P.; Calle-Vallejo, F.; Koper, M. T. M. Catalysts and Reaction Pathways for the Electrochemical Reduction of Carbon Dioxide. *J. Phys. Chem. Lett.* **2015**, *6* (20), 4073–4082.

(13) White, J. L.; Baruch, M. F.; Pander, J. E.; Hu, Y.; Fortmeyer, I. C.; Park, J. E.; Zhang, T.; Liao, K.; Gu, J.; Yan, Y.; Shaw, T. W.; Abelev, E.; Bocarsly, A. B. Light-Driven Heterogeneous Reduction of Carbon Dioxide: Photocatalysts and Photoelectrodes. *Chem. Rev.* **2015**, *115* (23), 12888–12935.

(14) Koppenol, W. H. & Rush, J. D. Reduction potential of the carbon dioxide/carbon dioxide radical anion: a comparison with other C1 radicals. *J. Phys. Chem.* **1987,** 91 (16), 4429–4430.

(15) Lamy, E.; Nadjo, L.; Saveant, J. M. Standard Potential and Kinetic Parameters of the Electrochemical Reduction of Carbon Dioxide in Dimethylformamide. *J. Electroanal. Chem.* **1977**, *78* (2), 403–407.

(16) Lin, B.; Golshan-Shirazi, S. and Guiochon, G. Effect of mass transfer coefficient on the elution profile in nonlinear chromatography. *J. Phys. Chem.* **1989,** 93 (8), 3363.

(17) Schwarz, H. A.; Dodson, R. W. Reduction Potentials of CO_2 and the Alcohol Radicals. *J. Phys. Chem.* **1989**, *93* (1), 409–414.

(18) Chen, Y.; Li, C. W.; Kanan, M. W. Aqueous CO_2 Reduction at Very Low Overpotential on Oxide-Derived Au Nanoparticles. *J. Am. Chem. Soc.* **2012**, *134* (49), 19969–19972.

(19) Chen, Y.; Kanan, M. W. Tin Oxide Dependence of the CO_2 Reduction Efficiency on Tin Electrodes and Enhanced Activity for Tin/Tin Oxide Thin-Film Catalysts. *J. Am. Chem. Soc.* **2012**, *134* (4), 1986–1989.

(20) Baruch, M. F.; Pander, J. E.; White, J. L.; Bocarsly, A. B. Mechanistic Insights into the Reduction of CO_2 on Tin Electrodes Using in Situ ATR-IR Spectroscopy. *ACS Catal.* **2015**, *5* (5), 3148–3156.

(21) Valenti, G.; Melchionna, M.; Montini, T.; Boni, A.; Nasi, L.; Fonda, E.; Criado, A.; Zitolo, A.; Voci, S.; Bertoni, G.; Bonchio, M.; Fornasiero, P.; Paolucci, F.; Prato, M. Water-Mediated ElectroHydrogenation of CO_2 at Near-Equilibrium Potential by Carbon Nanotubes/Cerium Dioxide Nanohybrids. *ACS Appl. Energy Mater.* **2020**, *3* (9), 8509–8518.

(22) Ikemiya, N.; Natsui, K.; Nakata, K.; Einaga, Y. Long-Term Continuous Conversion of CO_2 to Formic Acid Using Boron-Doped Diamond Electrodes. *ACS Sustain. Chem. Eng.* **2018**, *6* (7), 8108–8112.

(23) Kashiwada, T.; Watanabe, T.; Ootani, Y.; Tateyama, Y.; Einaga, Y. A Study on Electrolytic Corrosion of Boron-Doped Diamond Electrodes When Decomposing Organic Compounds. *ACS Appl. Mater. Interfaces* **2016**, *8* (42), 28299–28305.

(24) Natsui, K.; Iwakawa, H.; Ikemiya, N.; Nakata, K.; Einaga, Y. Stable and Highly Efficient Electrochemical Production of Formic Acid from Carbon Dioxide Using Diamond Electrodes. *Angew. Chemie - Int. Ed.* **2018**, *57* (10), 2639–2643.

(25) Tomisaki, M.; Kasahara, S.; Natsui, K.; Ikemiya, N.; Einaga, Y. Switchable Product Selectivity in the Electrochemical Reduction of Carbon Dioxide Using Boron-Doped Diamond Electrodes. *J. Am. Chem. Soc.* **2019**, *141* (18), 7414–7420.

(26) Einaga, Y. Diamond Electrodes for Electrochemical Analysis. *J. Appl. Electrochem.* **2010**, *40* (10), 1807–1816.

(27) Du, J.; Fiorani, A.; Inagaki, T.; Otake, A.; Murata, M.; Hatanaka, M.; Einaga, Y. A New Pathway for CO_2 Reduction Relying on the Self-Activation Mechanism of Boron-Doped Diamond Cathode . *JACS Au* **2022**, *2*, 1375-1382.

(28) Xu, J.; Natsui, K.; Naoi, S.; Nakata, K.; Einaga, Y. Effect of Doping Level on the Electrochemical Reduction of CO_2 on Boron-Doped Diamond Electrodes. *Diam. Relat. Mater.* **2018**, *86* (March), 167–172.

(29) Xu, J.; Einaga, Y. Effect of Sp^2 Species in a Boron-Doped Diamond Electrode on the Electrochemical Reduction of CO_2. *Electrochem. commun.* **2020**, *115* (April), 106731.

(30) Du, J.; Fiorani, A.; Einaga, Y. An Efficient, Formic Acid Selective CO_2 electrolyzer with a Boron-Doped Diamond Cathode. *Sustain. Energy Fuels* **2021**, *5* (10), 2590–2594.

(31) Kasahara, S.; Natsui, K.; Watanabe, T.; Yokota, Y.; Kim, Y.; Iizuka, S.; Tateyama, Y.; Einaga, Y. Surface Hydrogenation of Boron-Doped Diamond Electrodes by Cathodic Reduction. *Anal. Chem.* **2017**, *89* (21), 11341–11347.

(32) Thornton, E. W.; Harrison, P. G. Tin Oxide surfaces part 1. *J. Chem. Soc., Faraday Trans. 1* **1975**, 71, 461-472.

(33) Cagnon, B.; Py, X.; Guillot, A.; Joly, J. P.; Berjoan, R. Pore Structure Modification of Pitch-Based Activated Carbon by NaOCl and Air Oxidation/Pyrolysis Cycles. *Microporous Mesoporous Mater.* **2005**, *80* (1–3), 183–193.

(34) Dolci, L. S.; Quiroga, S. D.; Gherardi, M.; Laurita, R.; Liguori, A.; Sanibondi,

P.; Fiorani, A.; Calzà, L.; Colombo, V.; Focarete, M. L. Carboxyl Surface Functionalization of Poly(L -Lactic Acid) Electrospun Nanofibers through Atmospheric Non-Thermal Plasma Affects Fibroblast Morphology. *Plasma Process. Polym.* **2014**, *11* (3), 203–213.

(35) Věžník, J.; Konhefr, M.; Trnková, L.; Skládal, P.; Lacina, K. Elusive PKa' of Aminoferrocene Determined with Voltammetric Methods in Buffered and Unbuffered Systems and Practical Aspects of Such Experiments. *Electrochim. Acta* **2019**, *318*, 534–541.

(36) Costentin, C.; Robert, M.; Savéant, J. M. Catalysis of the Electrochemical Reduction of Carbon Dioxide. *Chem. Soc. Rev.* **2013**, *42* (6), 2423–2436.

(37) Becke, A. D. Density-Functional Exchange-Energy Approximation with Correct Assymptonic Behaviour. *Phys. Rev. A* **1988**, 38, 3098-3100.

(38) Lee, C.; Yang, W.; Parr, R. G. Development of the Colle-Salvetti Correlation-Energy Formula into a Functional of the Electron Density. *Phys. Rev. B* **1988**, 37, 785-789.

(39) Nishihara, S.; Otani, M. Hybrid Solvation Models for Bulk, Interface, and Membrane: Reference Interaction Site Methods Coupled with Density Functional Theory. *Phys. Rev. B* **2017**, *96*, 115429.

(40) Otani, M.; Sugino, O. First-Principles Calculations of Charged Surfaces and Interfaces: A Plane-Wave Nonrepeated Slab Approach. *Phys. Rev. B - Condens. Matter Mater. Phys.* **2006**, *73*, 115407.

(41) Zhou, X.; Liu, R.; Sun, K.; Chen, Y.; Verlage, E.; Francis, S. A.; Lewis, N. S.; Xiang, C. Solar-Driven Reduction of 1 atm of CO_2 to Formate at 10% Energy-Conversion Efficiency by Use of a TiO_2-Protected III-V Tandem Photoanode in Conjunction with a Bipolar Membrane and a Pd/C Cathode. *ACS Energy Lett.* **2016**, 1, 764-770.

(42) Vermaas, D. A.; Smith, W. A. Synergistic Electrochemical CO_2 Reduction and Water Oxidation with a Bipolar Membrane. *ACS Energy Lett.* **2016**, *1* (6), 1143–1148.

(43) McCrory, C. C. L.; Jung, S.; Peters, J. C.; Jaramillo, T. F. Benchmarking Heterogeneous Electrocatalysts for the Oxygen Evolution Reaction. *J. Am. Chem. Soc.* **2013**, *135* (45), 16977–16987.

(44) Yamamoto, T. et al. Electrochemical Reduction of CO_2 in the Micropores of Activated Carbon Fibers. *J. Electrochem. Soc.* **2000**, 147, 3393-3400.

(45) Verma, S.; Hamasaki, Y.; Kim, C.; Huang, W.; Lu, S.; Jhong, H. R. M.; Gewirth,

A. A.; Fujigaya, T.; Nakashima, N.; Kenis, P. J. A. Insights into the Low Overpotential Electroreduction of CO_2 to CO on a Supported Gold Catalyst in an Alkaline Flow Electrolyzer. *ACS Energy Lett.* **2018**, *3* (1), 193–198.

(46) Lu, X.; Leung, D. Y. C.; Wang, H.; Xuan, J. A High Performance Dual Electrolyte Microfluidic Reactor for the Utilization of CO_2. *Appl. Energy* **2017**, *194*, 549–559.

(47) Gurudayal; Bullock, J.; Srankó, D. F.; Towle, C. M.; Lum, Y.; Hettick, M.; Scott, M. C.; Javey, A.; Ager, J. Efficient Solar-Driven Electrochemical CO_2 Reduction to Hydrocarbons and Oxygenates. *Energy Environ. Sci.* **2017**, *10* (10), 2222–2230.

(48) Yamamoto, T.; Tryk, D. A.; Fujishimal, A.; Ohata, H. Production of Syngas plus Oxygen from CO_2 in a Gas-Diffusion Electrode-Based Electrolytic Cell. *Electrochim. Acta* **2002**, *47* (20), 3327–3334.

(49) Schreier, M.; Curvat, L.; Giordano, F.; Steier, L.; Abate, A.; Zakeeruddin, S. M.; Luo, J.; Mayer, M. T.; Grätzel, M. Efficient Photosynthesis of Carbon Monoxide from CO_2 Using Perovskite Photovoltaics. *Nat. Commun.* **2015**, *6*, 7326.

(50) Schreier, M.; Héroguel, F.; Steier, L.; Ahmad, S.; Luterbacher, J. S.; Mayer, M. T.; Luo, J.; Grätzel, M. Solar Conversion of CO_2 to CO Using Earth-Abundant Electrocatalysts Prepared by Atomic Layer Modification of CuO. *Nat. Energy* **2017**, *2*, 17087.

(51) Hegge, F.; Sharman, J.; Moroni, R.; Thiele, S.; Zengerle, R.; Breitwieser, M.; Vierrath, S. Impact of Carbon Support Corrosion on Performance Losses in Polymer Electrolyte Membrane Fuel Cells. *J. Electrochem. Soc.* **2019**, *166* (13), F956–F962.

(52) Li, F.; Medvedeva, X. V.; Medvedev, J. J.; Khairullina, E.; Engelhardt, H.; Chandrasekar, S.; Guo, Y.; Jin, J.; Lee, A.; Thérien-Aubin, H.; Ahmed, A.; Pang, Y.; Klinkova, A. Interplay of Electrochemical and Electrical Effects Induces Structural Transformations in Electrocatalysts. *Nat. Catal.* **2021**, *4* (6), 479–487.

Chapter 4

Electrochemical CO_2 reduction to CO facilitated by reduced boron-doped diamond

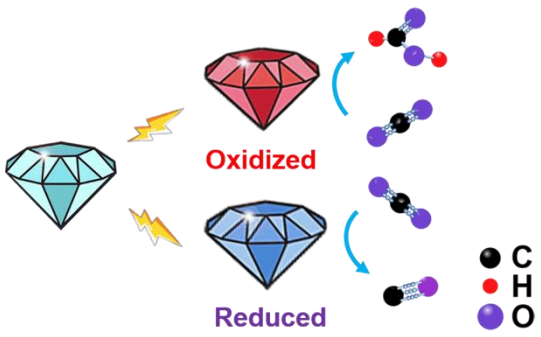

4.1 Introduction

The technological application of CO_2 utilization by reduction undertakes the task of artificial carbon offset in carbon neutrality.[1,2] If it is powered by sunlight, the solar energy will be stored as fuel to achieve high-efficiency artificial photosynthesis.[3] Among the various CO_2 reduction methods, electrochemical CO_2 reduction reaction (eCO_2RR) was proved to be a clean and efficient way converting CO_2 into value-added chemicals, such as CO,[4] formic acid, and short chain hydrocarbons or oxygenates.[5–7] In these products, CO not only plays an important role as an energy carrier, but also is a versatile precursor in the chemical industry.[4,8,9] Moreover, CO spontaneously separates from the electrolyte solution without requiring energy consumption for a separation process. From the view of production rate, investigations on the catalytic site of eCO_2RR are crucial, since the amount of catalytic sites can directly affect the reduction rate of CO_2.

In the literature concerning the catalytic site for eCO_2RR, the function of the undercoordinated site is commonly considered to play a pivotal role.[10,11] Basically, unpaired electrons are usually located in undercoordinated sites which are highly reactive and easily undergo reaction to intermediates. The introduction of heteroatoms is a familiar approach to increase the undercoordinated site therefore enhancing the catalytic activity.[12,13] In addition, the formation of the undercoordinated site also relies on the structural and intrinsic defects in the electrode.[14–16] Another kind of possible catalytic site for eCO_2RR could be attributed to the oxidized elements on the electrode surface. Kanan et al. proposed that oxide-derived metal electrodes (such as Au, Cu, Sn) possess outstanding reactivity and remarkable product selectivity for eCO_2RR.[17–19] Gong's group reported that compared with Cu^0, Cu^+ can form stronger adsorption with CO and is more likely to boost C-C coupling.[20] Furthermore, the presence of some oxygenates on the electrode surface were also proved to be beneficial to eCO_2RR.[21,22] Until now, mechanisms on eCO_2RR share both views among undercoordinated site or oxidized elements while other active sites are less investigated.

Boron doped diamond (BDD) possesses the advantages of low raw-material cost, non-toxic, long-term stability and strong corrosion resistance.[23,24] These features are highly competitive especially when compared with conventional metal electrodes.[25,26] Moreover, in eCO_2RR, high product selectivity and over 50% electrical-to-chemical energy conversion efficiency have been achieved by BDD-based electrolyzer.[21,27,28] In

the research on the catalytic site of eCO_2RR by BDD, two interesting results are worth noting: 1) increasing the proportion of heteroatoms (boron) in BDD had no positive effect on eCO_2RR,[29] and 2) both the sp^2 moiety itself and the structural defects caused by changes in carbon hybridization could not improve the catalytic activity of BDD toward eCO_2RR.[30] These seem to imply that the amount of undercoordinated site has little effect on the catalytic activity of eCO_2RR on BDD. In eCO_2RR, the main product of BDD electrode can be switched between CO and formic acid depending on the electrolyte solution.[31] Our previous investigations revealed that in a reaction system capable of producing formic acid, the catalytic sites for eCO_2RR are derived from the oxygen-terminated surface generated after oxidative pretreatment.[21,23] However, in the reaction system for CO production on BDD electrode, the surface state should be further investigated.

Here, we get insights into the optimal surface state for electrochemical CO_2 reduction to CO on BDD electrodes by providing evidences from the investigation of the performance when the BDD surface is in various redox states. It is found that a relatively stable reduction state showed the best catalytic activity for reducing CO_2 to CO, which is different from the situation of most oxidized electrodes reported so far.[17–19,21] Compared with the untreated BDD electrode, the Faradaic efficiency for CO production on the reduced BDD increased from 49% to 64%, and its production rate reached 23 μmol cm^{-2} h^{-1}, which was more than three times that of the BDD electrode set as comparison.

4.2 Experimental section

Materials. $KClO_4$, KOH, H_2SO_4, 2-propanol, acetone, and trimethyl borate were purchased from Wako Pure Chemical Industries Ltd. All reagents in this work were used without any further purification. The deionized (DI) water was obtained from a Simply-Lab water system (DIRECT-Q 3 UV, Millipore) with a resistivity of 18.2 MΩ·cm at 25 °C. Formic acid for HPLC calibration was purchased from FUJIFILM Wako pure Chemical Corporation. Hydrogen and carbon monoxide for GC calibration were purchased from GL Sciences.

Electrochemical setup. The electrochemical measurements were performed with the assistance of a potentiostat/galvanostat system (PGSTAT204, Metrohm Autolab). Ag/AgCl, KCl (sat'd) was utilized as the reference electrode for each electrochemical measurement in this work. BDD electrodes were pretreated at various current densities

in N_2-saturated 0.1 M $KClO_4$ aqueous solution. The open circuit potential (OCP) was measured in static 0.1 M $KClO_4$ solution.

Preparation and characterization of BDD electrodes. The polycrystalline BDD film was synthesized on a Si (100) wafer substrate by a microwave plasma-assisted chemical vapor deposition (MPCVD) system (AX5400, Cornes Technologies Ltd.). The concentration of boron in the BDD electrode was controlled by adjusting the ratio between the carbon source (acetone) and the boron source (trimethyl borate) and was set to 1%. Raman spectrum was recorded by an Acton SP2500 (Princeton Instruments) with a 532 nm laser (Figure 4.1). The specific elemental information of BDD surface was analyzed with an X-ray photoelectron spectrometer (XPS, JPS-9010 TR, JEOL). The baseline in the XPS spectra was created according to the Shirley background. The C 1s spectra were deconvoluted referring to Gaussian functions. Peaks deconvoluted from the C 1s spectra were assigned to the components as followed: 283.0 eV (sp^2 C-C bond), 284.1 eV (C-H bond), 284.75 eV (sp^3 C-C bond) and 285.3 eV (C-O bond).

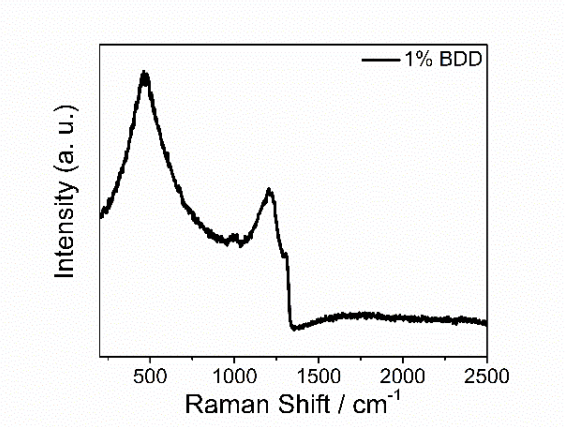

Figure 4.1 Raman spectrum for the BDD electrode with a boron concentration of 1%.

Electrochemical CO_2 reduction and product analysis. Before formal eCO_2RR experiments, 2-propanol and DI water were used to clean the electrode surface with an ultrasonic treatment for 10 minutes each. A two-compartment flow cell made of polytetrafluoroethylene (PTFE) were used to perform the electrochemical measurements, with the same configuration as our previous work.[28] The 1 % BDD, Pt and Ag/AgCl (KCl sat'd) were set as the working, counter and reference electrodes, respectively. Nafion NRE-212 (Sigma Aldrich) was employed to separate the anode and cathode chambers of the cell. Several cyclic voltammetry (CV) scans (including 10 cycles from a potential of -3.5 V to 3.5 V and 20 cycles from 0 V to 3.5 V in 0.1 M H_2SO_4 with a scan rate of 0.5 V s^{-1}) were set as a pretreatment before eCO_2RR to assure

reproducibility and cleanliness of the BDD surface. 0.1 M $KClO_4$ and 1 M KOH were employed as the catholyte and anolyte, respectively (50 mL each). Oxygen in the catholyte was removed by introducing N_2 for 30 min and CO_2 bubbling was performed for 60 min to achieve a CO_2-sauturated solution. During electrolysis, CO_2 bubbling was sustained at a flow rate of 10 ml min^{-1} and the flow rate of the electrolyte was set at 400 ml min^{-1}.

After the electrolysis experiments of eCO_2RR, all of the products were quantified. Formic acid was quantified with high-performance liquid chromatography (HPLC, CDD-10A, Shimadzu Corp.). The gaseous products (CO and H_2) were collected in an aluminum gas bag (GL Sciences) and quantified using gas chromatography (GC-2014, Shimadzu Corp.).

4.3 Results and discussion

Firstly, eCO_2RR experiments were carried out at various potentials to identify the best potential range for CO production on 1% BDD electrodes (Figure 4.2 A).

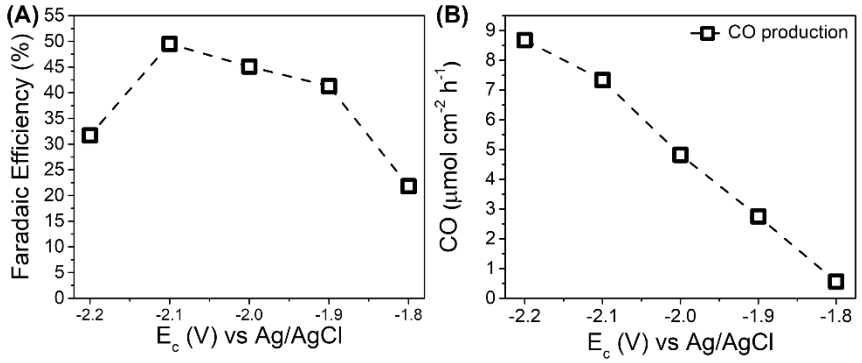

Figure 4.2 (A) Faradaic efficiency and (B) production rate for CO on 1% BDD electrode from -1.8 V to -2.2 V in 0.1 M $KClO_4$ aqueous solution.

It was found that the Faradaic efficiency for CO production was more remarkable when the reduction potential was in the range of -2.1 V to -1.9 V, peaking at 49% when the electrolysis potential was set at -2.1 V. Under the influence of the increasing reaction current, the production rate of CO was gradually improved as the eCO_2RR was performed at more negative potentials (Figure 4.2 B and Figure 4.3). Additionally, in our previous work, we have demonstrated that increasing the concentration of boron in BDD electrodes has no contribution to the catalytic activity of CO_2 reduction to formic acid.[29] In order to further verify whether the doped boron atoms contribute to the

catalytic activity in CO production, we prepared BDD with a boron concentration of 2%, and performed eCO_2RR at -2.1 V and -2.0 V. Compared with the eCO_2RR performance of 1% BDD, although the electrolysis current was improved along with the increasing boron concentration (Figure 4.4), the production rate of CO was still at the same level as that of 1% BDD (Table 4.1-4.2). Therefore, we conclude that undercoordinated atoms as result of boron doping are not a source of catalytic sites for eCO_2RR on BDD electrode. Considering that the electrochemical properties of BDD is greatly affected by its surface state,[32,33] we speculate that the amount of catalytic sites for eCO_2RR might be attributed to the redox state of the carbon atoms on the BDD surface.

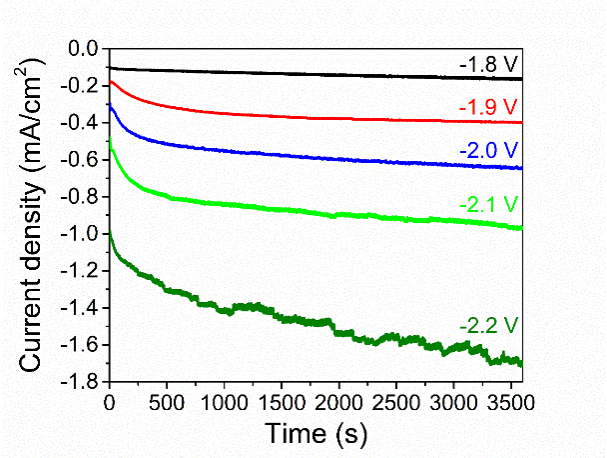

Figure 4.3 Current densities of electrochemical CO_2 reduction on 1% BDD at various potentials. Potentials are referred to Ag/AgCl (KCl sat).

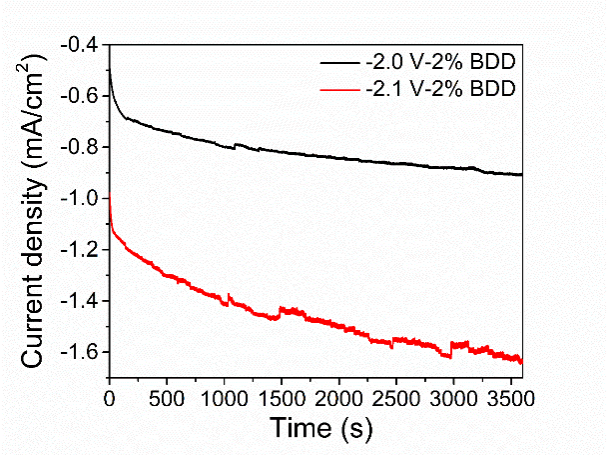

Figure 4.4 Current densities of electrochemical CO_2 reduction on 2% BDD at -2 V and -2.1 V. Potentials are referred to Ag/AgCl (KCl sat).

Table 4.1 Faradaic efficiencies for all products and production rate of CO in electrochemical CO_2 reduction by 1% BDD at various potentials. Potentials are referred to Ag/AgCl (KCl sat).

Potential (V)	H_2 (%)	CO (%)	Formic acid (%)	Production rate ($\mu mol\ cm^{-2}\ h^{-1}$)
-1.8	31.9	21.8	2.74	0.56
-1.9	39.1	41.3	5.02	2.75
-2.0	31.1	45.1	11.54	4.82
-2.1	30.8	49.5	11.22	7.34
-2.2	53.1	31.7	7.2	8.68

Table 4.2 Faradaic efficiencies for all products and production rate of CO in electrochemical CO_2 reduction by 2% BDD at -2 V and -2.1 V. Potentials are referred to Ag/AgCl (KCl sat).

Potential (V)	H_2 (%)	CO (%)	Formic acid (%)	Production rate ($\mu mol\ cm^{-2}\ h^{-1}$)
-2	54.5	31.3	11.36	4.78
-2.1	53.5	25.4	5.78	6.91

Galvanostatic electrolysis was applied as pretreatment to activate the surface of BDD electrodes with the current densities from anodic to cathodic (Figure 4.5) in a nitrogen-saturated solution of 0.1 M $KClO_4$, in order to investigate the performance of eCO_2RR for CO production when BDD is in various redox states.

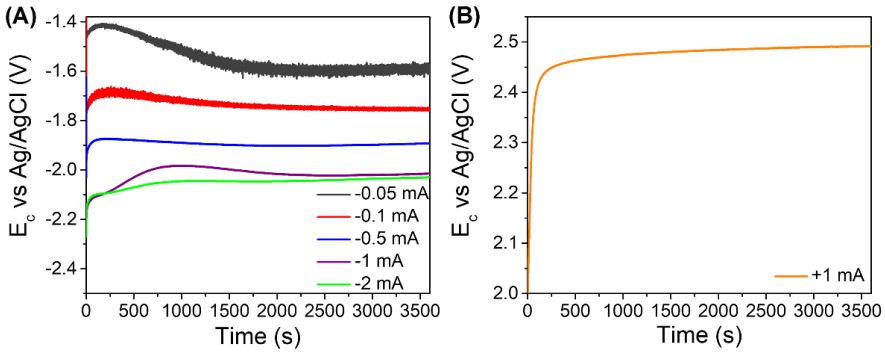

Figure 4.5 The variation of the potentials on (A) reduced and (B) oxidized BDD electrodes during the pretreatment in N_2 saturated $KClO_4$ aqueous solution.

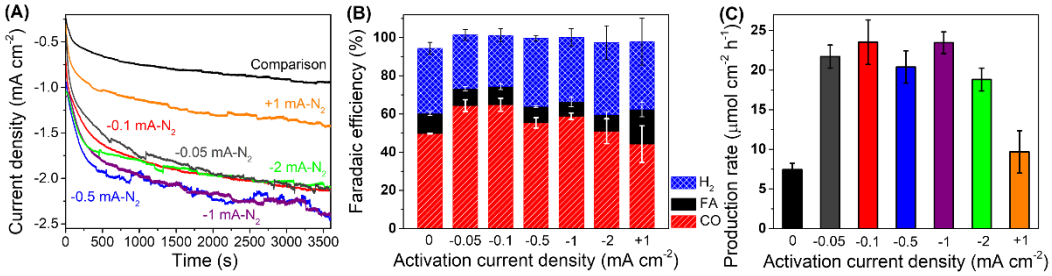

Figure 4.6 (A) Current densities, (B) Faradaic efficiencies and (C) production rate of CO in eCO_2RR at -2.1 V showing the difference between BDD electrodes which were treated by various activation currents (1 mA cm^{-2}, -0.05 mA cm^{-2}, -0.1 mA cm^{-2}, -0.5 mA cm^{-2}, -1 mA cm^{-2}, -2 mA cm^{-2}). The error bars show the standard deviation (n=3). Reference electrode: Ag/AgCl, KCl (sat'd).

Table 4.3 Faradaic efficiencies for all products and production rate of CO in electrochemical CO_2 reduction at -2.1 V by 1% BDD electrodes which were activated at various current densities in N_2 saturated $KClO_4$ aqueous solutions. Potentials are referred to Ag/AgCl (KCl sat).

Condition	H_2 (%)	CO (%)	Formic acid (%)	Production rate (μmol/cm^2 h)
Comparison	34.07±3.11	49.77±0.25	10.55±1.1	7.45±0.8
-0.05 mA	28.17±2.84	64.37±3.11	8.87±1.08	21.71±1.45
-0.1 mA	26.9±3.38	64.83±3.4	9.51±1.57	23.53±2.81
-0.5 mA	35.7±1.49	55.37±2.7	8.57±0.4	20.4±2.04
-1 mA	33.83±4.51	58.8±1.71	7.51±2.45	23.45±1.37
-2 mA	37.7±8.83	50.97±6.43	8.67±1.66	18.81±1.43
+1 mA	35.53±12.31	44.23±9.59	18.16±3.86	9.68±2.67

Then the eCO_2RR was performed at -2.1 V, and the BDD electrodes activated by reductive pretreatment showed notable improvements in catalytic activity if compared with the performance of the non-activated BDD electrode (Figure 4.6). When the activation current was set at -1 mA cm^{-2}, the current density of the activated BDD reaches -2.4 mA cm^{-2} after 1 h of eCO_2RR, while the reaction current of the comparison BDD is only -0.9 mA cm^{-2} (Figure 4.6 A). Moreover, the increased reactivity was also reflected in the production rate of CO. After the activation process by -1 mA cm^{-2}, the production rate of CO increased from 7.45 μmol cm^{-2} h^{-1} to 23.45 μmol cm^{-2} h^{-1}, which was threefold increase compared to the non-activated BDD electrode, and the Faradaic efficiency also increased from 49.8% to 58.8% (Figure 4.6B and C). The improvement of the production rate indicates that the amount of catalytic sites for CO production on

the BDD surface was greatly increased. It is noteworthy that the Faradaic efficiency for CO production was further improved to 64.8% when BDD was subjected to a lower activation current (i.e., -0.1 mA cm^{-2}), but the production rate of CO remained at the same level as when activated by -1 mA cm^{-2}. This performance indicates that when the activation current is increased from -0.1 mA cm^{-2} to -1 mA cm^{-2}, the amount of catalytic sites for eCO_2RR was not altered, while the activity for hydrogen evolution reaction was gradually enhanced. As the activation current was increased up to -2 mA cm^{-2}, the Faradaic efficiency of hydrogen evolution was further enhanced to 37.7% (Figure 4.6B, Table 4.3). Under the competition of the hydrogen evolution reaction, the production rate of CO decreased from 23.45 μmol cm^{-2} h^{-1} to 18.81 μmol cm^{-2} h^{-1}. Besides, we observed that when the BDD electrode was oxidized with an activation current of +1 mA cm^{-2}, the improvement of CO production was very limited, but the Faradaic efficiency of formic acid was significantly improved (Figure 4.6B, Table 4.3). This result is in agreement with our previous investigations.[21,23] Based on the above experimental information, we found that the catalytic activity of BDD electrodes for CO_2 reduction to CO can hardly benefit from excessive reductive or oxidative pretreatment. Only if the BDD electrode was treated with a relatively low reduction current (e.g., -0.1 mA cm^{-2} or -1 mA cm^{-2}), the amount of catalytic sites for CO production in eCO_2RR was the most prominent.

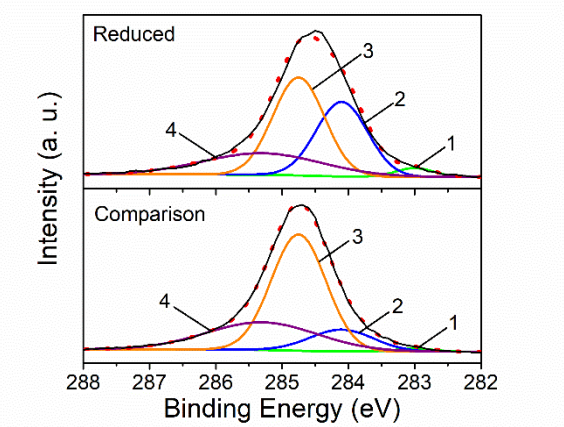

Figure 4.7 Deconvoluted C 1s spectra showing the different surface information between the comparison and reduced BDD electrodes. The relative components include (1) sp^2 C-C (green), (2) C-H (blue), (3) sp^3 C-C (orange) and (4) C-O (purple).

Table 4.4 Relative abundance of the surface components (%) on the BDD electrodes.

	sp^2 C-C	C-H	sp^3 C-C	C-O
Reduced	2.87	32.55	42.78	21.80
Comparison	1.1	12.69	58.07	28.13

XPS measurements were first adopted to identify the species of the surface components on BDD electrodes. As shown in Figure 4.7, the C 1s spectra of the reduced and comparison BDD electrodes were deconvoluted into four carbon species including sp^2 C-C, C-H, sp^3 C-C and C-O. According to our previous works,[32,33] the electrochemical performance exhibited by BDD electrodes varies depending on the species of surface terminations.

Through the analysis on the content of C-O bonds and C-H bonds (Table 4.4), we observed that after the pretreatment by reductive current, the ratio of C-H / C-O on the BDD electrodes increased from 0.45 to 1.49. This means that when the electrode surface is activated by reductive current, the hydrogen termination will replace the oxygen termination as the main factor affecting the electrochemical performance of BDD electrodes. As a result, the BDD electrodes with fewer -OH terminations are more capable of producing CO in eCO_2RR. Considering the improvement for the formic acid production shown in Figure 4.6 B and our previous researches,[21,23] we believe that the -OH terminations on the BDD electrodes can effectively promote the formation of formic acid, but it has no obvious benefit for the CO production in eCO_2RR.

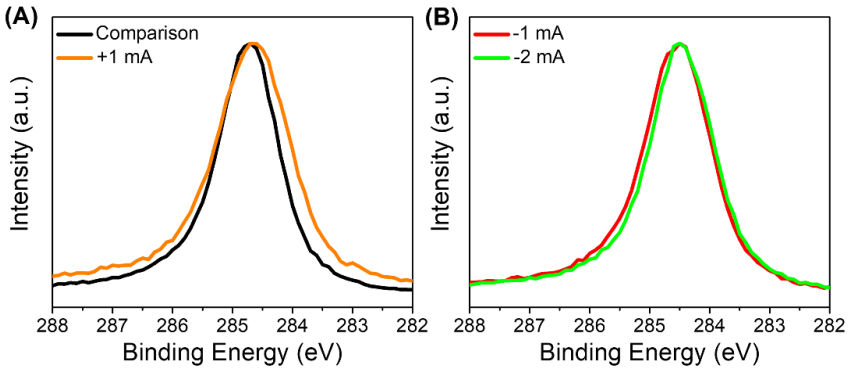

Figure 4.8 Compared XPS spectra showing the surface information of (A) the comparison BDD and the oxidized BDD treated by +1 mA cm^{-2}, and (B) the reduced BDD electrodes treated by -1 mA cm^{-2} and -2 mA cm^{-2} respectively.

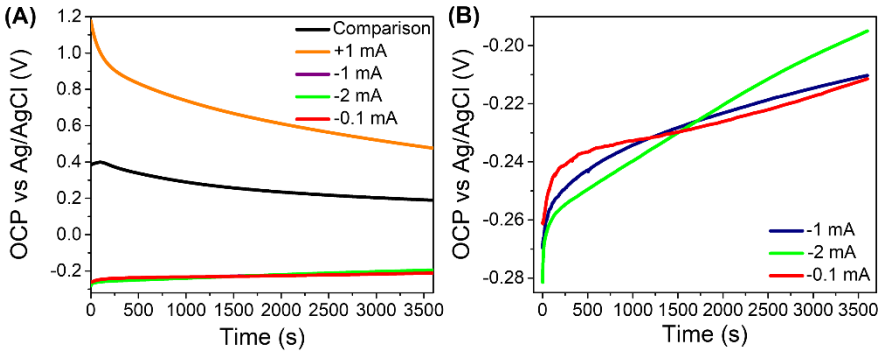

Figure 4.9 (A) Variation of OCPs as a function of time for BDD electrodes pretreated with different currents: comparison BDD, oxidized BDD at 1 mA cm^{-2} and reduced BDD at -0.1, -1, and -2 mA $cm^{-2.}$ (B) Enlarged figure showing the OCP details of the reduced BDD electrodes. Reference electrode: Ag/AgCl, KCl (sat'd).

Concerning the surface analysis on cathodic-reduced or anodic-oxidized BDD electrodes, the XPS measurements is not sensitive enough to clearly distinguish the surface variation caused by electrochemical pretreatments in this work (Figure 4.8). Open circuit potential (OCP) measurements were further performed to analyze and obtain information of the BDD surface state which was treated by various current densities. The corresponding results are shown in Figure 4.9.

We observed that the OCP of the BDD electrode subjected to the pretreatment by +1 mA cm^{-2} was in a more positive potential region than that of the comparison sample (Figure 4.9 A), while the OCPs of the BDD electrodes activated by the cathodic current densities were located at more negative position (Figure 4.9 B). Thus, it is demonstrated that the BDD surfaces activated by -0.1 mA cm^{-2}, -1 mA cm^{-2}, -2 mA cm^{-2} were in a reduced state, while the +1 mA cm^{-2} treated BDD surface was in an oxidized state. The repeatability of the OCP measurements were verified by 3 times experiments on the comparison sample (Figure 4.10). In addition, the OCP of the electrodes reflects the stability of the surface state. The OCP of the BDD electrode treated by +1 mA cm^{-2} showed a standard deviation of 0.145 V over the 1-hour measurement. In comparison, the standard deviation of OCPs associated with BDD electrodes activated by -0.1 mA cm^{-2}, -1 mA cm^{-2} and -2 mA cm^{-2} were 0.009 V, 0.013 V and 0.019 V, respectively (Table 4.5). These results suggest that compared with the BDD in the oxidized state, the reduced BDD surface exhibits higher stability, moreover as the activation current decreases, the surface state of the BDD electrode becomes more stable.

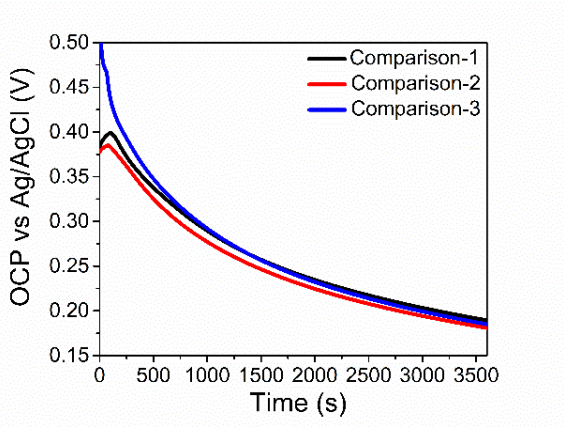

Figure 4.10 Open circuit potential (OCP) of the comparison BDD.

Table 4.5 Statistical parameters of the open circuit potentials of BDD electrodes which were pretreated at various current densities in N_2-saturated 0.1 M $KClO_4$ aqueous solution. Potentials are referred to Ag/AgCl (KCl sat'd).

Condition	Mean / V	Standard Deviation / V
Comparison	0.260	0.059
+1 mA/cm^2	0.664	0.145
-0.1 mA/cm^2	-0.227	0.009
-1 mA/cm^2	-0.227	0.013
-2 mA/cm^2	-0.225	0.019

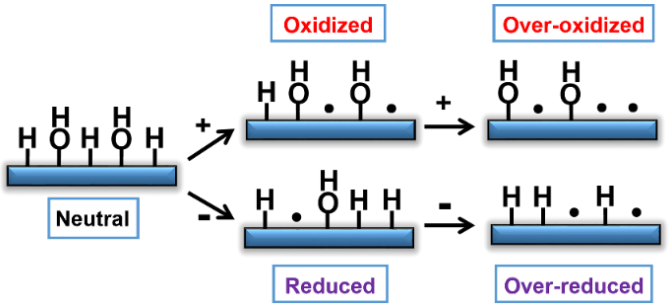

Figure 4.11 Schematic diagram showing hypothetical surface state of BDD electrode after electrochemical oxidation/reduction pretreatments.

Taking together the experimental results for eCO_2RR and the surface information from XPS analysis and OCP, we infer that a reduced surface state is stable and an optimal choice for the eCO_2RR on BDD electrodes toward CO production, with a mechanistic speculation on the variation of the BDD surface as presented in Figure 4.11.

The essence of the pretreatment on BDD electrodes with different current densities is to carry out hydrogen or oxygen evolution reactions. During the pretreatment electrolysis, when the reaction products are released from the BDD electrode, possibly unpaired electrons will be left on the electrode surface. Unpaired electrons are facile to gradually form further coupling with protons or hydroxyl groups in solution, resulting in unstable surface state and enhancing the reactivity of hydrogen evolution,[34–36] which is a competing reaction of eCO_2RR. With the rapid evolution of hydrogen/oxygen in the pretreatment, the amount of unpaired electrons on the BDD surface will also increase. Consequently, we observed that with the increase of the pretreatment current, the OCP variation over time became larger, and the Faradaic efficiency of the hydrogen evolution was gradually increased (Figure 4.6 B, Table 4.3 and Figure 4.9). From this assumption, we can deduce that when the electrode was treated with a positive current, the amount of unpaired electrons on the surface is larger than that on the reduced BDDs.

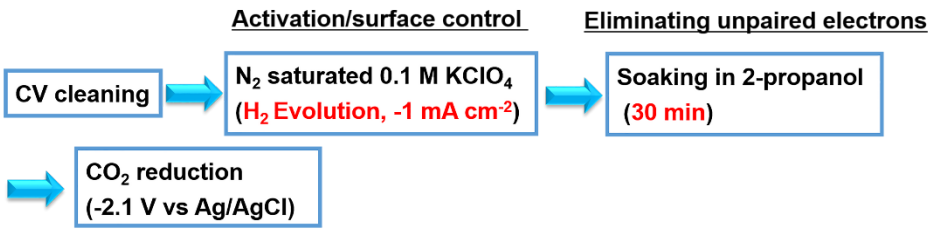

Figure 4.12 Flow diagram showing the experimental procedures for the introduction of 2-propanol before CO_2 reduction.

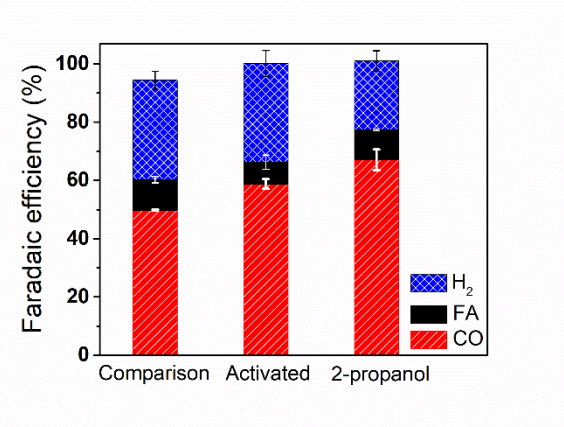

Figure 4.13 Compared Faradaic efficiencies of CO, H_2 and formic acid in the CO_2 reductions by various BDD electrodes including the comparison BDD, reduction-activated BDD and the BDD treated by 2-propanol.

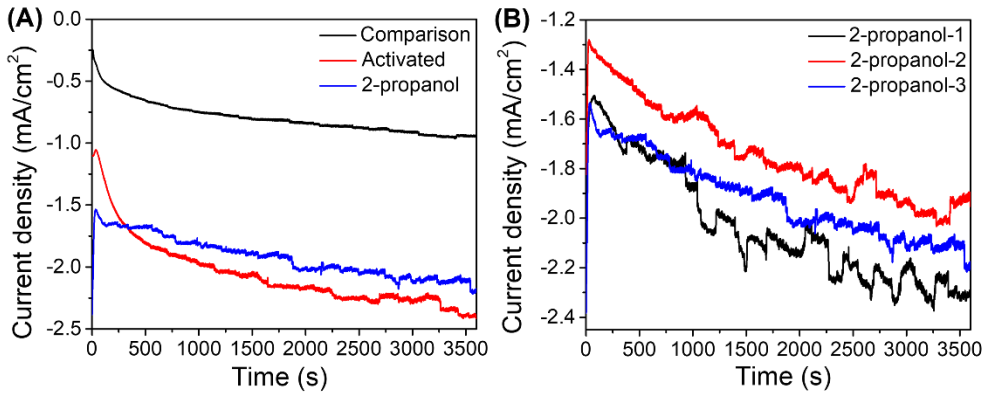

Figure 4.14 (A) The comparison of the current densities during 1 h CO_2 reduction on the comparison BDD, the reduction-activated BDD and the BDD treated by 2-propanol. (B) Current densities of three times CO_2 reduction on the BDD treated by 2-propanol. The CO_2 reductions were performed at -2.1 V vs Ag/AgCl.

Table 4.6 Faradaic efficiencies for all products and production rate of CO in electrochemical CO_2 reduction at -2.1 V by 1% BDD electrodes including the comparison BDD, the reduction-activated BDD and the BDD treated by 2-propanol. Potentials are referred to Ag/AgCl (KCl sat).

Condition	H_2 (%)	CO (%)	Formic acid (%)	Production rate (μmol cm^{-2} h^{-1})
Comparison	34.07±3.11	49.77±0.25	10.55±1.1	7.45±0.8
Activated	33.83±4.51	58.8±1.71	7.51±2.45	23.45±1.37
2-propanol	23.77±3.5	67.03±3.59	10.26±0.27	23.76±2.82

In order to verify the function of the unpaired electrons in eCO_2RR on BDD electrodes, 2-propanol was introduced as a scavenging agent. 2-propanol has been demonstrated to be a favorable coreactant which can form strong interaction with free radicals.[37,38] This property makes it possible to eliminate the catalytic activity of unpaired electrons on the electrode surface. As shown in Figure 4.12, before the formal eCO_2RR, the cathodic-activated BDD electrode was immersed in 2-propanol solution to suppress the influence of unpaired electrons on the eCO_2RR. We found that compared with the cathodic-activated only, the BDD electrode after soaking in 2-propanol showed a production rate of CO at the same level, but the Faradaic efficiency for CO production increased from 58.8% to 67.03% (Figure 4.13, Figure 4.14 and Table 4.6).

The improved Faradaic efficiency is mainly due to the reduced activity for the

hydrogen evolution reaction as the Faradaic efficiency was decreased from 33.83% to 23.77%. These results indicate that the unpaired electrons generated from the excessive hydrogen evolution on BDD electrodes facilitates the hydrogen evolution, but cannot be the catalytic sites for eCO_2RR.

Therefore, we can conclude that excessive oxidation or reduction is detrimental for CO production on BDD. Only when the surface of the BDD electrode is in a lower reduced state, the amount of unpaired electrons on the surface is the minimum, therefore state and stability of the BDD surface lead to the optimal condition for CO production. It can be seen that in the eCO_2RR on BDD for CO production, both the undercoordinated site dominated by unpaired electrons and the oxidized surface cannot be catalytic sites which is a circumstance different from the eCO_2RR on other metal or carbon-based electrodes.[39,40]

Combining the investigation concerning the surface terminations on BDD in Chapter 3 and Chapter 4, we can conclude that in the process of eCO_2RR on BDD, the -OH termination is beneficial to the production of formic acid, and the unpaired electrons on the electrode surface are more likely to promote the hydrogen evolution, while it seems that the hydrogen termination will facilitate the CO production.

4.4 Conclusion

Here, by pretreating the surface of BDD electrodes with different current densities, we evaluated the performance of the surface in various redox states to electrochemically reduce CO_2 to CO. As the result, the reduced BDDs showed improved Faradaic efficiency and production rate of CO. Especially, when current densities for the pretreatment were set at -0.1 mA cm^{-2} and -1 mA cm^{-2}, the production rate of CO exceeded 23 μmol cm^{-2} h^{-1}, which was more than three times that of the comparison electrode. The improvement of the production rate means that the amount of catalytic sites involved in the CO_2 reduction reaction were increased. Combined with the measurement results of the open circuit potential, we suggested that the stable reduced surface state provides the most catalytic site for the CO production on BDD.

This work demonstrates that the relatively stable reduced electrode surface also has the potential to efficiently reduce CO_2 to CO, and provides a new perspective for the CO production on BDD electrodes.

4.5 References

(1) Aresta, M.; Dibenedetto, A.; Angelini, A. Catalysis for the Valorization of Exhaust Carbon: From CO_2 to Chemicals, Materials, and Fuels. Technological Use of CO_2. *Chem. Rev.* **2014**, *114* (3), 1709–1742.

(2) Bushuyev, O. S.; De Luna, P.; Dinh, C. T.; Tao, L.; Saur, G.; van de Lagemaat, J.; Kelley, S. O.; Sargent, E. H. What Should We Make with CO_2 and How Can We Make It? *Joule* **2018**, *2* (5), 825–832.

(3) White, J. L.; Baruch, M. F.; Pander, J. E.; Hu, Y.; Fortmeyer, I. C.; Park, J. E.; Zhang, T.; Liao, K.; Gu, J.; Yan, Y.; Shaw, T. W.; Abelev, E.; Bocarsly, A. B. Light-Driven Heterogeneous Reduction of Carbon Dioxide: Photocatalysts and Photoelectrodes. *Chem. Rev.* **2015**, *115* (23), 12888–12935.

(4) Nielsen, D. U.; Hu, X. M.; Daasbjerg, K.; Skrydstrup, T. Chemically and Electrochemically Catalysed Conversion of CO_2 to CO with Follow-up Utilization to Value-Added Chemicals. *Nat. Catal.* **2018**, *1* (4), 244–254.

(5) Whipple, D. T.; Kenis, P. J. A. Prospects of CO_2 Utilization via Direct Heterogeneous Electrochemical Reduction. *J. Phys. Chem. Lett.* **2010**, *1* (24), 3451–3458.

(6) Kondratenko, E. V.; Mul, G.; Baltrusaitis, J.; Larraz ábal, G. O.; P érez-Ram írez, J. Status and Perspectives of CO_2 Conversion into Fuels and Chemicals by Catalytic, Photocatalytic and Electrocatalytic Processes. *Energy Environ. Sci.* **2013**, *6* (11), 3112–3135.

(7) Daiyan, R.; Lu, X.; Ng, Y. H.; Amal, R. Liquid Hydrocarbon Production from CO_2 : Recent Development in Metal-Based Electrocatalysis. *ChemSusChem* **2017**, *10* (22), 4342–4358.

(8) Dry, M. E. The Fischer-Tropsch Process: 1950-2000. *Catal. Today* **2002**, *71* (3–4), 227–241.

(9) Maitlis, P. M.; Haynes, A.; Sunley, G. J.; Howard, M. J. Methanol Carbonylation Revisited: Thirty Years On. *J. Chem. Soc. - Dalt. Trans.* **1996**, 11, 2187–2196.

(10) Mariano, R. G.; Kang, M.; Wahab, O. J.; McPherson, I. J.; Rabinowitz, J. A.; Unwin, P. R.; Kanan, M. W. Microstructural Origin of Locally Enhanced CO_2 Electroreduction Activity on Gold. *Nat. Mater.* **2021**, *20* (7), 1000–1006.

(11) Mezzavilla, S.; Horch, S.; Stephens, I. E. L.; Seger, B.; Chorkendorff, I. Structure Sensitivity in the Electrocatalytic Reduction of CO_2 with Gold Catalysts. *Angew. Chemie - Int. Ed.* **2019**, *58* (12), 3774–3778.

(12) Wu, J.; Ma, S.; Sun, J.; Gold, J. I.; Tiwary, C.; Kim, B.; Zhu, L.; Chopra, N.; Odeh, I. N.; Vajtai, R.; Yu, A. Z.; Luo, R.; Lou, J.; Ding, G.; Kenis, P. J. A.; Ajayan, P. M. A Metal-Free Electrocatalyst for Carbon Dioxide Reduction to Multi-Carbon Hydrocarbons and Oxygenates. *Nat. Commun.* **2016**, *7*, 13869.

(13) Zhang, L.; Ng, M. L.; Vojvodic, A. Role of Undercoordinated Sites for the Catalysis in Confined Spaces Formed by Two-Dimensional Material Overlayers. *J. Phys. Chem. Lett.* **2020**, 9400–9407.

(14) Wang, W.; Shang, L.; Chang, G.; Yan, C.; Shi, R.; Zhao, Y.; Waterhouse, G. I. N.; Yang, D.; Zhang, T. Intrinsic Carbon-Defect-Driven Electrocatalytic Reduction of Carbon Dioxide. *Adv. Mater.* **2019**, *31*, 1808276.

(15) Kang, X.; Li, L.; Sheveleva, A.; Han, X.; Li, J.; Liu, L.; Tuna, F.; McInnes, E. J. L.; Han, B.; Yang, S.; Schröder, M. Electro-Reduction of Carbon Dioxide at Low over-Potential at a Metal–Organic Framework Decorated Cathode. *Nat. Commun.* **2020**, *11*, 5464.

(16) Gong, Q.; Ding, P.; Xu, M.; Zhu, X.; Wang, M.; Deng, J.; Ma, Q.; Han, N.; Zhu, Y.; Lu, J.; Feng, Z.; Li, Y.; Zhou, W.; Li, Y. Structural Defects on Converted Bismuth Oxide Nanotubes Enable Highly Active Electrocatalysis of Carbon Dioxide Reduction. *Nat. Commun.* **2019**, *10*, 2807.

(17) Chen, Y.; Li, C. W.; Kanan, M. W. Aqueous CO_2 Reduction at Very Low Overpotential on Oxide-Derived Au Nanoparticles. *J. Am. Chem. Soc.* **2012**, *134* (49), 19969–19972.

(18) Chen, Y.; Kanan, M. W. Tin Oxide Dependence of the CO_2 Reduction Efficiency on Tin Electrodes and Enhanced Activity for Tin/Tin Oxide Thin-Film Catalysts. *J. Am. Chem. Soc.* **2012**, *134* (4), 1986–1989.

(19) Li, C. W.; Kanan, M. W. CO_2 Reduction at Low Overpotential on Cu Electrodes Resulting from the Reduction of Thick Cu_2O Films. *J. Am. Chem. Soc.* **2012**, *134* (17), 7231–7234.

(20) Yuan, X.; Chen, S.; Cheng, D.; Li, L.; Zhu, W.; Zhong, D.; Zhao, Z. J.; Li, J.; Wang, T.; Gong, J. Controllable Cu^0-Cu^+ Sites for Electrocatalytic Reduction of Carbon Dioxide. *Angew. Chemie - Int. Ed.* **2021**, *60* (28), 15344–15347.

(21) Du, J.; Fiorani, A.; Inagaki, T.; Otake, A.; Murata, M.; Hatanaka, M.; Einaga, Y. A New Pathway for CO_2 Reduction Relying on the Self-Activation Mechanism of Boron-Doped Diamond Cathode . *JACS Au* **2022**, *2*, 1375-1382.

(22) Wu, J.; Risalvato, F. G.; Ma, S.; Zhou, X. D. Electrochemical Reduction of Carbon Dioxide III. the Role of Oxide Layer Thickness on the Performance of

Sn Electrode in a Full Electrochemical Cell. *J. Mater. Chem. A* **2014**, *2* (6), 1647–1651.

(23) Ikemiya, N.; Natsui, K.; Nakata, K.; Einaga, Y. Long-Term Continuous Conversion of CO_2 to Formic Acid Using Boron-Doped Diamond Electrodes. *ACS Sustain. Chem. Eng.* **2018**, *6* (7), 8108–8112.

(24) Kashiwada, T.; Watanabe, T.; Ootani, Y.; Tateyama, Y.; Einaga, Y. A Study on Electrolytic Corrosion of Boron-Doped Diamond Electrodes When Decomposing Organic Compounds. *ACS Appl. Mater. Interfaces* **2016**, *8*, 28299–28305.

(25) Hori, Y. Electrochemical CO_2 Reduction on Metal Electrodes; Springer: New York, 2008; pp 89−189.

(26) Verma, S.; Kim, B.; Jhong, H. R. M.; Ma, S.; Kenis, P. J. A. A Gross-Margin Model for Defining Technoeconomic Benchmarks in the Electroreduction of CO_2. *ChemSusChem* **2016**, *9* (15), 1972–1979.

(27) Du, J.; Fiorani, A.; Einaga, Y. An Efficient, Formic Acid Selective CO_2 electrolyzer with a Boron-Doped Diamond Cathode. *Sustain. Energy Fuels* **2021**, *5* (10), 2590–2594.

(28) Natsui, K.; Iwakawa, H.; Ikemiya, N.; Nakata, K.; Einaga, Y. Stable and Highly Efficient Electrochemical Production of Formic Acid from Carbon Dioxide Using Diamond Electrodes. *Angew. Chemie - Int. Ed.* **2018**, *57* (10), 2639–2643.

(29) Xu, J.; Natsui, K.; Naoi, S.; Nakata, K.; Einaga, Y. Effect of Doping Level on the Electrochemical Reduction of CO_2 on Boron-Doped Diamond Electrodes. *Diam. Relat. Mater.* **2018**, *86* (March), 167–172.

(30) Xu, J.; Einaga, Y. Effect of Sp^2 Species in a Boron-Doped Diamond Electrode on the Electrochemical Reduction of CO_2. *Electrochem. commun.* **2020**, *115* (April), 106731.

(31) Tomisaki, M.; Kasahara, S.; Natsui, K.; Ikemiya, N.; Einaga, Y. Switchable Product Selectivity in the Electrochemical Reduction of Carbon Dioxide Using Boron-Doped Diamond Electrodes. *J. Am. Chem. Soc.* **2019**, *141* (18), 7414–7420.

(32) Kasahara, S.; Natsui, K.; Watanabe, T.; Yokota, Y.; Kim, Y.; Iizuka, S.; Tateyama, Y.; Einaga, Y. Surface Hydrogenation of Boron-Doped Diamond Electrodes by Cathodic Reduction. *Anal. Chem.* **2017**, *89* (21), 11341–11347.

(33) Kasahara, S.; Ogose, T.; Ikemiya, N.; Yamamoto, T.; Natsui, K.; Yokota, Y.; Wong, R. A.; Iizuka, S.; Hoshi, N.; Tateyama, Y.; Kim, Y.; Nakamura, M.;

Einaga, Y. In Situ Spectroscopic Study on the Surface Hydroxylation of Diamond Electrodes. *Anal. Chem.* **2019**, *91* (8), 4980–4986.

(34) Song, Q.; Li, J.; Zhang, B.; Li, H.; Liu, X. Controlling the D-Band for Improved Oxygen Evolution Performance in Ni Modulated Ultrafine Co Nanoparticles Embedded in Nitrogen-Doped Carbon Microspheres. *J. Colloid Interface Sci.* **2022**, *623*, 44–53.

(35) Tan, H.; Tang, B.; Lu, Y.; Ji, Q.; Lv, L.; Duan, H.; Li, N.; Wang, Y.; Feng, S.; Li, Z.; Wang, C.; Hu, F.; Sun, Z.; Yan, W. Engineering a Local Acid-like Environment in Alkaline Medium for Efficient Hydrogen Evolution Reaction. *Nat. Commun.* **2022**, *13*, 2024.

(36) Yang, Q.; Le, C.; Li, G.; Heine, T.; Felser, C.; Sun, Y. Enhancement of Basal Plane Electrocatalytic Hydrogen Evolution Activity via Joint Utilization of Trivial and Non-Trivial Surface States. *Appl. Mater. Today* **2021**, *22*, 100921.

(37) Honda, K.; Yamaguchi, Y.; Yamanaka, Y.; Yoshimatsu, M.; Fukuda, Y.; Fujishima, A. Hydroxyl Radical-Related Electrogenerated Chemiluminescence Reaction for a Ruthenium Tris(2,2′)Bipyridyl/Co-Reactants System at Boron-Doped Diamond Electrodes. *Electrochim. Acta* **2005**, *51* (4), 588–597.

(38) Wu, H.; Mu, Y.; Zhang, X.; Jiang, G. Relative Rate Constants for the Reactions of Hydroxyl Radicals and Chlorine Atoms with a Series of Aliphatic Alcohols. *Int. J. Chem. Kinet.* **2003**, *35* (2), 81–87.

(39) Duan, X.; Xu, J.; Wei, Z.; Ma, J.; Guo, S.; Wang, S.; Liu, H.; Dou, S. Metal-Free Carbon Materials for CO_2 Electrochemical Reduction. *Adv. Mater.* **2017**, *29*, 1701784.

(40) Zhu, D. D.; Liu, J. L.; Qiao, S. Z. Recent Advances in Inorganic Heterogeneous Electrocatalysts for Reduction of Carbon Dioxide. *Adv. Mater.* **2016**, *28* (18), 3423–3452.

Chapter 5

Summary and Future Perspective

5.1 Summary

In this thesis we first evaluated the electrical-to-chemical energy (ECE) conversion efficiency and the energy distribution in the CO_2 electrolyzer based on boron doped diamond (BDD) electrodes. Then the reaction pathway for formic acid production and possible catalytic site for CO production in the electrochemical CO_2 reduction reaction (eCO_2RR) on BDD were further investigated. The specific summary of each chapter is as follows.

In Chapter 2, we proposed an efficient and high product-selectivity CO_2 electrolyzer based on BDD cathode. As a stable non-toxic inert electrode, BDD is able to effectively convert CO_2 into formic acid. The Faradaic efficiency of as high as 96% for the production of formic acid can be obtained at the applied voltage of 3.5 V. The ECE conversion efficiency for formic acid reached 43% at 3 V, which was very close to the predicted maximum value at 3 V. Besides, the total ECE conversion efficiency attained the value of up to 45%, if the secondary products including CO and H_2 were taken into account. Concerning the energy distribution in this BDD-based CO_2 electrolyzer, except the energy for the electrical-to-chemical conversion, the energy consumption for the overpotential is the most, which reached around 50.64%. And the energy loss from the resistance is increased from 3% to 14% along with the increasing reaction current. Therefore, reducing the energy consumption for overpotential and resistance is efficient strategy toward the improvement of the ECE conversion efficiency.

In Chapter 3, we found the self-activation effect of BDD electrodes in eCO_2RR, which means that the electrochemical performance (current and Faradaic efficiency) can be gradually improved during eCO_2RR on BDD. XPS, ATR-IR and Fc-NH_2 tracer experiments indicate that unidentate carbonate and carboxylic intermediates were generated on the surface of BDD and would keep increasing during eCO_2RR. Based on the presence of these intermediates, a new pathway for electrochemical CO_2 reduction was proposed, which was independent of the generation of $CO_2^{\bullet-}$. This reaction pathway is the reason of the self-activation effect. Theoretical calculation was further performed to verify the rationality. Benefiting from the self-activation effect of BDD, in long-term two-electrode electrolysis a dramatic energy conversion efficiency of 50.2% was attained for the single product of formic acid.

In Chapter 4, at the first part, we found that the optimized potential range on BDD electrods for CO_2 reduction to CO is from -1.9 V to -2.1 V (vs Ag/AgCl). Then, the BDD surface was pretreated by various current densities in inert supporting electrolyte in order to evaluate the performance of eCO_2RR with different redox states. The CO production-rate of the reduced BDD electrode was significantly improved, especially when the pretreatment current densities were -0.1 mA cm^{-2} and -1 mA cm^{-2}, the production rate of CO exceeded 23 μmol cm^{-2} h^{-1}, which was more than three times that of the comparison sample. The improvement of the production rate means that the amount of catalytic site involved in the CO_2 reduction reaction was increased. Combined with the measurement results of the XPS, open circuit potential and the comparison experiments with 2-propanol, we believe that the stable reduced surface state is the optimal condition for the CO production on BDD.

5.2 Future Perspective

As a working electrode for eCO_2RR, BDD possesses the superiorities in terms of product selectivity, cost of raw material, long-term stability and resistance to corrosion. Benefiting from the wide potential window and the low background current, BDD also provides favorable electrochemical environment for mechanistic investigations. On the basis of the investigations in this thesis, the directions for the future investigations can be predicted in the following three aspects.

1. Although high Faradaic efficiency and over 50% energy conversion efficiency were achieved by the BDD-based two-electrode system in the second and third chapters. Compared to some metal-based electrodes such as Au, Ag and Cu, the current density and production rate are still too low to match the industrial requirements. Recently, by creating enhanced adsorption between CO_2 and working electrodes, the electrolysis system based on gas diffusion electrode exhibited outstanding improvements in reaction current. Thus the preparation of BDD as a gas diffusion electrode is expected to be a promising approach to increase reaction current and production rate.

2. BDD shows remarkable product selectivity for the products of CO and formic acid. Referring to the Sabatier principle, we can infer that the adsorption strength between CO_2 and BDD surface is still at a relatively low level. Hence, improving the adsorption capacity of BDD for reactants will be crucial for the further enhancement of the catalytic activity and even for the generation of multi-carbon products.

3. In the electrolysis system for CO production, we have demonstrated the functions of some surface groups including the reduced surface (-H termination), -OH terminations and the unpaired electrons. However, the surface control involving C=O bonds is hard to be achieved by electrochemical routes. Therefore, revealing the role of the native C=O bonds on BDD in eCO_2RR will be the next topic of mechanistic investigation.

Appendix

The computational methods and calculation details for Chapter 3

We first constructed a surface model based on the bulk diamond structure with a lattice constant of 3.56 Å obtained in preliminary calculations. This lattice parameter is in agreement with the experimental value (3.57 Å).[1] The corresponding C-C bond length was 1.54 Å. We used the stable (111) surface rather than the (100) surface according to the previous study.[2] The surface area in the x-y plane was set to 8.713 × 10.061 Å^2 and eight bilayers were placed in the z direction. The supercell size along the z direction was about 50 Å, which included a free space for a vacuum region of ~34 Å. The resultant diamond slab contained 256 carbon atoms. A surface of interest was terminated by hydrogen (H) except the reaction site with a hydroxyl group (OH) although Futera and coworkers reported that the fully OH terminated (111) surface is more stable than the H terminated one.[2] This is because we found an unreasonable short-distance O-O pair (2.48 Å) in the fully OH terminated surface. Also, the experimental X-ray photoelectron spectrometer measurement (Figure 3.6) indicates that C-H bonds remain at the surface even after the activation. The other surface was terminated fully by hydrogen atoms. The boron doping was carried out by substituting two carbon atoms under the surface bilayer. The doping ratio in this case was ~0.8%, which is a little bit higher than that in the experiment (0.1%). The reason why two carbon atoms were selected for the substitution rather than one is to avoid demanding spin-polarized calculations as with the previous study.[2] The two boron atoms were located separately in the second and fourth bilayers as an example. Note that the boron's position has been shown to have less impact on the electronic structure of the H terminated surface.[3] The slab structure thus constructed is displayed in Figure A1.

To estimate the thermodynamic stability of each surface state of interest, we calculated grand potential using a combined method[4] of the effective screening medium (ESM)[5] and reference interaction site model (RISM)[6] methods under the experimental electrode potential condition (~ -2.0 V vs Ag/AgCl). The grand potential in this study was defined as

$$\Phi = E_{\mathrm{DFT}} + \Delta\mu - \mu_e \Delta N_e, \qquad (1)$$

where the respective terms in order from the left in the right-hand side represent electronic energy of the slab, solvation free energy, and energy for introducing electrons into the calculation system. The third term consists of the chemical potential of electrons μ_e and the difference in the number of electrons relative to the charge neutral

system ΔN_e. The electronic energy and solvation free energy were calculated by the density functional theory (DFT) and the Laue-represented RISM method,[6] respectively. To perform the calculations, the open boundary condition was employed in the normal direction to the surface by setting the vaccum-slab-vaccum configuration in the ESM method. The vacuum regions were filled by 0.5 M KCl aqueous solution at 300 K, which was represented by the RISM. The parameters employed in the RISM calculation are summarized in Table A1, which are based on the OPLS-AA force field and SPC water models. The Kovalenko-Hirata closure[7] was used to solve the RISM integral equation.

The first-principles DFT calculations to evaluate the electronic energy were performed using the Becke-Lee-Yang-Parr exchange-correlation functional[8,9] based on the generalized gradient approximation. The functional has also been employed in a previous study by Futera and coworkers on boron-doped diamond surfaces.[2] The Grimme's empirical dispersion correction method was used to treat the dispersion interaction for organic molecules.[10] The core–valence interaction was taken into account by the norm-conserving Goedecker–Hartwigsen–Hutter–Teter's pseudopotentials,[11,12] and the plane-wave basis set with a cutoff energy of 80 Ry was used for describing the electronic structure. Brillouin zone integration was performed on the Γ point only due to the slab supercell geometry. All the calculations were performed using the Quantum Espresso program package[13] in which the ESM-RISM method has been implemented.[6]

According to the paper by Haruyama and coworkers,[4] we estimated the standard hydrogen electrode (SHE) potential to be 5.97 V versus inner potential at the bulk KCl aqueous solution region. Based on the present experiments performed around at -2 V vs Ag/AgCl corresponding to about -1.8 V vs SHE, we considered charged systems which give the chemical potential μ_e of about -4.2 eV. In addition, to estimate the grand potential difference between surface states, we considered the following stoichiometric chemical equations:

$$[\text{unidentate carbonate state}] + H_3O^+ + e^- \rightarrow [\text{carboxylic state}] + H_2O$$

for between unidentate carbonate and carboxylic surface state, and

$$[\text{carboxylic state}] + 2H_3O^+ + e^- \rightarrow [\text{hydroxyl state}] + HCOOH + 2H_2O$$

for between carboxylic and hydroxyl surface states. Note that grand potential of molecules in solution was also calculated in the same manner as the surface states.

Based on the computational method described above, we performed geometry optimization calculations of three individual surface states with unidentate carbonate, carboxylic, and OH groups. The resultant surface structures are shown in Figure 3.16. The charges introduced to keep the electrode potential were also listed in this figure. While the unidentate carbonate surface state was negatively charged, the others were almost electrically neutral. This negatively charged unidentate carbonate state is expected to reflect a stable carbonate anion. As described in the main text, we found that the reaction proceeds exothermically. Although the present calculations considered no vibrational entropic effects and zero-point energies, the qualitative trend would be independent of the effects because of the large difference in grand potential. In addition to the intermediates suggested in the experiment, we found that a surface state with a lactone form is also a stationary point along the reaction process. The corresponding stoichiometric chemical equation is expressed as

$$[\text{unidentate carbonate state}] + H_3O^+ + e^- \rightarrow [\text{lactone state}] + 2H_2O.$$

Its grand potential was more stable by 16 kcal/mol than that of the unidentate carbonate state, but the state was not stable as much as the carboxylic state. However, the lactone was formed with the release of a water molecule from the unidentate carbonate state according to the above stoichiometric chemical equation. This implies that the lactone state was free-energetically stabilized by translational and rotational entropy effects of the water molecule. Taking into account the effects, we found that the lactone state was comparable in free energy to the carboxylic state (see blue-colored values in Figure 3.16). Nevertheless, it should be emphasized that the priority of the carboxylic state was unchanged. Further analyses on the detailed electrochemical catalytic cycle will be reported in a future paper.

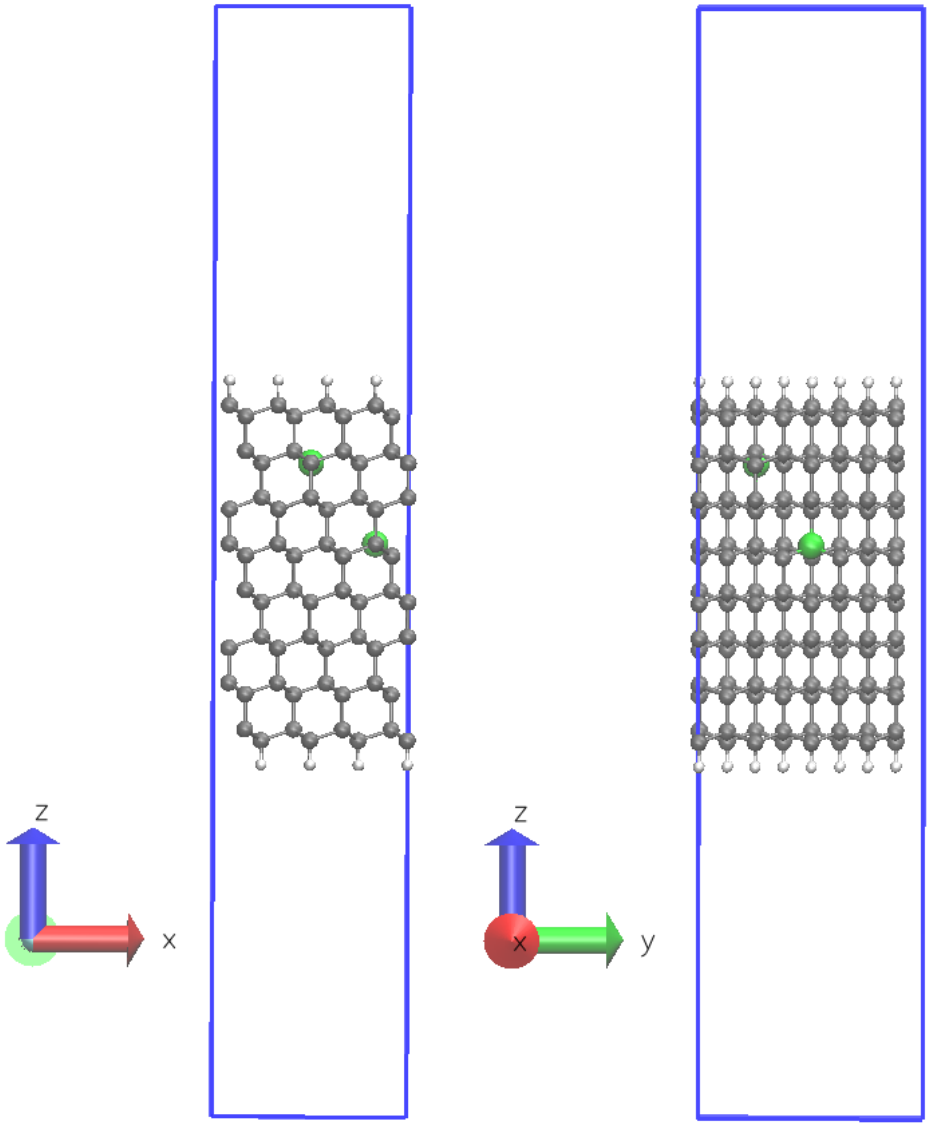

Figure A1. Calculation supercell containing an H-terminated diamond slab. Gray, white, and green spheres represent carbon, hydrogen, and boron atoms, respectively. The carbon dioxide reduction reaction occurs on the upper surface. Reproduced with permission from Du, J.; Fiorani, A.; Inagaki, T.; Otake, A.; Murata, M.; Hatanaka, M.; Einaga, Y. A New Pathway for CO_2 Reduction Relying on the Self-Activation Mechanism of Boron-Doped Diamond Cathode. *JACS Au* **2022**, *2*, 1375-1382. Copyright 2022, American Chemical Society.

Table A1. Point charge and Lennard-Jones parameters used in the RISM calculations

atom type	q (e)	ε (kcal/mol)	σ (Å)
Boron-doped diamond surface			
C(-C)	-	0.055	3.370
C(-O)	-	0.105	3.750
O(-H)	-	0.210	3.066
O(-C)	-	0.210	2.960
H(-O)	-	0.055	1.000
H(-C)	-	0.016	2.471
B	-	0.095	3.581
KCl aqueous Solution			
O(-H)	− 0.82	0.155	3.166
H(-O)	0.41	0.046	1.000
K^+	1.00	0.0005	5.170
Cl^-	− 1.00	0.710	4.020

References

(1) Holloway, H., Hass, K. C., Tamor, M. A., Anthony, T. R., and Banholzer, W. F. Isotopic dependence of the lattice constant of diamond. *Phys. Rev. B* **1991**, *44*, 7123.

(2) Futera, Z., Watanabe, T., Einaga, Y., and Tateyama, Y. First Principles Calculation Study on Surfaces and Water Interfaces of Boron-Doped Diamond. *J. Phys. Chem. C* **2014**, *118*, 22040.

(3) Anh, L. T., Catalan, F. C. I., Kim, Y., Einaga, Y., Tateyama, Y. Boron position-dependent surface reconstruction and electronic states of a boron-doped diamond (111) surfaces: an *ab initio* study. *Phys. Chem. Chem. Phys.* **2021**, *23*, 15628-15634.

(4) Haruyama, J., Ikeshoji, T., and Otani, M. Electrode potential from density functional theory calculations combined with implicit solvation theory. *Phys. Rev. Mater.* **2018**, *2*, 095801.

(5) Otani, M. and Sugino, O. First-principles calculations of charged surfaces and interfaces: A plane-wave nonrepeated slab approach. *Phys. Rev. B* **2006**, *73*, 115407.

(6) Nishihara, S. and Otani, M. Hybrid solvation models for bulk, interface, and membrane: Reference interaction site methods coupled with density functional theory. *Phys. Rev. B* **2017**, *96* 115429.

(7) Kovalenko, A., and Hirata, F. Self-consistent description of a metal–water interface by the Kohn–Sham density functional theory and the three-dimensional reference interaction site model. *J. Chem. Phys.* **1999**, *110*, 10095.

(8) Becke, A. D. Density-Functional Exchange-Energy Approximation With Correct Assymptonic Behaviour. *Phys. Rev. A* **1988**, *38*, 3098-3100.

(9) Lee, C., Yang, W., Parr, R. G. Development of the Colle-Salvetti Correlation-Energy Formula into a Functional of the Electron Density. *Phys. Rev. B* **1988**, *37*, 785-789.

(10) Grimme, S., Antony, J., Ehrlich, S., and Krieg, H. A consistent and accurate *ab initio* parameterization of density functional dispersion correction (DFT-D) for the 94 elements H-Pu. *J. Chem. Phys.* **2010**, *132*, 154104.

(11) Goedecker, S., Teler, M., and Hutter, J. Separable dual-space Gaussian pseudopotentials. *Phys. Rev. B* **1996**, *54* 1703.

(12) Hartwigsen, C., Goedecker, S., and Hutter, J. Relativistic separable dual-space Gaussian pseudopotentials from H to Rn. *Phys. Rev. B* **1998**, *58*, 3641.

(13) Giannozzi, P. et al, J. Phys.: *Condens. Matter* **2009**, *21*, 395502; **2017**, *29*, 465901; *J. Phys. Chem.* **2020**, *152*, 154105.

List of Publications and Conferences

Published papers presented in this thesis

(1) Du, J.; Fiorani, A.; Inagaki, T.; Otake, A.; Murata, M.; Hatanaka, M.; Einaga, Y.
"A New Pathway for CO_2 Reduction Relying on the Self-Activation Mechanism of Boron-Doped Diamond Cathode."
JACS Au **2022**, *2*, 1375-1382.

(2) Du, J.; Fiorani, A.; Einaga, Y.
"An Efficient, Formic Acid Selective CO_2 electrolyzer with a Boron-Doped Diamond Cathode."
Sustain. Energy Fuels **2021**, *5* (10), 2590–2594.

Other publications

(1) Nihongi, S.; Otake, A.; Du, J.; Einaga, Y.
"Convection Control in a Flow Cell on Electrochemical CO_2 Reduction Using a Boron-Doped Diamond Electrode."
Carbon **2022**, *200*, 456–461.

(2) Otake, A.; Du, J.; Einaga, Y.
"Activation of Boron-Doped Diamond Electrodes for Electrochemical CO_2 Reduction in a Halogen-Free Electrolyte."
ACS Sustain. Chem. Eng. **2022**, *10* (44), 14445–14450.

International conference

(1) Du, J.; Fiorani, A.; Einaga, Y.
"Active oxygen-evolution anode assisted improvements in the CO_2 reduction of boron-doped diamond based electrolyzer."
Pacifichem 2021, Online, December 19th (2021).

Domestic conference

(1) Du, J.; Fiorani, A.; Inagaki, T.; Otake, A.; Murata, M.; Hatanaka, M.; Einaga, Y.
"A New Pathway for CO_2 Reduction Relying on the Self-Activation Mechanism of Boron-Doped Diamond Cathode."
36th Diamond Symposium, Yokohama, Japan, November 16th (2022).

(2) Du, J.; Fiorani, A.; Einaga, Y.
"An Efficient, Formic Acid Selective CO_2 electrolyzer with a Boron-Doped Diamond Cathode."
The 88th ECSJ Spring Meeting, Online, March 24th (2021).

Acknowledgment

I recall that when I first arrived in Japan, whenever someone asked me why I chose here to complete the Ph. D. program, the answer I gave at that time was that I wanted to do high-quality researches. And when I ask the same question to myself today, I agree with what my Japanese teacher said in the preparatory school for Chinese students to Japan, that is, "Studying abroad is to experience a different culture."

The three years of my Ph. D. program coincided with the global pandemic of COVID-19. On the one hand, the travel restrictions imposed to prevent infection makes me focus more on researches, and on the other hand, I was also forced to reduce contact with the outside world, and lost a lot of interesting experience in my daily life. During the period of my Ph. D. program, I experienced a different research atmosphere from my master period, and fortunately I quickly integrated into this atmosphere and enjoyed it. Although I didn't have too much contact with the Japanese daily life, I still partially experienced the local life and culture in Japan and met various researchers from all over the world. All this made me feel the vastness and colorfulness of the world.

At the end of my Ph.D. program, I would first like to thank my supervisor, Prof. Yasuaki Einaga who provided me with the opportunity to complete my Ph.D. at Keio University. After that, I want to thank Prof. Einaga and Dr. Andrea Fiorani (Ando San) for their help and guidance in my daily research. My major in the master period was condensed matter physics, and my Ph.D. program was focusing on the electrochemical CO_2 reduction. At the beginning of my research, I knew nothing about electrochemistry. Benefiting from their patient guidance, I was able to understand the electrochemical reaction process in stepwise and apply the knowledge I learned into practical research.

I sincerely thank all of the members in Einaga lab for their help and companionship. Tomisaki san and Xu san taught me how to use the instruments in our lab and analysis center. Thank Yamamoto san, Otake san and Murata san for their support and suggestions. I feel very grateful to my cooperators in the 3rd chapter, Inagaki sensei and Hatanaka sensei. They verified the rationality of the proposed mechanism for electrochemical CO_2 reduction from the perspective of theoretical calculations. At the same time, I also learned a lot from this cooperative research.

In addition, I would like to appreciate all the reviewers of my Ph.D. defense, Prof. Taku Hasobe, Prof. Miho Hatanaka, and Prof. Hiroaki Imai for all the kind suggestions and comments for my work. I am also grateful for the revision of this graduation thesis, which makes it better than before.

Besides, I also want to thank my family and my girlfriend for their understanding and support during my studying abroad.

Finally, I would like to thank the Japanese government scholarship (MEXT) and the China Scholarship Council for their financial support.

Japan, February 2023

Jinglun Du